PULSE SHAPE STUDIES OF COSMIC RAY COMPOSITION

A thesis submitted to the
Department of Physics
and
Mathematical Physics
University of Adelaide

for the degree of Doctor of Philosophy

by

Matthew Downie Sinnott B.Sc (Hons.)

January 2002

TABLE OF CONTENTS

SUMMARY

The thesis contains a study of the pulse shape of atmospheric Čerenkov signals emanating from cosmic ray showers. This technique has been examined in light of its ability to the discriminate between different mass cosmic ray primaries.

Chapter 1 begins with an overview of the field of cosmic ray research. A brief history is discussed and we introduce the competing models for origin, acceleration and propagation of these cosmic rays. Direct and indirect measurements are discussed in light of the constraints these results place on the models at energies above 1 TeV.

In chapter 2, we discuss the dynamics of shower development. The components of the shower are presented, with much attention given to the muon and electromagnetic components in defining bulk shower features, and mass discrimination ability. Differences between showers generated by light and heavy primaries are discussed and the effect of the geomagnetic field is briefly examined in the context of timing analysis.

Chapter 3 introduces the atmospheric Čerenkov technique, discusses the lateral and angular distributions of the light pool, and examines the operation of the most simple atmospheric Čerenkov detector possible. Working definitions of energy threshold and collecting area are introduced here.

The pulse shape system used in this work is discussed next in chapter 4, with particular focus on the sensitivity of the detector and sources of error. The detector is then calibrated by a number of methods.

Much of the work done in this thesis appears in chapter 5. The modelling of the telescope's response is discussed leading to optimal parameters for discriminating between light and heavy cosmic ray events. This has been examined across a variety of zenith angles in order to probe a range of energy by utilising the increased energy threshold of the detector at low elevations. Sensitivity of the technique to atmospherics has also been discussed.

Chapter 6 then looks at a goodness of fit analysis using the optimal parameters chosen in chapter 5. A two-component Monte Carlo model is generated from CORSIKA protons and iron nuclei and matched with real measurements taken by the author.

Chapter 7 finishes with comments on these results and the limitations of the technique. Suggestions for further work have also been included.

STATEMENT OF ORIGINALITY

This work contains no material which has been accepted for the award of any other degree or diploma in any university or other tertiary institution and, to the best of my knowledge and belief, contains no material previously published or written by another person, except where due reference has been made in the text.

I give consent to this copy of my thesis, when deposited in the University Library, being available for loan and photocopying.

SIGNED:..... DATE:15/2/02

ACKNOWLEDGEMENTS

There are many people to thank for getting me to the end of this thesis. Firstly, I must thank my supervisors, Dr. Roger Clay and Dr. Greg Thornton, for their patience above and beyond the call of duty. Especially for their perseverance in proof reading my verbose text.

I thank Dr. Ray Protheroe and Dr. Bruce Dawson for their helpful advice since the beginning of this thesis (all those years ago). And a special thank you to Neville Wild, the technician for the High Energy Astrophysics group. I am deeply indebted to his ability to be always on call to help, no matter how trivial the question. Also I must mention the help of Mike Shorthose who managed to keep the local network up and running in times of crisis.

I appreciate the help from members of the CORSIKA collaboration, particularly Dr. Dieter Heck and Dr. Konrad Bernlohr for their assistance with the customising of the simulations in this thesis.

My stay in the department has been made all the more pleasant because of my fellow suffering students. I would especially like to thank Ken, Paddy, Steve, Gavin, Mike, Rishi, Chris, Aidan, Gail, Melanie, Hayley and Jose.

Most importantly, I thank Heidi and my mum for their enduring support. They have never stopped being as much a part of this project as myself and will be quite relieved to see its conclusion in this thesis. My deepest thanks and love for believing in me.

Finally this thesis is for my little jedi, Aayla-Jae (who began as this project ended).

Chapter 1

COSMIC RADIATION

1.1 Introduction

The origin of much of the cosmic radiation reaching the earth lies well beyond our solar system. This radiation consists mainly of atomic nuclei, and its composition is dominated at low energies by hydrogen (90%). Helium (9%) and heavier nuclei (~1%) follow with a smaller number of photons and electrons.

The study of cosmic radiation is primarily of interest to two different fields of research in physics. Firstly, the interactions of cosmic radiation (during their tortuous journey from production to their eventual detection at the earth) provide us with a natural laboratory for studying the physics of elementary particles at energies exceeding anything remotely attainable on the earth using particle accelerators (Costa 1998). In fact, cosmic ray experiments have been responsible for some of the most important discoveries in particle physics. For example, the existence of antimatter in nature was only confirmed following the discovery of the positron (Anderson 1933) in *secondary* cosmic rays in the atmosphere. More recently, the implication that neutrinos have mass (Ahmad et al. 2001), from the solution to the solar neutrino problem, has important consequences for the Standard Model of particle physics.

Secondly, the cosmic radiation comprises the only source of material from outside our solar system available for us to directly study. Cosmic ray particles collected at the

earth contain information about their site of production and their journey through the interstellar medium to us. As such, they are of great astrophysical significance. This is especially in light of the fact that, despite substantial achievements in cosmic ray research since their discovery almost a century ago, we still have no conclusive models for the origin, acceleration and propagation of these particles.

1.2 History of Cosmic Ray Physics

At the start of the 1900s, it was believed that all radiation consisted of α, β and γ-"rays". The discovery of a penetrating extra-terrestrial radiation was made in 1912 (Hess 1912). Viktor Hess carried ion chambers on manned balloon flights up to a maximum altitude of 5 km. After a decrease away from ground effects up to an altitude of 2 km, the measured ionisation rate due to this radiation exhibited a dramatic and continual increase with altitude. Kölhorster (1913) later confirmed this and extended his measurements beyond 9 km in altitude.

These "cosmic rays" (named by Millikan in 1925) were initially assumed to be energetic γ-rays due to their great penetrating power. In 1932, Blackett & Occhialini (1933) used a series of aligned Geiger-Mueller detectors in coincidence to trigger the operation of their cloud chamber. The observed particle tracks quickly proved that the radiation measured at ground level actually consisted of charged particles (and not γ-rays). During the 1930s, Clay (1934) and Compton (1933) independently confirmed this by investigating the variation of sea level cosmic ray intensity with latitude. The earth's magnetic field deflects incoming charged particles more readily at the equator than at higher latitudes for a given particle momentum. This results in an intensity

variation known as the "latitude effect". Rossi (1930a) predicted the existence of an "east-west asymmetry" for the radiation based on its charge polarity. An increase in cosmic rays from the west was later observed by Johnson (1940). He concluded that virtually all of the primary cosmic radiation must consist of positively charged particles.

Rossi (1930b) measured the absorption of cosmic rays in varying layers of lead. He found the intensity of the radiation actually increased for a small thickness of lead. This prompted the idea that these particles observed at the ground might be secondaries in showers produced high in the atmosphere by a far more energetic primary radiation. Skobelzyn (1929) was the first to observe such showers of particles in a cloud chamber. Auger (1939) measured the characteristic lateral extent of such air showers to be about 300 m. When combined with the particle density in his detector, this suggested energies for the primary radiation of ~ 10^{15} eV.

1.3 Energy Spectrum of Cosmic Radiation

We now know that the maximum energy of primary cosmic radiation extends beyond 10^{20} eV. It cannot be measured directly below 10^{9} eV due to effects of the solar wind. The measured spectrum follows a remarkably uniform power law relationship across this vast range of energy ($10^{9} - 10^{20}$ eV). The fact that this is not a Maxwell-Boltzmann distribution implies that the acceleration mechanism for these cosmic rays is non-thermal. The *all-particle spectrum* above 10^{11} eV is shown in figure 1.1. It is commonly presented as either a *differential* spectrum (the number of particles with energy between E and $E + dE$), or an *integral* spectrum (the number with energy exceeding E).

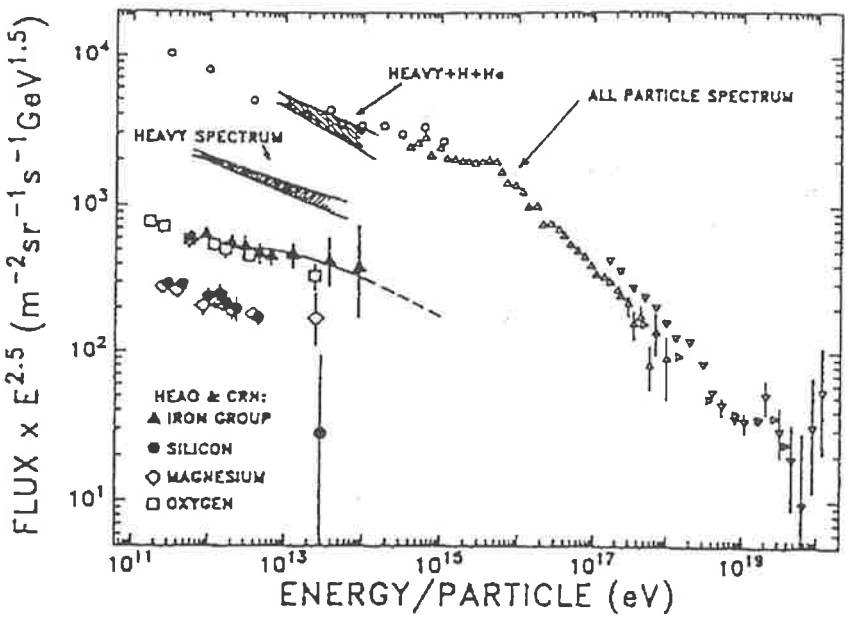

Figure 1.1: The primary cosmic ray energy spectrum displayed as a differential spectrum (from Swordy et al. 1993). For convenience in examining the structure in this spectrum, the flux has been multiplied by energy to the power of 2.5. This process can have the undesirable effect of correlating measurement errors in the two axes.

Some structure is evident in the spectrum. At energies below 10^9 eV, the intensity of extra-heliospheric cosmic rays suffers modulation by magnetic fields carried in the solar wind as it flows out through the solar system. The true interstellar spectrum at these energies is therefore impossible to completely determine from within the solar system, although some departure from the steep power law relationship must occur at low energies.

Between 10^{15} eV and 10^{16} eV the spectrum appears to steepen with the differential exponent decreasing from –2.7 to –3.1. This gives rise to a *knee* in the spectrum observed by many ground-based experiments. The most popular explanation attributes this to the maximum energies attainable by the cosmic ray acceleration "engine" for a

given mass primary. Alternatively, it might be due to an energy dependent leakage of cosmic rays out of the Galaxy. It may even indicate a breakdown in our understanding of hadronic interactions at these energies, though no experimental data so far show a need to be understood through the use of a radically different interaction model. If we neglect this last possibility, the other models predict a shift in composition from light to heavy as the energy passes through the knee. We will discuss composition measurements at the knee in section 1.6.2.

The spectral slope appears to reduce again above 10^{19} eV creating an *ankle*. This feature in the spectrum may represent the addition of an extra-galactic source of cosmic rays. The *Greisen-Zatsepin-Kuz'min (GZK)* cut-off (Gresien 1966; Zatsepin & Kuz'min 1966) sets the maximum distance a particle of such energy might travel in the intergalactic medium before being attenuated by the microwave background radiation. No evidence of the resulting predicted cut-off at ~ $5x10^{19}$ eV appears in the spectrum. This implies that, if there are extra-galactic sources for these cosmic rays, they must lie within 100 Mpc from us. Recently, the AGASA array has detected an excess of 10^{18} eV particles from an object located near the galactic centre (Hayashida et al. 2001). Whether the ankle is real or simply an artefact of the low statistics of the observed highest energy particles is not completely certain. We must wait for the next generation of large-scale particle detectors such as the Auger observatory (Pierre Auger Design Report 1995) to answer such questions.

1.4 Origin and Acceleration of Cosmic Rays

The location of the acceleration sites of cosmic radiation and the nature of the acceleration mechanisms themselves are still largely unknown. Realistic models for particle acceleration to the highest energies include some of the highest energy processes ever conceived and push our knowledge of nuclear and particle physics to its limits. Current opinion for the most likely acceleration mechanism points to supernovae (SN) for acceleration within the Galaxy, and radio galaxies as the preferred extra-galactic sources.

1.4.1 Normal Supernova Explosions into the ISM

Supernova remnants (SNR) have been popular candidate sites for the acceleration of cosmic rays to high energies since the work of Colgate & Johnson (1960). The galactic SN energy output appears to be sufficient to explain the predicted cosmic ray luminosity ($\sim 10^{41}$ erg s^{-1}). This available SN power is inferred from observations of the radio synchrotron emission from accelerated electrons in the SNR (Allen et al. 1999).

Relativistic particles can undergo diffusive acceleration via continual scattering across the SN shock wave boundary. This is referred to as 1st order Fermi acceleration since the fractional energy gain upon each shock crossing is proportional to the shock velocity. Fermi (1949) originally proposed an alternative theory for cosmic ray acceleration, which involved multiple collisions with randomly moving, magnetised clouds in the ISM. However, the energy transfer from this 2nd order Fermi acceleration mechanism was too inefficient to explain the acceleration of particles to the highest

energies. We assumed here that the relativistic particles injected into the shock were already present in the ISM. The origin of this material is still uncertain. Recent evidence from ACE (Yanasak et al. 1999) suggests that these particles are from SN ejecta that have been allowed to mix in the ISM over timescales greater than 10^6 yr.

Perhaps the most appealing feature of shock acceleration is that the energy dependent probability for cosmic rays escaping the acceleration region of the shock produces a power law. The differential spectrum of accelerated particles leaving the shock is estimated to be of the form, $E^{-\alpha}$, where α lies in the range 2.1 – 2.4. This agrees well with the shape of the measured cosmic ray spectrum once propagation losses have been removed. The highest particle energies attainable are thought to occur at the end of the Sedov phase of the shock after energy losses due to adiabatic expansion have occurred. The maximum particle energy achievable depends strongly on the density of the local ISM and, in the most tenuous regions, acceleration up to an energy, Zx100 TeV, (where Z is the charge of the particle) may be possible (Lagage & Cesarsky 1983). This mass dependence naturally predicts an enrichment of heavy nuclei at the knee.

While the preceding argument may appear to be compelling, we still have no direct evidence that acceleration of cosmic ray hadrons actually takes place in SNRs. The detection of π^0 decay γ-rays from nearby SNRs would provide a direct confirmation of this. Unfortunately, existing experiments are unable to discriminate between γ-rays that are due to π^0 decay and those from Inverse Compton emission. It is expected that the increased sensitivity, angular resolution and spectral range of new experiments such as GLAST (Kniffen et al. 1999), VERITAS (Krennrich et al. 1999),

HESS (Hoffmann et al. 1999) and CANGAROO-III (Enomoto 1999) will be successful in identifying this π^0 decay signal if it exists.

1.4.2 Cosmic Ray Acceleration Beyond the Knee

The particle energy range obtained by SN shock acceleration can be extended to energies well above the knee if the SN explodes into the stellar wind of a neighbouring star or its own predecessor star (Ip & Axford 1992). Such sources require massive stars with strong winds. Possible candidates include OB associations and Wolf Rayet stars.

The energies attained by this acceleration are again rigidity dependent, so we expect a heavier composition at higher energies. The spectrum of accelerated particles is given as $E^{-2.3}$ below some critical energy, Zx700 TeV (Volk & Biermann 1988), and steepening to $E^{-2.7}$ above (up to a maximum energy of Zx70 PeV). This spectral bend is due to the effect of turbulence in the ISM on the acceleration efficiency of such particles (Biermann 1994). Below this critical energy, the gyro-radii of these particles are small enough so that they experience particle drifts due to turbulence. The bending appears to correspond with the shape of the knee in the cosmic ray spectrum shown in figure 1.1. This model also predicts a small flattening of the cosmic ray spectrum just prior to the knee.

Other galactic models suggest alternative sites for accelerating particles to energies beyond the knee. These include a galactic wind shock (Jokipii & Morfill 1987); re-acceleration of low energy cosmic rays in the ISM (Ip & Axford 1992); and the high magnetic fields of fast rotating pulsars (Bednarek & Protheroe 2001). Extra-galactic sources are also potential sites for the acceleration of cosmic rays to higher energies.

Protheroe & Szabo (1992) suggest that there might even be an extra-galactic contribution at the knee. They have shown that models of accretion shocks in Active Galactic Nuclei (AGN) are capable of producing a particle spectrum that fits the shape of the knee well, but which does not extend beyond the ankle. The composition of such a component must consist entirely of protons. Any heavier nuclei would undergo photodisintegration before escaping the central region of the AGN.

The highest energy cosmic rays (above 10^{19} eV) possess extremely large gyro-radii. This is seen as a strong argument for an extra-galactic origin. It may therefore be possible to trace these near-straight trajectories back to a region close to their source. Any observational evidence of such an anisotropy is limited by the low event statistics at these energies. One favoured location for extra-galactic sources places them in the hot spots of powerful Fanaroff Riley Class II radio galaxies (Rachen & Biermann 1993). These are capable of explaining the observed intensity, composition and spectrum of such particles.

1.5 Cosmic Ray Propagation

At low energies, the relative abundance of different mass cosmic rays is very similar to that of the solar system material, with a few exceptions. Some groups of cosmic ray species, such as LiBeB and ScTiVMn, are many orders of magnitude greater in abundance in the cosmic radiation because of *spallation* processes. Heavier nuclei collide with protons in the interstellar medium, which has a density of $\rho_{ISM} \sim 1$ H atom cm^{-3} in the galactic disk, and fragment into lighter products. To a first approximation, the energy per nucleon of the cosmic ray primary is conserved in the

collision. Therefore the measured all-particle spectrum (in terms of energy per nucleon) shows no losses due to spallation.

Spallation products provide us with tools for determining the average amount of matter traversed by cosmic ray primaries. The ratio of the number of fragmented secondaries to primaries in the measured cosmic radiation defines the quantity of matter along the path of the cosmic ray primary from its point of origin to its detection at the earth. Assuming the primary is confined to the galactic disk, this defines a path length of the order of 1 Mpc. It must be noted that this is only a lower limit if the cosmic ray spends part of its lifetime in the lower density galactic halo.

An alternative estimate of cosmic ray "age" may be obtained from certain unstable cosmic ray isotopes like Be^{10} (Garcia-Munoz et al. 1977), which decay with a half-life comparable to their confinement time in the Galaxy. Recent measurements of four cosmic ray "clocks" (Binns et al. 1999) are all consistent in defining a confinement time of about 20 Myr. Combining this with the path length estimated above, we get a measure of the mean density of the confinement region ($\rho_{mean} \sim 0.2$ H atoms cm^{-3}) much smaller than the density in the disk. This suggests that cosmic rays probably spend much of their life in the galactic halo.

The simplest model for confinement is the *Leaky Box Model* (Peters 1961). Here, charged cosmic rays are assumed to diffuse freely throughout the Galaxy spiralling around magnetic field lines. The gyro-radius of each particle depends on its *rigidity*, which is roughly proportional to energy per nucleon. The observed cosmic ray secondary to primary ratio decreases with increasing energy. This is consistent with an

energy dependent leakage of cosmic rays out of the Galaxy. At high energies, where the rigidity, R, exceeds 4 GV, the mean free path for escape may be estimated from (Ptuskin et al. 1999) as

$$\lambda_{esc} \sim R^{-0.6} \tag{1.1}$$

At the highest energies, the gyro-radius will exceed the thickness of the galactic disk and the particle will escape into the intergalactic medium. Removing the energy dependence of confinement from the measured cosmic ray spectrum, $E^{-2.7}$, we derive a source spectrum, $E^{-2.1}$. Even if the source spectrum was well described by the same power law for all primaries, the shape of the measured energy per nucleus spectrum for each cosmic ray species will still differ because of the rigidity dependent escape probability.

Other confinement models include the Halo Diffusion Model (where cosmic rays escape at the extremity of the halo); the inclusion of winds away from the galactic disk (such that diffusion becomes less energy dependent); and the possibility of continual re-acceleration of low energy cosmic rays during propagation. So far no clear evidence exists for discriminating between these models (Ptuskin et al. 1999) but they are expected to be sensitive to isotope measurements in the range 1 – 10 GeV nucleon^{-1}. It is hoped that future results from the ISOMAX experiment (de Nolfo 1999) will be useful in rejecting some of these models.

Strong & Mosalenko (1998) have argued convincingly for re-acceleration as the only model capable of describing the observed spectral shape of the B/C ratio

at 1 GeV nucleon^{-1}. Re-acceleration of cosmic rays also predicts shorter path lengths. The decay of heavy long-lived isotopes (such as V^{49}) by electron capture gives us information on the matter traversed by the cosmic ray. Further analysis of heavy isotope data from ACE (Mahan et al. 1999) may provide enough evidence to support or reject this model.

1.6 Composition Experiments

The cause of the knee in the energy spectrum is thus still uncertain. It may indicate limits in the acceleration mechanism or be due to a propagation effect. Both alternatives are rigidity dependent, although the Leaky Box Model appears to be too simple a model to explain the shape of the knee. The main aims for experiments operating at 10^{14} – 10^{17} eV include: locating the position of the knee with greater precision; studying any fine-scale structure present; and estimating changes in the mass composition across this energy range. This information is vital for placing constraints on acceleration and confinement models, and identifying the source of these energetic particles.

First inferred from shower size spectra in the 1950s (Kulikov & Khristiansen 1958), the knee has been observed in all air shower measurements at high energies. The spectral break is a fairly smooth feature and no evidence of multiple knees from individual mass components has so far been convincingly observed. Above the knee there is a lack of observed anisotropy. This causes problems in trying to understand galactic confinement at high energy. Simply extrapolating the escape time of cosmic rays to energies greater than 10^{15} eV produces an escape length on the order of the thickness of

the galactic disk. Therefore a significant measurable anisotropy increasing with energy should be seen as we approach the knee. However, the maximum excess in any direction is found to be only a few percent.

1.6.1 Direct Measurements

Detectors on high altitude balloons or satellites outside the atmosphere can be used to directly study the primary cosmic radiation. The energy and mass of each particle can be determined with some confidence on an event-by-event basis. These measurements become impractical above 10^{14} eV due to the steep energy spectrum and the necessarily small collecting area of the detector. At higher energies, details of the primary radiation must be inferred from ground-based experiments studying air showers.

The first successful direct measurements of the cosmic ray energy spectrum were made by the PROTON series of satellites (Grigorov et al. 1970). Their study of the proton spectrum over 0.1 – 10 TeV showed a break at about 2 TeV (Grigorov et al. 1972). This break has not been confirmed in later experiments (see below). Emulsion chamber experiments launched on balloons by the JACEE (Asakimori et al. 1998) and RUNJOB (Apanasenko et al. 1995) groups now provide the most comprehensive datasets available for cosmic rays at these energies. The JACEE data were taken from 14 successful flights (1979 – 1995). Less than half of the data from the 10 RUNJOB flights (1995 – 1999) have been analysed so far and their current dataset is significantly smaller than that of JACEE.

A standard JACEE detector comprises three chambers as shown in figure 1.2. The primary section employs a series of nuclear emulsion plates to determine the species of

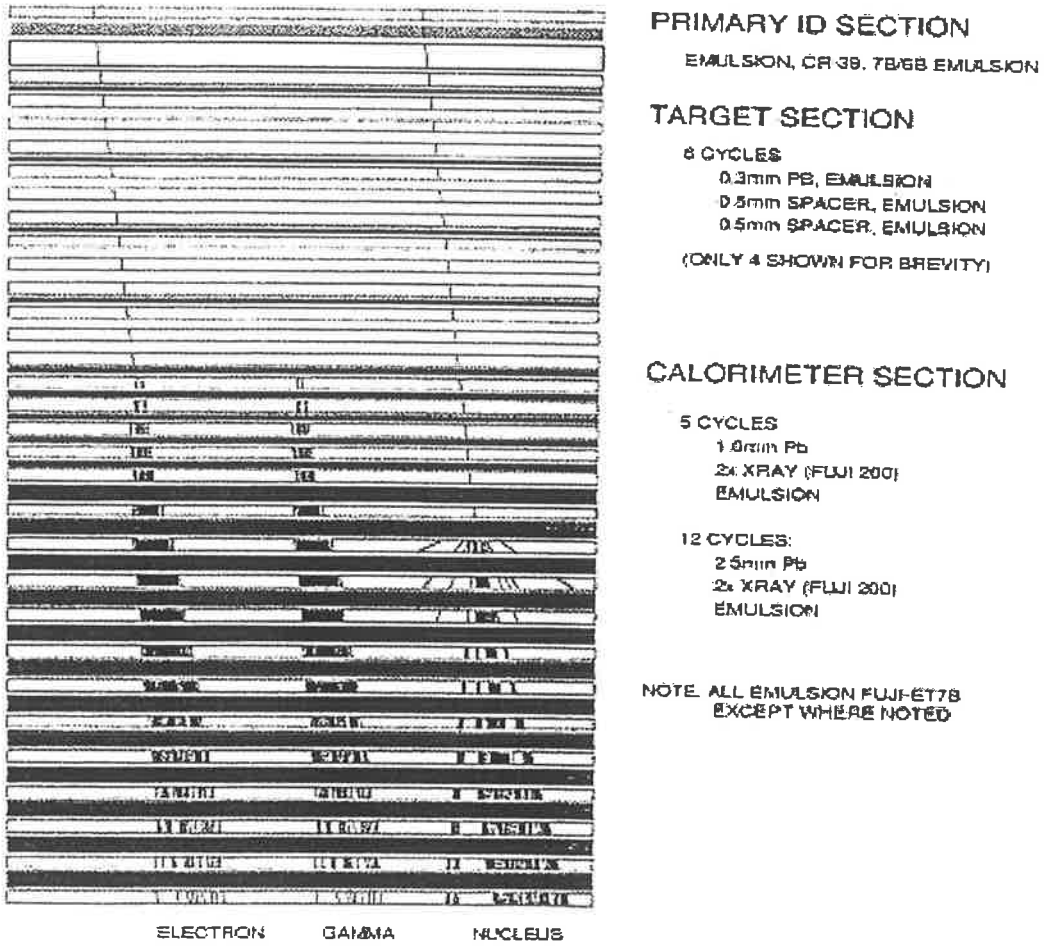

Figure 1.2: A standard emulsion chamber used in a JACEE flight (from Asakimori et al. 1998).

the cosmic ray primary via its charge. A target region is included to maximise the probability of nuclear interaction for the cosmic ray. Finally, the emulsion-X-ray film calorimeter follows the tracks of secondary electromagnetic cascades and is able to provide a measure of the primary energy. For high energy, emulsion experiments, calibration of this type of detector is non-trivial. Coupled with the low cosmic ray event statistics available at these energies, uncertainties in the determination of primary energy can range as large as 25 – 50%.

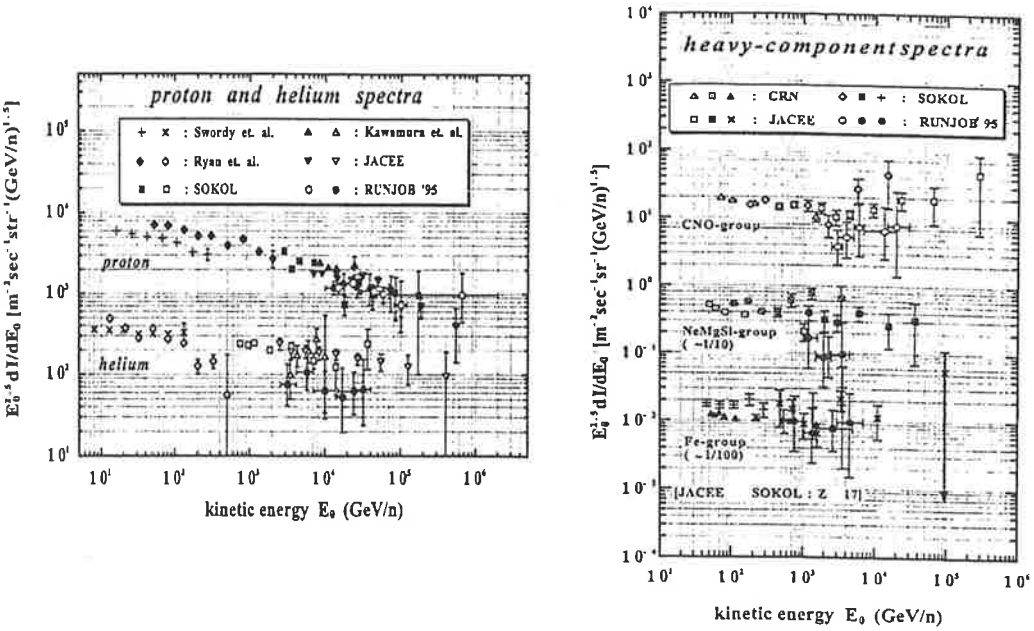

Figure 1.3: (a) Differential energy spectra for proton and helium as measured by various experiments; and (b) Differential energy spectra for CNO, NeMgSi and iron groups (from Castellina 2001).

H and He spectra have been well studied by both JACEE and RUNJOB. These results are summarised in figure 1.3(a). There is general agreement regarding the shape of the proton spectrum up to at least 100 TeV with no evidence of any break such as the one found by PROTON. The results for He are less consistent. RUNJOB finds a steeper spectrum than JACEE (similar in slope to their H spectrum). Their most recently analysed data (Anapasenko 2001) show less discrepancy, although they claim that the spectral difference is not simply due to the lower statistics of their He dataset. The measured fluxes of the heavy component groups CNO and NeMgSi are even less certain. The reported spectra from JACEE and RUNJOB differ by a factor of two. However, their Fe results do appear to be in agreement. The differential spectra of these components are displayed in figure 1.3(b).

The JACEE dataset, in addition to benefiting from larger statistics, is probably more reliable as a result of the detector's excellent proton/helium discrimination (nearly 100%). Charge discrimination (particularly between proton and helium events) can be problematic for other, similar experiments including RUNJOB. Thus, the composition results for the experiment described in this thesis will be directly compared with cosmic ray spectra derived from the JACEE data.

A lack of structure in the measured all-particle spectrum (up to 10 TeV nucleon^{-1}) is taken as evidence that the acceleration mechanism is likely to be the same for each cosmic ray species up to the knee. More measurements above 100 TeV are needed to make the interpretation of air shower experiments less model dependent. JACEE has only 4 events above 1 PeV. Any estimation of mean mass from this is too vague to be useful. An extension of the directly measured spectrum will also determine whether any change in hadronic interactions occurs at the knee.

1.6.2 Ground-Based Experiments at the Knee

Conveniently, just at the energies where direct measurements become impractical, secondary particles from air showers (initiated by these primaries) are given enough energy to reach the ground and to be readily measurable in coincidence detectors. We will have more to say about these air showers and their components in chapter 2. Measurements of such particles by large-scale ground-based detectors are used to reconstruct shower "observables". These relate to the energy and mass of the primary, though not independently.

The different types of air shower experiment in use near the knee can be broadly categorised by their choice of which observables are measured: (1) by estimating shower size from direct sampling of the shower front; (2) through the study of atmospheric Čerenkov signals; and (3) from utilising underground measurements of the muon component. Each class of detector has its own merits for yielding information on the energy and mass of the primary radiation. It is likely that a combination of these techniques will be needed to fully understand the knee. So many cosmic ray experiments are being designed or are currently in operation that it would be impractical to list details of them all. Instead we shall focus our attention on two experiments that have recently yielded promising results.

- The ***KASCADE*** (KArlsruhe Shower Core and Array DEtector) detector complex (Doll et al. 1990) consists of a 200x200 m^2 array of scintillation detectors (containing muon and electron counters), a central detector (including a multi-segmented hadronic calorimeter), and a muon tracking detector. The threshold energy for this installation is $4x10^{14}$ eV. The lateral particle density distribution of each shower component is measured and integrated to define truncated particle shower sizes. The truncation has been implemented to remove the systematic uncertainties in defining the lateral distribution outside the physical area of the experiment. Information on arrival directions and shower core positions are obtained from the scintillation array.

From the reasonable assumption that the muon and electron components contain nearly all of the shower's energy, the primary energy is then determined by

$$E \cong a \log N_{\mu}^{tr} + b \log N_{e}^{tr} \tag{1.2}$$

where N_{μ}^{tr} is the truncated muon shower size, N_{e}^{tr} is the truncated electron shower size, and a and b are weights determined from simulations (Kampert 2001). In addition, a reliable estimate of primary mass may be obtained from the parameter

$$Y_{ratio} = \frac{\log N_{\mu}^{tr}}{\log N_{e}^{tr}} \tag{1.3}$$

A recent multivariate analysis (Roth et al. 1999) has made use of all these measured observables to provide strong evidence that the shape of the knee is due to the turnover in the proton spectrum alone. Above this energy, the mean mass is observed to increase with energy. This is inferred from "electron poor" (i.e. iron-like) showers selected by using an appropriate value for equation 1.3. These exhibit no knee in their shower size spectra at energies where it is clearly visible in "electron rich" showers.

- In recent years, much interest has been generated in combining well established arrays of particle detectors with atmospheric Čerenkov detectors to maximise the information available in a given shower. The ***HEGRA*** project (Aharonian et al. 1998) is a prime example, running six imaging

atmospheric Čerenkov telescopes (for γ-ray astronomy) with three arrays exploring the primary energy spectrum and mass composition in the range 0.3 – 10 PeV. These include the wide-angle Čerenkov array AIROBICC (Karle et al. 1995), a 200x200 m^2 scintillation array, and the Geiger tower array (Rhode et al. 1996). The Čerenkov and scintillation arrays are used independently to reconstruct arrival direction and shower core location for each shower triggering the installation.

For core distances between 20 and 100 m, the Čerenkov lateral distribution is well described by an exponential (Patterson & Hillas 1983a). AIROBICC measures the slope of the photon density distribution in this range. From it, it is possible to estimate the distance to shower maximum, d_{max}, and thus the energy per nucleon (independent of primary mass). The mass can then be extracted from the shape of the distribution of penetration depths. Unfortunately, the absolute calibration of AIROBICC detectors still depends on an assumed mass composition. An NKG (Nishimura, Kamata & Greisen) fit (see equation 2.6) is applied to the particle densities measured by the scintillation array at detector level to estimate shower size. This, combined with d_{max}, allows the primary energy to be estimated.

Their composition results below the knee are consistent (Arqueros et al. 2000) with direct measurements of the fraction of light components (H and He) at 100 TeV as summarised in Watson (1997)

$$\frac{H + He}{All} = 0.54 \pm 0.08 \tag{1.4}$$

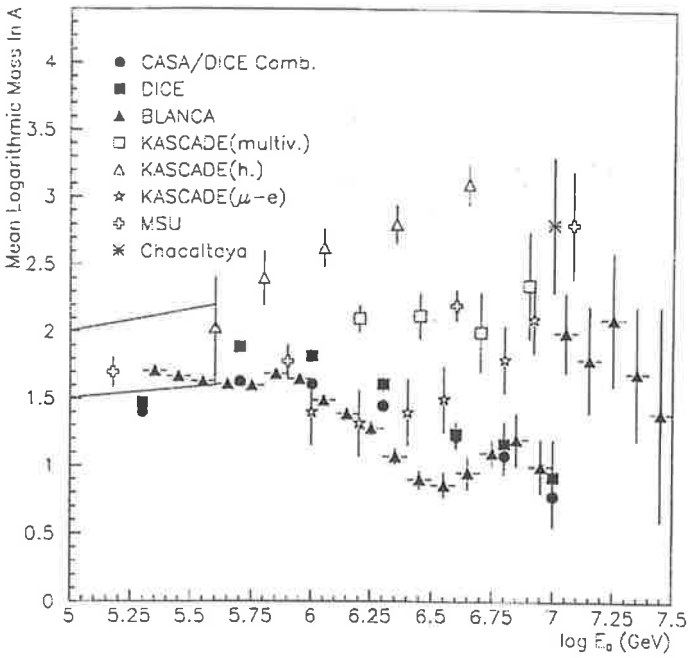

Figure 1.4: Mean logarithmic mass as a function of primary energy in the knee region. The straight lines enclose the region covered by direct measurements (from Castellina 2001).

They find no evidence for a change in the energy spectrum from TeV energies right up to the knee (Aharonian et al. 1999). A gradual enrichment of heavy nuclei above 1 PeV seems possible from their data but no drastic change in composition at the knee has been observed.

All experiments generally agree on the location of the knee at 3 – 5 PeV but there is still much confusion regarding the composition in the region about the knee. This is best represented in figure 1.4 where the estimated mean mass is plotted as a function of energy for a variety of air shower experiments. Except for the Čerenkov experiments, most results indicate a shift in mass from light to heavy above the knee (but not all on the same scale). The greatest uncertainty in interpreting data in the knee region and beyond lies in the choice of hadronic interaction model used in shower simulations.

Currently, the QGSJET model (Kalmykov & Ostapchenko 1993), based on the quark-gluon-string model of particle interactions, appears to give the best fit to air shower data. Muon and electron components are well described but the model has been found to overestimate the number of hadrons in 10^{16} eV showers (Antoni et al. 1999).

Chapter 2

EXTENSIVE AIR SHOWERS

2.1 Introduction

The study of cosmic ray particles becomes more difficult with increasing energy. As we have seen in section 1.6.1, direct measurements using satellite and balloon-borne experiments are limited by small collecting areas and the steeply descending energy spectrum of these particles. An alternative detection method can be realised by incorporating the atmosphere into our detector as a collecting medium for these particles. The *extensive air showers (EAS)* of secondary particles generated in the atmosphere may then be studied with ground-based detectors. As the name suggests, these particle cascades have a broad lateral extent. This provides sparsely placed detectors on the ground with collecting areas sufficiently large enough to study high energy cosmic rays in a practical way.

A primary cosmic ray with sufficient energy entering the atmosphere will collide with atmospheric nuclei and produce secondary particles. The secondaries created in each successive collision continue to interact with the atmosphere producing more particles. This cascading effect of particle interactions is the "engine" driving the growth of an air shower. The particles are distinctly separated into three families based on the shower's physical structure: the *nuclear component* containing the primary cosmic ray (or its remnants), secondary nucleons and anti-nucleons, kaons (K) and pions (π); the soft,

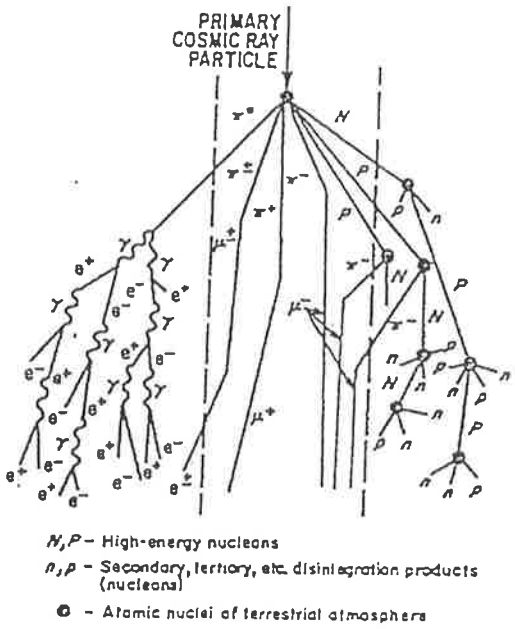

Figure 2.1: A schematic picture of cascade development showing the different shower components (from Venkatesan 1990). Neutrinos from pion and muon decay and kaons have been omitted for clarity.

electromagnetic component made up of photons, positrons and electrons; and the hard, penetrating *muon component*. These are described qualitatively in figure 2.1.

2.2 Structure of Cosmic Ray EAS

2.2.1 The Nuclear Component

The thickness of the atmosphere as an absorber is about 1000 gcm^{-2} and the interaction length for a proton is typically $\lambda = 80$ gcm^{-2}. The proton will thus not travel far before colliding with the nuclei of atmospheric molecules. The secondary particle production in each collision occurs via two main processes. *Fragmentation* describes both the secondary nucleons knocked out of the atmospheric nuclear targets and any fragments of the cosmic ray primary. The relativistic velocity of the primary causes the secondary

nucleons to be beamed in roughly the same direction. Their limited lateral spreading defines the *core* of the shower. Energy loss occurs through subsequent collisions producing pions and kaons. When particle energies fall below that necessary for further particle production (~ 1 GeV), ionisation losses become important and the secondary nucleons are absorbed into the surrounding atmosphere.

The particle production of kaons and pions is called *pionisation*. Each inelastic collision releases about half of the particle's energy in the form of kaons ($K^{\circ}, \overline{K^{\circ}}, K^{+}, K^{-}$) and pions ($\pi^{\circ}, \pi^{+}, \pi^{-}$). These mesons fuel the other shower components. Kaons are produced at about 10% the rate of the pions, and interact or decay to produce more pions, muons (μ) and electrons (e). With this in mind, we shall only concentrate on the pion interactions. The three species of pion are produced in roughly equal numbers at sufficiently high energies and their decay process is charge dependent. Charged pions decay into muons, and neutral pions into gamma rays giving rise to the electromagnetic component.

2.2.2 The Electromagnetic Component

The gamma rays, electrons and positrons of the electromagnetic component make up the majority of the particles in an EAS. It is no surprise then that they dominate the bulk character of the shower in its observed lateral extent and longitudinal development. "Electromagnetic" cascades of these particles are mainly initiated by gamma rays from the decay of 0.1 – 1 TeV neutral pions (Allan 1971).

$$\pi^{o} \rightarrow \gamma + \gamma \tag{2.1}$$

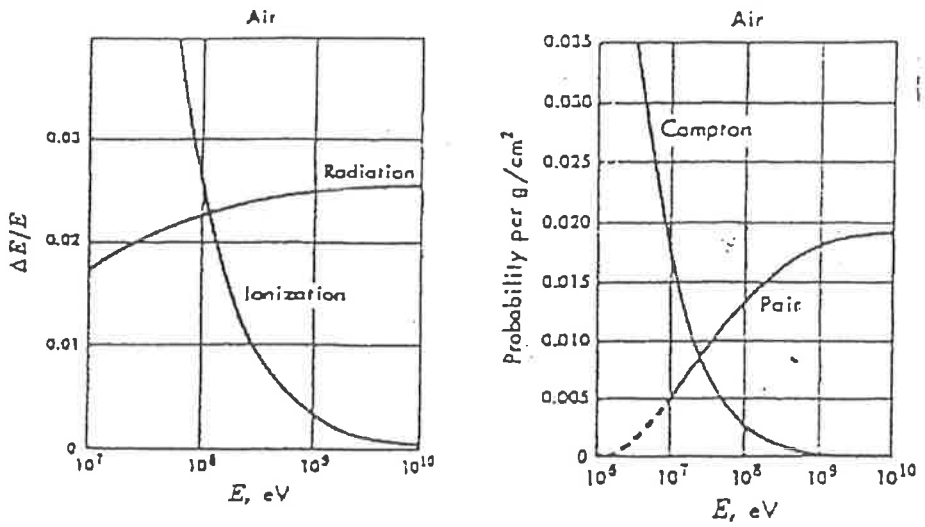

Figure 2.2: (a) Fractional energy loss per gcm^{-2} of electrons due to ionisation and bremsstrahlung processes in air; and (b) The energy dependent probability that a photon will either suffer compton scattering or pair produce in a track length of 1 gcm^{-2} (from Rossi 1964).

The half-life is only 8×10^{-17} s, so there is very little chance for the neutral pion to interact before decaying.

Two main processes characterise the development of an electromagnetic cascade:

- ***Bremsstrahlung*** production of gamma rays through the acceleration of electrons in the coulomb field of an atmospheric nucleus.

$$e^{\pm} \rightarrow e^{\pm} + \gamma \tag{2.2}$$

After a single radiation length, X_o = 37.15 gcm^{-2} in air (Linsley 1985), an electron typically loses ~ 63% of its energy to this "braking radiation". This process does not continue once electron energies drop below 100 MeV since ionisation losses begin to take over (see figure 2.2(a)).

- ***Pair Production*** of electrons and positrons via gamma ray interactions with the field of an atmospheric nucleus.

$$\gamma \rightarrow e^{+} + e^{-} \tag{2.3}$$

For many shower aspects there is no physical need to differentiate between electrons and positrons since they only differ in charge. From here on they will jointly be referred to as electrons. The interaction length for this process is 9/7 X_o. The chance of pair production occurring is reduced at energies less than 20 MeV, where gamma rays are more likely to undergo Compton scattering instead (see figure 2.2(b)).

It is clear that the interaction lengths of these processes are very similar. As we shall see later, this fortunate result allows us to greatly simplify the modelling of electromagnetic cascade development.

Throughout their journey, EAS electrons suffer multiple coulomb scattering off atmospheric nuclei. This scattering is energy dependent and the mean square scattering angle for an electron with energy, E_e, is well described by (Gaisser 1990)

$$d\theta_s^{\,2} = \left(\frac{E_s}{E_e}\right)^2 dx \tag{2.4}$$

where $E_s = 21$ MeV and dx is the distance travelled in units of X_o.

The inverse relationship between energy and scattering angle immediately suggests an important fact. The shower core will contain mostly energetic electrons since they will experience only a small lateral departure from central region of the EAS. Low energy electrons are scattered away from the core and travel a shorter distance before being

attenuated. As an example, a 100 MeV electron at sea level will be deflected by about 12° in a single radiation length.

The lateral extent of the electromagnetic component (and thus the total EAS) will be dominated by this continual scattering. The density of shower particles at a distance r from the core

$$\rho(N_e, r) = \frac{N_e f_{NKG}(r)}{r_o^2} \text{ m}^{-2} \tag{2.5}$$

is characterised by the Moliere radius, $r_o = (E_s / E_c) X_o = 79$ m (at sea level), the NKG (Nishimura, Kamata & Greisen) function, $f_{NKG}(r)$, and the total number of EAS electrons, N_e. Moliere (1948) made the first attempt at deriving the lateral distribution function but his calculations were only valid at shower maximum. Nishimura & Kamata (1951) extended his work to explain the lateral spread at all stages of EAS development. Based on the observed lateral distributions of cosmic ray EAS, Greisen (1966) fitted an empirical approximation to their model. The NKG function, described as a function of shower age, s, with r measured in units of r_o, can be written as

$$f\left(\frac{r}{r_o}\right) = C(s)\left(\frac{r}{r_o}\right)^{s-2}\left(\frac{r}{r_o}+1\right)^{s-4.5} \tag{2.6}$$

with a normalisation factor

$$C(s)=\frac{\Gamma(4.5-s)}{2\pi\Gamma(s)\Gamma(4.5-2s)} \tag{2.7}$$

The shower "age" describes the state of shower development at a given point of observation. It is a monotonically increasing function, with $s = 0$ at the beginning of the cascade, $s = 1$ at shower maximum, and $s = 2$ when the shower has decayed to leave only a single particle remaining. As a function of atmospheric depth, x, and shower maximum, x_{max}, where both are measured in radiation lengths, it can be expressed as

$$s=\frac{3x}{x+2x_{\max}} \tag{2.8}$$

2.2.3 The Hard Component

The interaction length for charged pions is 120 gcm^{-2}, which is about 2 km for a typical height of shower maximum. The decay length depends strongly on energy and is equal to $2(E/3\text{x}10^{10})$ km where E is the pion energy in eV. Decay is the most likely mechanism, for energies below 30 GeV, producing muons and their associated neutrinos.

$$\pi^{+}\rightarrow\mu^{+}+\nu_{\mu} \tag{2.9a}$$

$$\pi^{-}\rightarrow\mu^{-}+\bar{\nu}_{\mu} \tag{2.9b}$$

For near-vertical showers with energies less than 100 TeV, these "unaccompanied" muons are the only particles that can be directly measured at sea level. As such they are often called the hard, or penetrating, component of an EAS.

They have a lifetime of 2.6×10^{-8} s and lose energy through ionisation at a constant rate of about 2 MeV per gcm^{-2}. Thus it might be expected that they should all decay in the 1000 gcm^{-2} of atmosphere before reaching the ground. However, those with Lorentz factors greater than 20 (muon energies $E_\mu > 2$ GeV) will experience relativistic time dilation effects large enough to let them survive to the ground. Low energy muons will decay in flight to produce electrons that contribute very little to the electromagnetic component.

$$\mu^+ \rightarrow e^+ + \nu_e + \bar{\nu}_\mu \tag{2.10a}$$

$$\mu^- \rightarrow e^- + \bar{\nu}_e + \nu_\mu \tag{2.10b}$$

The rest mass of a muon is 106 MeV and it is only ~ 0.5 MeV for an electron. More energy is required from the EAS to generate muons so they are mostly produced in the early stages of shower development. Energetic muons are weakly interacting and thus largely insensitive to coulomb scattering. Although they are typically created with relatively small transverse momenta (~ few 100 MeV/c), they can still achieve a large lateral dispersion due to the long path length between their production height and the ground. The muon lateral distribution is flatter than that of the electromagnetic component and has been described by Greisen (1960) as

$$\rho_\mu(r) \propto r^{-0.75}\left(1+\frac{r}{k(s,\theta_z)}\right)^{-2.5} \tag{2.11}$$

where k is a function of both shower age, s, and zenith angle, θ_z.

2.3 Electromagnetic Cascades

As mentioned previously, the electromagnetic particles in a typical EAS greatly outnumber the hadronic and muon components. Hence, many large-scale features of EAS development can be observed from a study of electromagnetic cascades on their own.

The development of an electromagnetic cascade can be understood in a general way with the help of a simplified model first suggested by Heitler (1935). The inclusion of every relevant process in the cascade is too complex for an analytical treatment. Various approximations are available to simplify this. The most basic is "Approximation A" (Rossi & Greisen 1941) which ignores the Compton scattering of photons and ionisation losses of electrons.

We will begin by considering an electron, with energy, E_o, that radiates half of its energy away as a photon of energy, $E_o/2$, after traversing an atmospheric depth of $X_o \ln 2$. Assuming that the path lengths of bremsstrahlung and pair production are to a good approximation equivalent, the photon will then travel the same distance before pair producing into two electrons each with energy, $E_o/4$. The shower thus grows exponentially with each radiation length. At a depth, $x \ln 2$, (where x is measured in units of X_o), the number of electrons and photons in the cascade is

$$N(x) = e^x \tag{2.12}$$

The energy of each particle at this depth is then described by

$$E = E_o e^{-x} \tag{2.13}$$

After n interactions, the critical energy, $E_c = E_o/2^n \sim 80$ MeV is reached where the loss rates for bremsstrahlung and ionisation are approximately equal. The total number of electrons in the shower is then $N_e = (2/3)\, E_o/E_c$. This is called the shower maximum and occurs at a depth, $x_{max} = \ln (E_o/E_c)$. From this point on, ionisation losses become significant and the cascade stops growing. This is because further collisions with atmospheric nuclei only result in "knock-on" electrons, ions and photons that have energies too low to add to further cascade growth.

After x_{max} is reached, the shower particles undergo rapid attenuation. The shower decay is also exponential, and the number of particles at a depth, $x > x_{max}$, is given by

$$N(x) = N_e e^{-\Delta x/\lambda_0} \tag{2.14}$$

where $\Delta x = x - x_{max}$ and $\lambda_0 \sim 130$ gcm^{-2} is the attenuation coefficient of the shower.

While this model is quite basic, it is still able to identify some important large-scale cascade features with a great degree of accuracy, namely:

- The exponential growth of the cascade.
- The relationship of the primary energy to x_{max}.
- Rapid attenuation of the shower beyond shower maximum.

It is known that the preceding discussion underestimates the number of electrons in the shower. In this model the distribution of particle energies at a given depth is deficient

in low energy electrons. A more detailed treatment is obtained by considering "Approximation B" (Rossi 1952) which includes ionisation losses at all energies. This more accurately recreates the cascade's longitudinal development in accord with the work of Greisen (1966). The total number of electrons as a function of EAS energy, E_o, and depth, x, measured in radiation lengths is then given by

$$N_e(E_o, x) = \frac{0.31}{\sqrt{x_{\max}}} e^{x(1-\ln s)} \tag{2.15}$$

2.4 Differences Between Light and Heavy EAS

The development of an EAS is highly sensitive to the early particle interactions in the hadronic core. Any variations in the depth of the initial interaction are carried as similar fluctuations in the position of $x_{\max}$. This makes the determination of primary energy and mass from EAS measurements non-trivial. The mean free path for protons with energy, E, (taken from Dawson 1985) is

$$\lambda_p = 67.2\left(\frac{E(\text{TeV})}{100}\right)^{-0.065} \text{gcm}^{-2} \tag{2.16}$$

On average, this is larger than the interaction length for iron nuclei $\lambda_{Fe} \sim 13$ gcm^{-2}, which is nearly constant with energy (Westfall et al. 1979), and so iron primaries will tend to interact higher in the atmosphere than protons with the same energy.

The superposition model from de Beer et al. (1966) assumes that an EAS from a primary of energy, E_o, and mass, A, can be well approximated by the sum of A proton showers each with energy, E_o/A. Iron showers will develop more quickly due to the

reduced energy in each sub-shower. This model is known to underestimate fluctuations in the cascade development of real cosmic ray showers (Dixon et al. 1974). Nevertheless, the general argument is valid. So for a given energy we expect less variation in x_{max} for showers initiated by heavy nuclei.

A further consequence of the superposition model is the increased number of muons relative to the electromagnetic component present in heavy showers. This is primarily due to three effects:

- The multiplicity of secondaries produced in a high energy, hadronic collision is described roughly by Feynman scaling (1969) and so varies with $\ln E$. So, whilst the number of mesons in a single sub-shower will not vary rapidly with the energy of the shower, the summed contribution from all sub-showers will be expected to show composition dependence.

- The energies of π and K mesons created in each sub-shower will be reduced for showers with heavy primaries. So they will more readily decay into muons before interacting.

- The large rest masses of these mesons rapidly diminish the energy reservoir of a shower at the early stages of its development. The reduced energy per sub-shower means there is less energy available to go into the production of electromagnetic cascades.

The ratio of the number of muons measured at the ground to the number of electrons is observed to be a powerful indicator of primary mass. EAS experiments such as

EAS-TOP (Aglietta et al. 1999) and KASCADE have used this to show a clear increase of mean primary mass with energy above the knee (see section 1.6.2).

The lateral distribution of iron showers is broader than that of proton showers. This reflects the higher altitude of the initial interactions in the cascade. The atmospheric density there is less than at the height of a similar stage of cascade development for proton primaries of the same energy. Particles in iron showers will thus travel a greater distance before being attenuated. In addition, the lateral distribution of the muon component is intrinsically flatter than that of the electromagnetic component. An increase in the number of muons will thus make an important contribution to the lateral extent of the entire iron shower.

2.5 The Geomagnetic Field

To a first approximation, the terrestrial magnetic field may be described by a dipole centred at the earth's core and inclined at an angle of 11.5° to the axis of rotation. The field strength at the earth's surface ranges from ~ 6×10^{-5} T at the poles to less than 3×10^{-5} T near the equator. For details of the field at a specific geographic location, the reader is referred to the Handbook of Geophysics & Space Environments (1965).

Charged cosmic ray particles approaching the earth undergo deflection in the geomagnetic field as a function of their kinetic energy and charge. Störmer (1964) identified regions of threshold energy at the earth's surface based on the particle's arrival direction. In order to reach the earth (neglecting atmospheric interactions), a low energy cosmic ray particle with charge, Z, arriving vertically must have a momentum, p, satisfying the condition

$$p \geq 14.9Z\cos^4(\lambda_g)\ \mathrm{GeV c^{-1}} \tag{2.17}$$

where the geomagnetic latitude, λ_g, at the observation site is defined with respect to the equatorial plane of the geomagnetic field. From equation 2.17 we can determine that, for a given cosmic ray primary, there must exist a larger energy threshold, cp, near the equator compared to that found at higher latitudes. This is responsible for the "latitude effect" mentioned in section 1.2.

The effects of the geomagnetic field on cascade development and the lateral spread of emitted Čerenkov radiation (which will be introduced in chapter 3) were first investigated by Porter (1973). This, and later work by Browning and Turver (1977), only examined the effects of a non-varying geomagnetic field on EAS for a given location. However, the magnetic field effect experienced by shower particles is known to be strongly dependent on the orientation of field lines relative to the direction of shower development. Particles travelling perpendicular to the field lines will feel a maximum effect, while those with trajectories aligned with the direction of the field will be relatively unaffected.

The Durham group (Chadwick et al. 1999) have generated simulations of atmospheric Čerenkov pulses from γ-ray and proton initiated air showers for their γ-ray telescopes at Narrabri (30.19°S, 149.47°E). These have been used to determine possible trends in their measured data due to geomagnetic effects. They conclude that with an increasing transverse magnetic field:

- There is an increase in energy threshold for the detector. The event rate at a set trigger threshold will then decrease.

- Čerenkov angular images are expected to widen along the geomagnetic E/W line. This reflects the lateral spreading of the shower particles.

- Delays in the arrival times of Čerenkov photons are expected and the observed pulse shape will appear wider.

Chapter 3

ATMOSPHERIC ČERENKOV DETECTORS

3.1 Introduction

For cosmic rays with energy below 100 TeV, most of their secondaries do not have enough energy to reach the ground. Instead they are absorbed in the protective atmospheric layer surrounding our planet. Thus it is impossible to directly measure most of the EAS particles with ground-based detectors. Fortunately, information about the lateral and longitudinal development of each shower may still be obtained by studying the atmospheric Čerenkov emission due to the shower particles.

3.2 The Čerenkov Mechanism

Researchers in the early studies of radioactivity were the first to notice this radiation. A pale blue glow was often seen in transparent materials stored near radioactive sources. Ignored for many years, this phenomenon was first investigated seriously by Mallett (1926) and then in greater detail by Čerenkov (1934). A theoretical explanation, describing the mechanism responsible for this radiation, was proposed by Frank & Tamm (1937). The derivation of this explanation contains a degree of mathematical rigour beyond the scope of this thesis. However, it will still be useful for us to consider a simplified picture of the Čerenkov mechanism.

Let us imagine the passage of a charged particle through a non-conducting medium. The particle's electromagnetic field distorts the shape of the local molecules in the

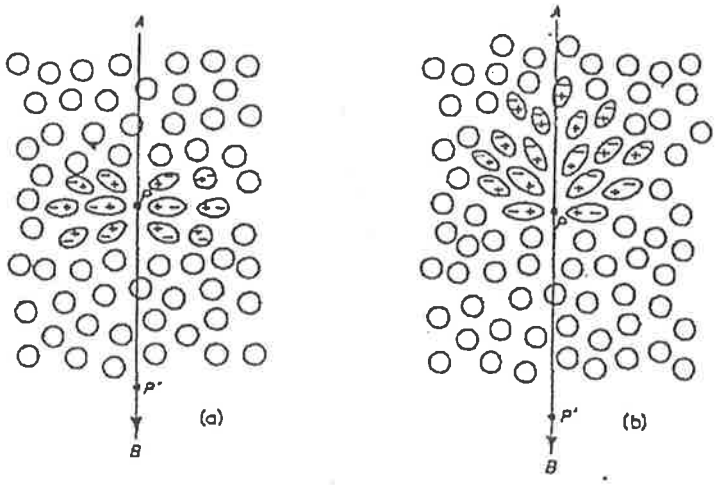

Figure 3.1: A fast charged particle travelling from A to B through an isotropic medium sets up a local time-dependent polarisation in the surrounding molecules (from Jelley 1982).

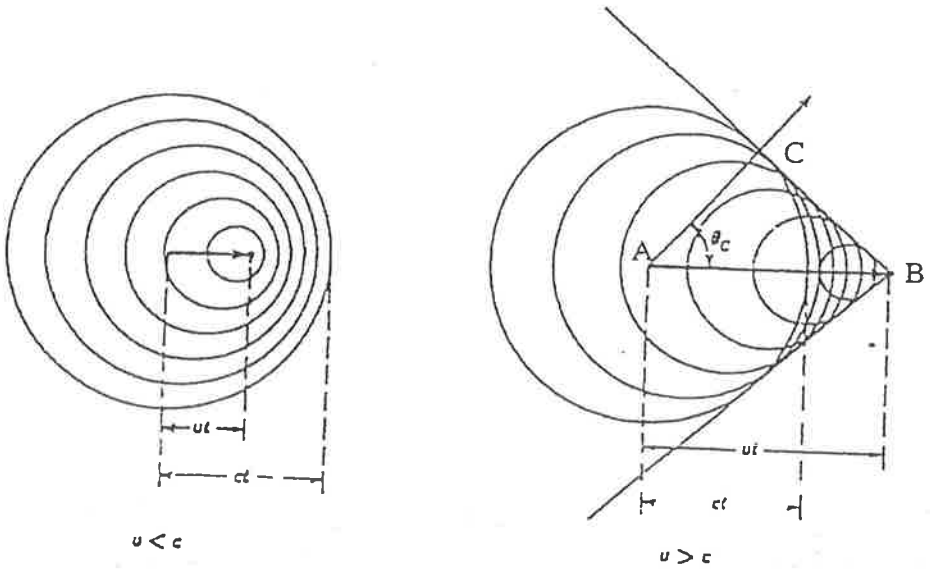

Figure 3.2: Huygens construction of a Čerenkov wavefront from the constructive interference of wavelets. This occurs when $v > c/n$ (from Jackson 1962).

medium and a polarisation of this medium results. As the particle continues on its journey, the distorted molecules return to their original shape. We can see from figure 3.1 that, for low particle velocities, the polarisation is symmetrical and no resultant field is visible at macroscopic distances. Increasing the particle velocity produces an asymmetry in the polarisation field. This becomes significant at higher velocities. In the wake of the particle, a momentary dipole then forms at each element of the particle track and a brief electromagnetic pulse is radiated from each point.

Generally the pulses from different track elements interfere destructively and no coherent emission is observable at macroscopic distances. However, suppose the particle velocity, v, exceeds the phase velocity of light, c/n, in this medium where c is the speed of light and n is the refractive index of the medium. The wavelets radiated from each element then add constructively to create a wavefront. This is shown in the Huygens' construction in figure 3.2. For coherence to occur we require the track length of the particle to be much larger than the wavelength of the emitted light and the particle velocity to remain nearly constant along this track.

The Čerenkov wavefront is an optical shock wave similar to bow waves produced by boats and the sonic boom of a jet aircraft breaking the sound barrier. It is directed at an angle, θ_c, to the particle track. By symmetry about the particle track, this angle forms a cone in three dimensions defining an expanding ring of light away from the central axis. In a time, t, the particle moves a distance, vt, through the medium and the wavefront will travel a corresponding distance, ct/n. Combining these, we derive the Čerenkov relation

$$\cos\ \theta_c = \frac{1}{\beta n} \tag{3.1}$$

where $\beta = v/c$. The angle of emission is completely defined from the particle velocity and the refractive index of the medium.

A number of interesting properties of the Čerenkov emission follow directly from this:

- There exists a minimum velocity

$$\beta_{\min} = \frac{1}{n} \tag{3.2}$$

  below which no emission of radiation can occur. At this velocity, $\theta_c = 0°$ and any radiation produced will be beamed along the particle track.

- The angle of emission increases with n. A maximum angle

$$\theta_{c\max} = \cos^{-1}\left(\frac{1}{n}\right) \tag{3.3}$$

  exists for particles in the ultra-relativistic limit, $\beta = 1$.

- Due to the dispersive nature of any real medium, there exist absorption bands in the frequency spectrum making n less than unity. Čerenkov emission is not possible at these frequencies (e.g. X-rays and γ-rays), and is restricted primarily to the visible and ultraviolet regions.

Following the work of Frank and Tamm, the amount of energy, E, lost to the surrounding medium for Čerenkov emission by a particle of charge, Z, is described by

$$\frac{d^2E}{dldf} = \frac{Z^2e^2 4\pi f}{c^2}\left(1 - \frac{1}{n^2\beta^2}\right) \tag{3.4}$$

where l is the track length and f is the frequency of emitted radiation. The energy lost by the particle is much smaller than the losses due to bremsstrahlung and ionisation losses. The energy is transferred to the medium, and it is the medium (not the particle) that emits the Čerenkov pulse.

For a singly charged particle such as a muon or electron, we can now predict the number of Čerenkov photons, N, radiated with wavelengths between λ_1 and λ_2 for a given track length using

$$N = 2\pi\alpha\, l\left(\frac{1}{\lambda_1} - \frac{1}{\lambda_2}\right)\left(1 - \frac{1}{\beta^2 n^2}\right) \tag{3.5}$$

where $\alpha = 1/137$ is the fine structure constant.

It is clear that the number of photons produced depends on λ^{-1}, and so the Čerenkov emission will peak near the ultraviolet end of the spectrum.

3.3 Čerenkov Emission in the Atmosphere

Early studies of the Čerenkov mechanism only considered emission from transparent solids and liquids. Due to their high refractive indexes, these media generate large numbers of photons and thus measurements of these signals were relatively simple.

Considering the passage of charged cosmic ray particles through the atmosphere, Blackett (1948) proposed that Čerenkov emission in a gas might produce a significant

signal distinguishable from the background light of the night sky. This was first observed by Galbraith & Jelley (1953) and later confirmed independently by them (1955) and Nesterova & Chudakov (1955).

As we mentioned in the previous section, there exists a minimum velocity, β_{min}, for a particle of rest mass, m_o, to induce Čerenkov emission. This corresponds to an energy threshold, E_{cmin}, defined by

$$E_{c\min} = \frac{m_0 c^2}{\sqrt{1-\frac{1}{n^2}}} \tag{3.6}$$

Assuming a simple isothermal atmosphere, the refractive index can be written as

$$n = 1 + \eta \tag{3.7}$$

where

$$\eta = 2.9\times10^{-4} \exp\left(-\frac{z}{z_o}\right) \tag{3.8}$$

is a function of height, z, and the scale height of the atmosphere is z_o = 8 km.

We can use this to directly calculate E_{cmin} at sea level for the main shower particles

Electrons: E_{cmin} = 21 MeV (3.9a)

Muons: E_{cmin} = 4.3 GeV (3.9b)

Protons: E_{cmin} = 39 GeV (3.9c)

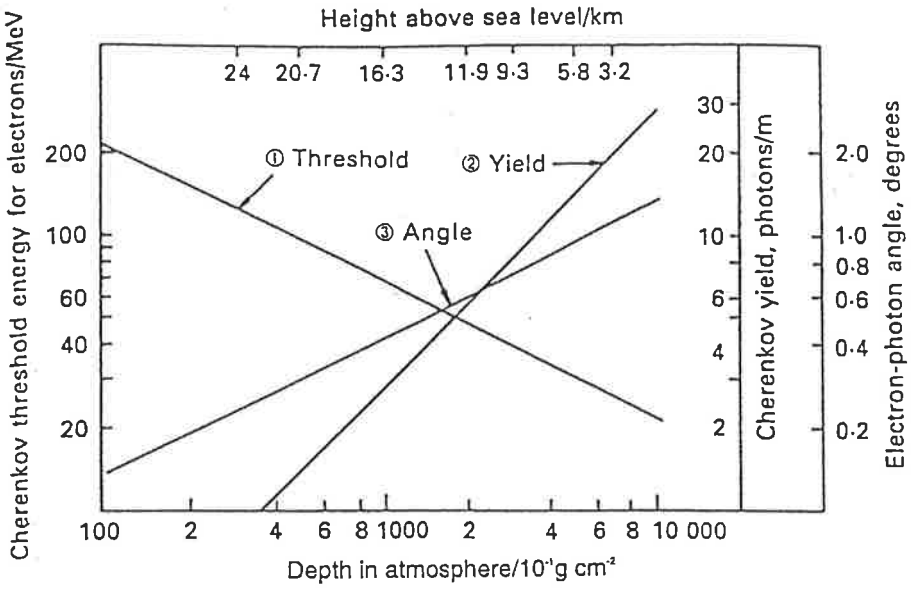

Figure 3.3: The variation with depth in the atmosphere of (1) the Čerenkov energy threshold; (2) the intensity of the Čerenkov pulse; and (3) the emission angle for the electrons in the shower (from Ramana Murthy & Wolfendale 1986).

The Čerenkov energy threshold, production angle and photon yield all scale with atmospheric depth as evident in figure 3.3. As a particle penetrates deeper into the atmosphere: its threshold energy decreases; the Čerenkov production angle increases; and the number of photons produced per unit track length increases. If we consider particle energies well above Čerenkov threshold, then the photon yield at sea level in the wavelength range 300 – 600 nm can be approximated from equation 3.5 as

$$\frac{dN}{dl} = 1530\ \eta \text{ photons cm}^{-1} \qquad (3.10)$$

In practical terms, this means that at sea level about 44 photons will be emitted for every metre of particle track. This is provided that the particle's energy remains well above the Čerenkov threshold. We can also derive a more useful relation for the emission angle in degrees from equation 3.1

$$\theta_c = 81\sqrt{\eta} \tag{3.11}$$

Therefore at all depths of emission, θ_c is small and the Čerenkov pulse will be emitted in a direction similar to that of the particle. Since these pulses are emitted from all parts of the shower's development, the total Čerenkov signal will contain information on the lateral and longitudinal development of the shower.

Čerenkov radiation suffers attenuation in the atmosphere through Rayleigh scattering, aerosol scattering and ozone absorption. These processes do not greatly affect the overall transmission within the spectral response of our detector. However, it is possible that selective transmission losses at different stages of shower development may complicate the interpretation of Čerenkov pulses at ground level. We shall leave a discussion of the modelling of these transmission losses until section 5.3.3.

3.4 Čerenkov Lateral Distribution

The variation in Čerenkov intensity with distance from the shower core defines the Čerenkov lateral distribution. Galbraith & Jelley (1953) made the first crude estimate of this. They observed light at distances greater than 100 m from the core. This extended pool of light defines a modest collecting area for a ground-based telescope even at energies where direct sampling of the shower front is impossible. Trigger rates

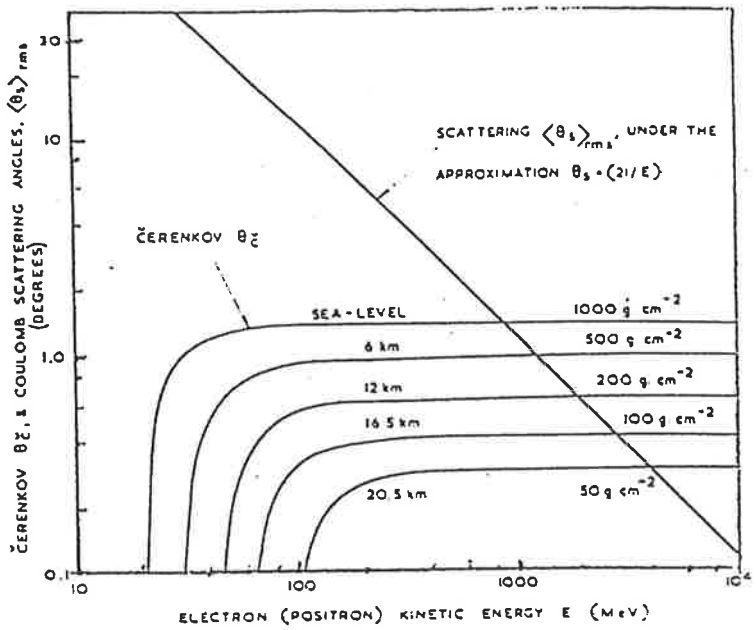

Figure 3.4: A comparison of the energy dependence of both the Čerenkov emission angle and the RMS deviation due to multiple coulomb scattering of the electrons (from Jelley 1967).

many times greater than that obtained from satellite experiments at the same energies are then possible.

In an extensive air shower, the majority of particles available for Čerenkov emission are electrons. It is no surprise then that the Čerenkov lateral distribution is dominated by the lateral spread of the electromagnetic component of the shower. The main cause of this lateral broadening is the multiple coulomb scattering of low energy electrons off of atmospheric molecules. The RMS angular deviation, θ_s, in radians due to scattering is related to the electron's energy, E, in MeV by

$$\partial \theta_s = \frac{E_s}{E}\sqrt{\partial x} \qquad (3.12)$$

(Rossi & Greisen 1941)

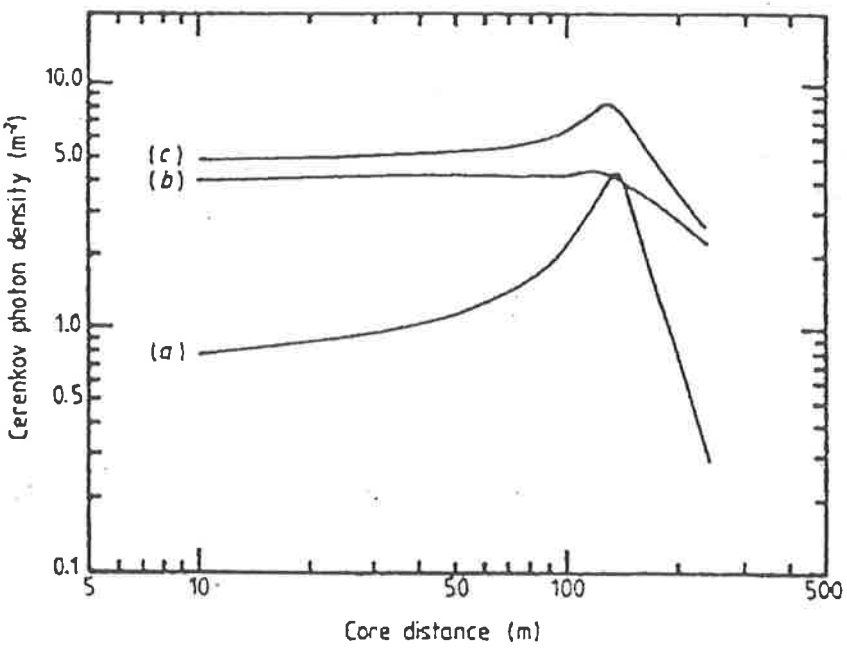

Figure 3.5: A breakdown of the Čerenkov lateral development for a 100 GeV γ-ray induced cascade into electron energy components (a) $\geq$ 1 GeV which defines the Čerenkov shoulder; (b) < 1 GeV which produces the majority of the Čerenkov signal; and (c) all energies (from Rao & Sinha 1988).

where E_s = 21 MeV and x is the path length in radiation lengths. We can see that after travelling a distance of one radiation length, a 100 MeV electron will be scattered by $\theta_s \sim 12°$ (this is much larger than the Čerenkov angle at sea level, which is $\theta_c \sim 1.3°$). The dependence of θ_c and θ_s on altitude and particle energy is shown in figure 3.4. It is evident that most shower electrons suffer multiple coulomb scattering during their entire journey through the atmosphere. Muons, on the other hand, are far more penetrating and do not suffer appreciable scattering, so the lateral extent of their Čerenkov emission depends on their production height and the transverse momenta of their meson parents.

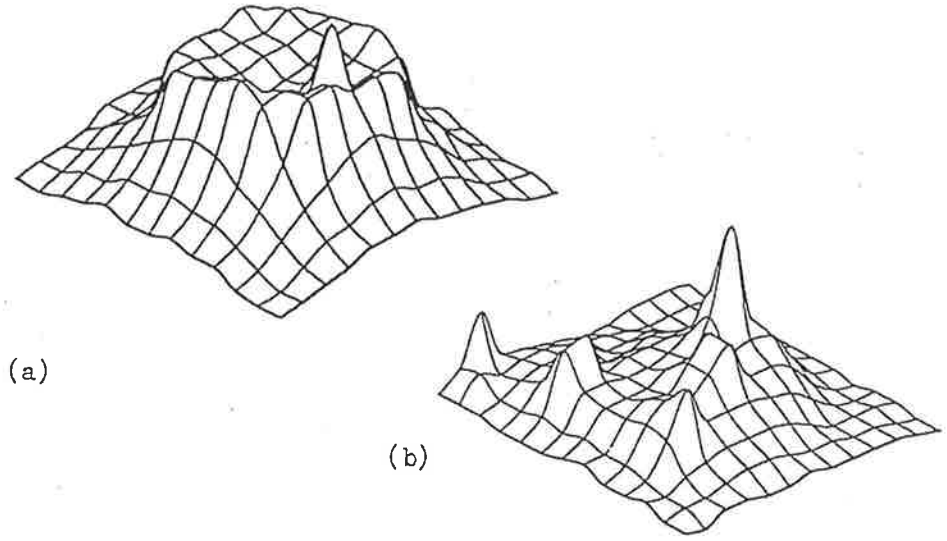

Figure 3.6: 3D contour plots of Čerenkov photon densities at sea level for vertical showers initiated by (a) 320 GeV γ-ray and (b) 1 TeV nucleon. A grid spacing of 50 m has been used. The Čerenkov shoulder is the dominant feature of (a) while (b) shows the presence of local muon peaks (from Hillas & Patterson 1987).

While we are mainly concerned with the development of showers due to hadronic primaries for the work in this thesis, it is useful to consider the characteristics of γ-ray initiated showers for a few reasons. The overall development is easier to study and reflects that of the low energy electromagnetic sub-showers in hadronic showers. Also, the design of atmospheric Čerenkov telescopes has been optimised to preferentially select γ-ray signals rather than the cosmic ray background.

For a vertical γ-ray primary, the pure electromagnetic cascade is responsible for the flatness of the Čerenkov lateral distribution observed out to about 150 m from the shower core. Beyond this, the intensity falls steeply as $1/r^2$ where r is the distance from the shower core. Between these two regions lies a phenomenon known as the

"Čerenkov shoulder". This enhanced ring of light, centred at the core, is caused by emission from relativistic electrons ($E > 1$ GeV) travelling close to the shower axis (see figure 3.5). θ_c increases with decreasing height such that the product of these two quantities remains constant for a large range of altitude (7 – 20 km). This results in emission from these heights focusing to a small core distance range on the ground approximately 150 m from the shower core (Rao & Sinha 1988). In a real shower, multiple coulomb scattering of these electrons will be significant and the shoulder will be somewhat blurred.

Higher energy γ-ray showers penetrate closer to the ground and the reduced distance between shower maximum and observation level causes a steepening of the lateral distribution near the core washing out the presence of the Čerenkov shoulder. At least for cosmic ray showers, the shoulder has been observed up to PeV energies (Dawson et al. 1989). Showers arriving from large zenith angles have a lateral distribution flatter near the core and broader overall due to the increased distance to shower maximum. This places the Čerenkov shoulder further from the core. A recent experimental verification of these features can be found in Aharonian et al. (1999). Cosmic ray showers have steeper lateral distributions than pure electromagnetic cascades and the shoulder is less noticeable. This is due to the penetrating hadronic core maintaining an appreciable number of Čerenkov inducing particles travelling close to it. The shower core may be detectable at ground level and Grindlay (1971) has suggested that it might be possible to distinguish between cosmic ray showers and γ-ray showers on the basis of its presence.

Fluctuations in intensity observed by a detector at any core distance may be due to Čerenkov emission from nearby penetrating muons. These local intensity peaks are superimposed on the lateral distribution as shown in figure 3.6 and offer another tool for the discrimination between hadronic and γ-ray primaries. Ozone absorption at high altitudes greatly reduces much of the ultraviolet Čerenkov signal from the overall shower. The use of an ultraviolet filter can enhance the more local ultraviolet signal emitted by nearby penetrating particles. However, this has been shown by Hillas & Patterson (1990) to offer little improvement in aiding γ-ray selection. In section 2.4, we discussed that heavy cosmic ray primaries are characterised by a broader lateral distribution of shower particles than that of the protons due to the enhanced muon content in their showers. The Čerenkov lateral distribution similarly reflects this.

3.5 Čerenkov Angular Distribution

The intensity of Čerenkov radiation as a function of angular distance from the shower axis depends strongly on the distance from the shower core. The analytical calculations of Zatsepin (1965) showed that for non-zero core distances, the observed maximum photon intensity does not coincide with the arrival direction of the shower. Figure 3.7 shows angular distributions from simulations of vertical γ-ray showers of energy 1 TeV and 5 PeV, and proton showers of 1.5 TeV and 4.5 PeV. Core distances of 0 m, 100 m and 400 m are considered.

Observations at the core measure the maximum emission from directly overhead. At increasing distances from the core the angle of peak emission is observed to increase. If we assume that most of the Čerenkov emission is produced at shower maximum it

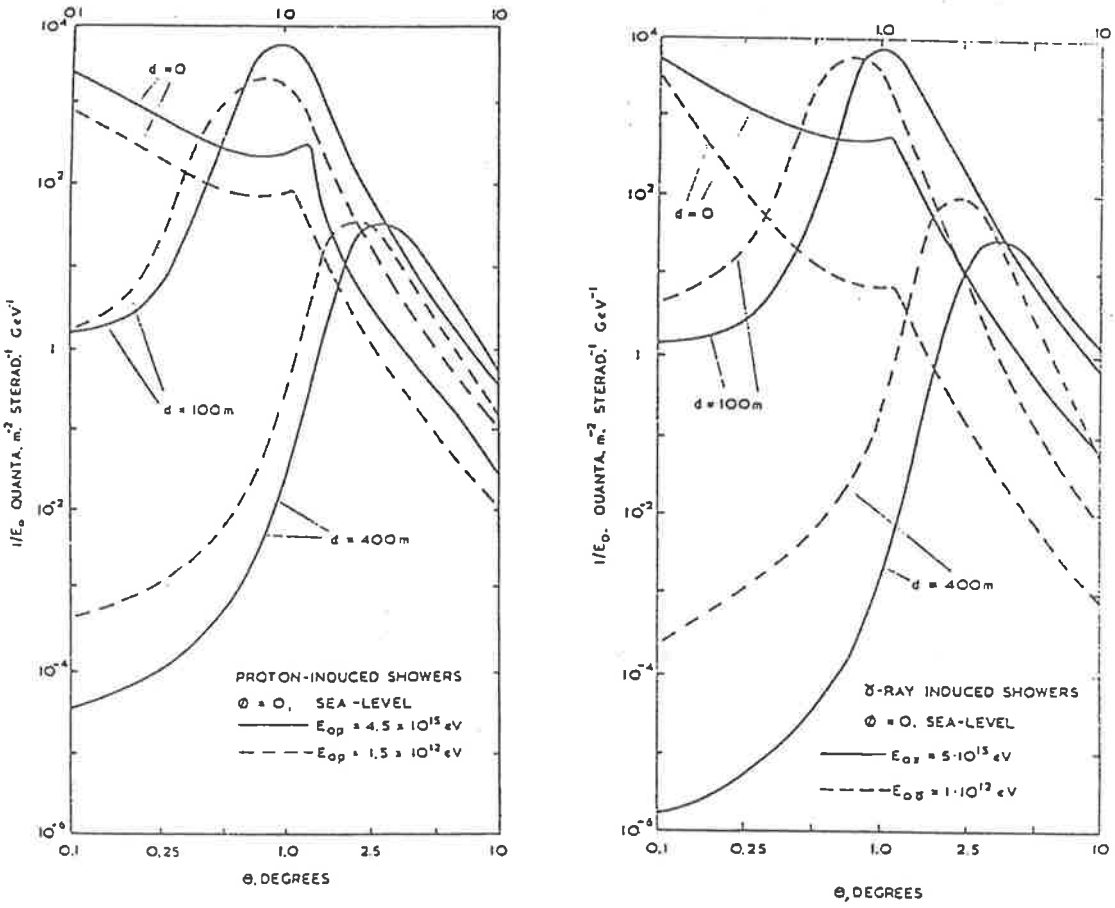

Figure 3.7: Theoretical angular distributions of Čerenkov photons for vertical γ-ray and proton showers at sea level based on calculations by Zatsepin (1965). The dependence of peak emission angle on core distance is shown (from Jelley 1967).

becomes easier to understand this effect. By a simple geometric argument, our line of sight to shower maximum defines an angle with the vertical shower axis that increases as we travel farther from the core (for a given primary energy). An increase in primary energy for a fixed core distance also increases the peak emission angle. This reflects the reduced distance from observation level to shower maximum for showers of higher energy.

The broad angular distribution complicates the collection of Čerenkov signals in two main ways:

- The field of view of the detector must be sufficiently large in order to collect enough of the extended angular Čerenkov image. If not, important information about the shower's development will be lost. Gamma ray selection based on the shape and orientation of the angular images collected in the focal plane of the detector is a powerful technique that has dominated the design of instrumentation in γ-ray astronomy in recent years.

- Any knowledge of the arrival direction of the primary particle is limited. Fortunately, the major axis of the angular image points towards the true arrival direction of the primary. This can be determined with imaging systems of sufficiently high angular resolution.

3.6 A Simple Atmospheric Čerenkov Telescope (ACT)

The detection of faint γ-ray signals has influenced the design of atmospheric Čerenkov telescopes. The steep energy spectrum for γ-ray signals, and their absorption in the

microwave background radiation at high energies, biases the collection of data to that of low energy events. The performance of an EAS detector system is characterised by an *energy threshold*. This is considered to be the minimum energy of a shower capable of triggering the system. A reduction in threshold will greatly increase the data collecting ability of a telescope and enable the detection of more distant objects.

The simplest ACT employs a single photomultiplier tube (PMT) at the focus of a large mirror. The field of view is chosen to maximally capture the γ-ray Čerenkov angular distribution. Light collected by the mirror is focused onto the PMT and converted into electrical pulses. Utilising fast electronics and gating this signal, the amount of background noise may be reduced. The γ-ray selection capability of an ACT depends on its ability to separate out two independent sources of noise: illumination of the PMT by the night sky background (NSB); and the large number of cosmic ray events generating Čerenkov pulses similar to that of the γ-rays. The work in this thesis is primarily a study of the cosmic ray background.

3.6.1 Reducing Sky Noise

Čerenkov signals are superimposed on the NSB fluctuations and contribute only 10^{-4} of the total background light. The mean charge collected by an ACT from the NSB flux, Φ_{NSB}, is described by

$$\overline{n_{pe}} = A\,\Omega\,R\,\varepsilon\tau\,\Phi_{\mathrm{NSB}} \tag{3.13}$$

and depends on the geometry of the detector. Namely: the mirror collecting area, A, in metres; its reflectivity, R; the solid angle subtended by the PMT, Ω, in steradians; the

quantum efficiency of the PMT photocathode, ε; and the integration time in which pulses were recorded, τ. The Čerenkov signal collected with the same detector is

$$S = \rho_c AR\ \varepsilon \tag{3.14}$$

where ρ_c is the Čerenkov photon density in photons m^{-2}. Since the NSB fluctuations are described by Poisson statistics, we can express the signal to noise ratio as

$$\frac{S}{\sqrt{n_{pe}}} = \rho_c \sqrt{\frac{AR\varepsilon}{\Omega \tau \Phi_{NSB}}} \tag{3.15}$$

We can see from this that Čerenkov signals may be enhanced purely through the optimisation of detector characteristics. An increase in mirror area, reflectivity, and PMT quantum efficiency will increase the collected signal. The Čerenkov angular distribution defines an optimal Ω (as seen in section 3.5). Anything larger than this will simply add to the level of noise.

At first glance, the task of detecting faint Čerenkov emissions in such an overwhelming noisy background seems a daunting one. It was recognised early on that Čerenkov detection might be possible by exploiting the short duration of such pulses. At timescales approaching the width of these pulses (typically of the order of 10 ns) the Čerenkov pulse is visible above the sky noise. By employing fast electronics and reducing τ accordingly, a great deal of the spurious noise outside this window will be rejected.

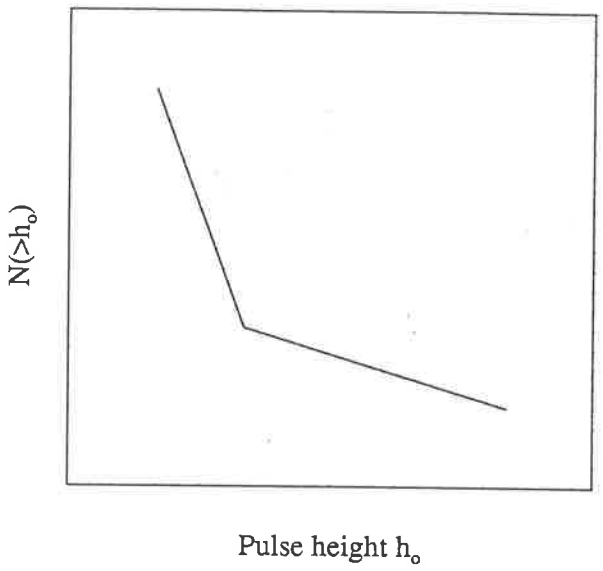

Figure 3.8: Integral pulse height distribution describing the frequency of pulses with pulse heights greater than h. The steep line represents the NSB background and the shallow line is due to atmospheric Čerenkov signals.

If we were to trigger the ACT randomly on the night sky, we would see that the number of NSB pulses collected by the PMT above a pulse height, h, is well described by a power law

$$n_{\mathrm{NSB}}(>h) = kh^{-\kappa} \tag{3.16}$$

where κ lies typically in the range 8 - 16 (Patterson & Hillas 1983) and k is a constant. This integral pulse height distribution is expressed in figure 3.8. Photons from the NSB follow Poisson statistics and the steeper line is due to the detector triggering on upward fluctuations in the sky noise. Above some pulse height, the slope of the line abruptly changes and the detector begins to trigger from atmospheric Čerenkov signals. The power law describing the Čerenkov signals is representative of the energy spectrum of the initiating primaries. Selection of the triggering criteria for an ACT involves a

compromise between the number of accidental noise triggers accepted and the lowering of the energy threshold for the detector.

Random fluctuations in the sky noise set the minimum operating energy of an ACT. The number of accidental triggers due to noise is reduced when operating a number of PMTs in coincidence. The trigger rate R_i from each ith PMT above some trigger threshold is used to define the rate of accidentals recorded for this threshold as

$$R_{acc} = n\tau^{n-1}\prod_{i}^{n} R_i \tag{3.17}$$

for n PMTs triggering in coincidence within a time, τ.

3.6.2 Defining Energy Threshold and Collection Area

The energy threshold of an ACT is often characterised by the lowest energy γ-ray primary capable of triggering the telescope. This is extremely difficult to estimate accurately from shower simulations. The uncertainty of such a measurement can be of the order of 50% due to difficulties in correctly calibrating the detector. Also, the interpretation of the energy threshold from simulations depends on the choice of hadronic interaction model used. Thus, there is the potential for great differences in the thresholds and flux rates reported by different experiments.

A more robust parameter to use is the effective energy threshold suggested by Weekes (1988). For an energy dependent γ-ray collecting area $A_\gamma(E)$ and source spectrum $N_\gamma(>E) = k_\gamma E^{-\alpha}$ we can define the energy, E_{eff}, which maximises the product $A_\gamma(E)E^{-\alpha}$. It is usually within a factor of 2 or 3 of the real energy threshold. Both

the effective energy threshold and the collecting area for the cosmic ray primaries studied in this thesis will be determined similarly from detailed Monte Carlo simulations of shower development described in chapter 5. The collecting area is determined by the lateral spread of Čerenkov light and will differ for each species of cosmic ray primary. Similarly, the energy threshold will vary for light and heavy hadronic primaries due to differences in their Čerenkov production efficiency.

The collecting area scales with energy and its edge is not clearly defined. Thus, it is often more useful to estimate an effective collecting area for a given mass primary. To do this, we must first determine the integral trigger efficiency of the telescope for each cosmic ray species from simulations. This is equivalent to the fraction of showers, above a given energy, capable of triggering the telescope. We will define the effective collecting area, for a given mass primary, by the product of its trigger efficiency and the area in which the showers have been distributed. Figure 3.9 shows the triggered energy spectra and the integral trigger efficiencies for vertical proton and iron showers with the BIGRAT telescope as described in chapter 5.

Observations at large zenith angles see an increased collecting area for energies well above threshold. This is because of the greater distance from observer to shower maximum. However, since the Čerenkov signal for a given primary energy is now spread over a larger area, the photon density will be greatly reduced. This results in a significant increase in threshold energy. The total trigger rate is commonly observed to follow a $\cos^n(\theta_z)$ relationship with zenith angle, θ_z, where n typically lies between 2 and 3 (Boley 1964).

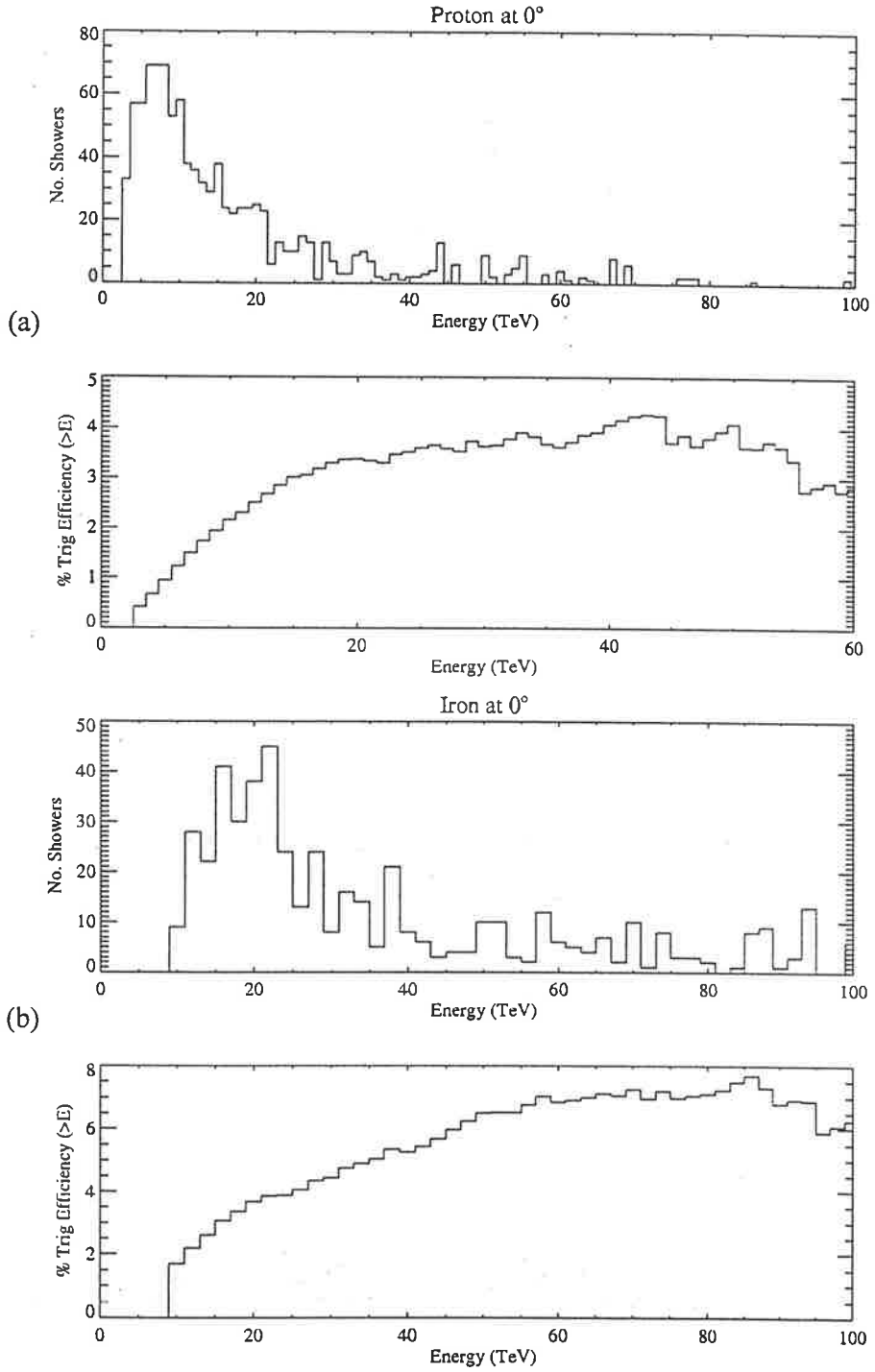

Figure 3.9: (a) Triggered energy spectrum for protons at the zenith estimated from simulations described in chapter 5. The effective energy threshold is equal to the modal energy of the distribution. The second plot shows the integral triggering efficiency as a function of energy.
(b) The same two plots for iron primaries at the zenith.

Chapter 4

THE PULSE SHAPE SYSTEM

4.1 Introduction

The time profile of the Čerenkov pulse has been studied since the earliest measurements of atmospheric Čerenkov from EAS (Boley 1962, Fomin & Khristiansen 1972). With the emission occurring over a large range of atmospheric depth, it seems reasonable to assume that the pulse shape might be related to the longitudinal development of the shower. The pulse width measured by wide aperture detectors at large core distances has been found to be a good measure of the average depth of shower maximum (Thornton & Clay 1979, Patterson & Hillas 1983b). This was used to estimate the elemental composition of cosmic ray primaries at PeV energies (Thornton & Clay 1981). The main benefit in using the Čerenkov signal to infer the position of shower maximum is that it is far less sensitive to fluctuations inherent in directly measuring the particles in the shower front at a single depth.

Pulse shape discrimination in γ-ray astronomy has also been investigated. Initial studies suggested little difference between the pulse shapes of photon and proton primaries based solely on the presence of structure in the pulse (Patterson & Hillas 1989). However, no studies of pulse width were made at this time. The technique was then neglected in favour of the rejection of hadrons on the basis of the shape and orientation of their angular Čerenkov images. This proved a much more powerful discrimination tool.

Interest in timing information was renewed again, following the detection of a significant γ-ray signal from the Crab Nebula (Tűmer et al. 1990) using pulse shape discrimination alone. Cosmic ray events were identified, based on the presence of "kinks" and long tails in the pulse, and rejected. Konopelko et al. (1990) extended on this method by using the entire shape of the pulse to build a database of ideal γ-ray events for comparison with real data.

These techniques were still of limited use in enhancing γ-ray signals, relative to the power of imaging methods. However, it was known that image cuts become less effective at low elevations. This is because the increased distance from observing level to shower maximum for these inclined showers reduces the angular size of the image. Roberts (1993) devised a discrimination technique valid at all zenith angles based on the rise-time (RT), full-width-at-half-maximum (FWHM), and fall-time (FT) parameters of the pulse shape. He found that near-vertical showers benefited from FWHM cuts, whereas rise-time cuts based on the leading edge of the pulse become increasingly more effective as the detector is inclined towards the horizon. One possible explanation for this behaviour at low elevations is that the increased distance to shower maximum allows the signal from penetrating muons in the shower to overtake and separate from the main Čerenkov front. The light due to these muons arrives early, and is thus seen on the leading edge of the pulse shape. Since this technique increases the available elevation range, it benefits from an increase in the number of observable sources available for a given location and a given night. Unfortunately, low elevation observations also introduce a dramatic increase in the energy threshold, as discussed in section 3.6.2.

As we discussed in section 1.6.2, studies of elemental composition become more uncertain as we approach the knee. An increase in both energy threshold and collecting area with zenith angle enables us to probe the primary cosmic ray background across a wider range of energy than would be possible at a single elevation. However, this will still be constrained by the practical considerations of a greatly reduced trigger rate at the lowest elevations.

4.2 The Woomera VHE Gamma Ray Telescope

The pulse shape experiment described in this chapter was mounted on the Very High Energy γ-ray telescope BIGRAT (BIcentennial Gamma RAy Telescope) situated about 13 km north of Woomera, Australia (31°6' S, 136°47' E, 160 m a.s.l). The telescope began operation in 1988, and has been subject to a number of upgrades in design up until its closure at the end of 1998. A view of the telescope can be seen in figure 4.1. The Japanese telescopes CANGAROO-I and CANGAROO-II lie ~ 100 m to the west and 100 m to the northwest respectively.

The initial construction of BIGRAT consisted of three multi-segmented mirrors (A, B, C), each measuring 4 m in diameter, fixed to a single alt-azimuth mount. Each mirror segment was itself a spherical mirror of 0.9 m diameter. At the focus of each composite mirror a detector pod housed a triangular array of three RCA 8575 photomultiplier tubes (see figure 4.2). Elevation and azimuth encoders in the telescope mount permitted remote, computer-controlled guidance of the telescope from a nearby hut.

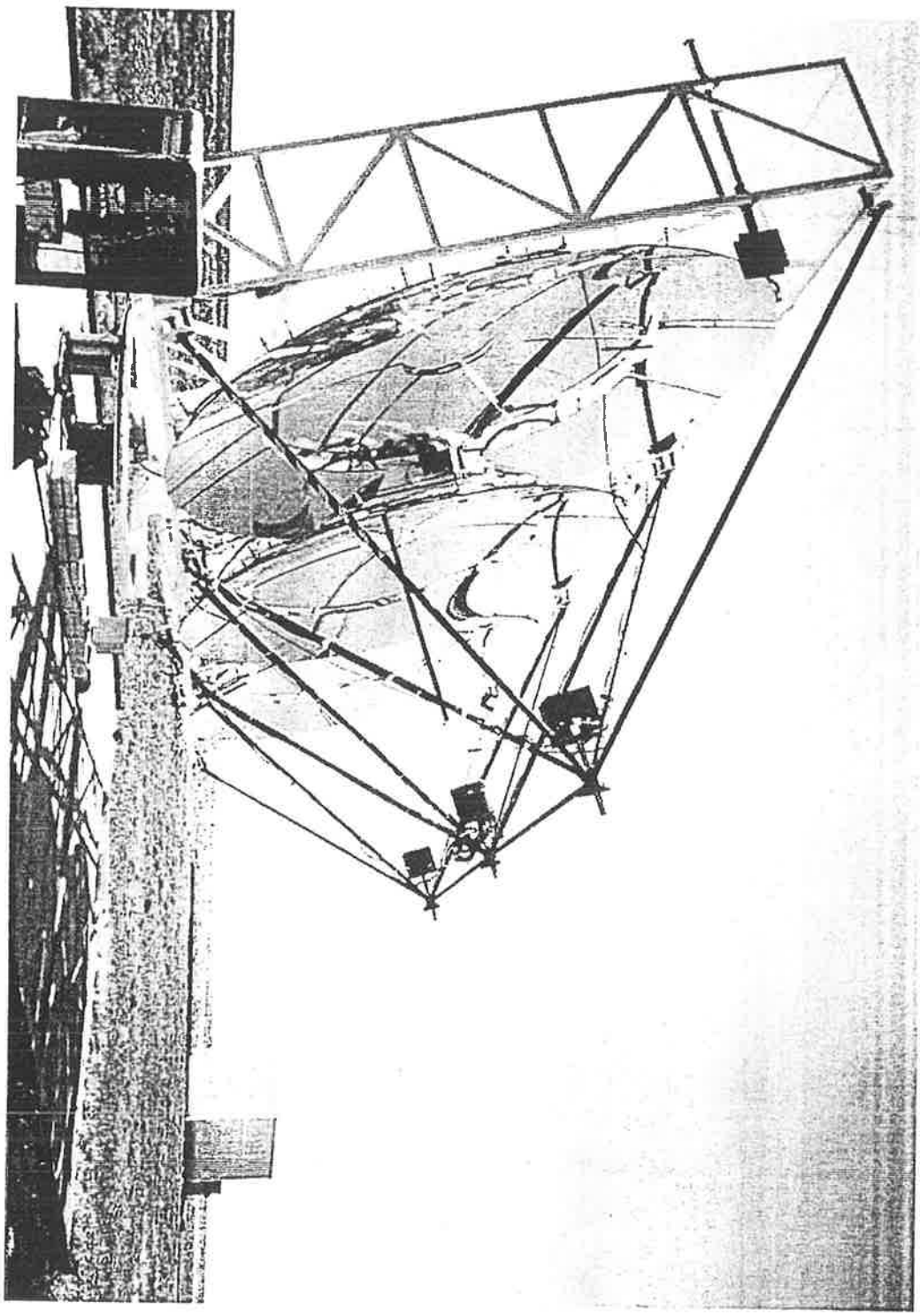

Figure 4.1: The BIGRAT Telescope at Woomera. Detector pods housing the Ax and Cx PMTs are mounted at the focus of each of the outer mirrors. The Japanese telescope, CANGAROO-I, lies 100 m to the east.

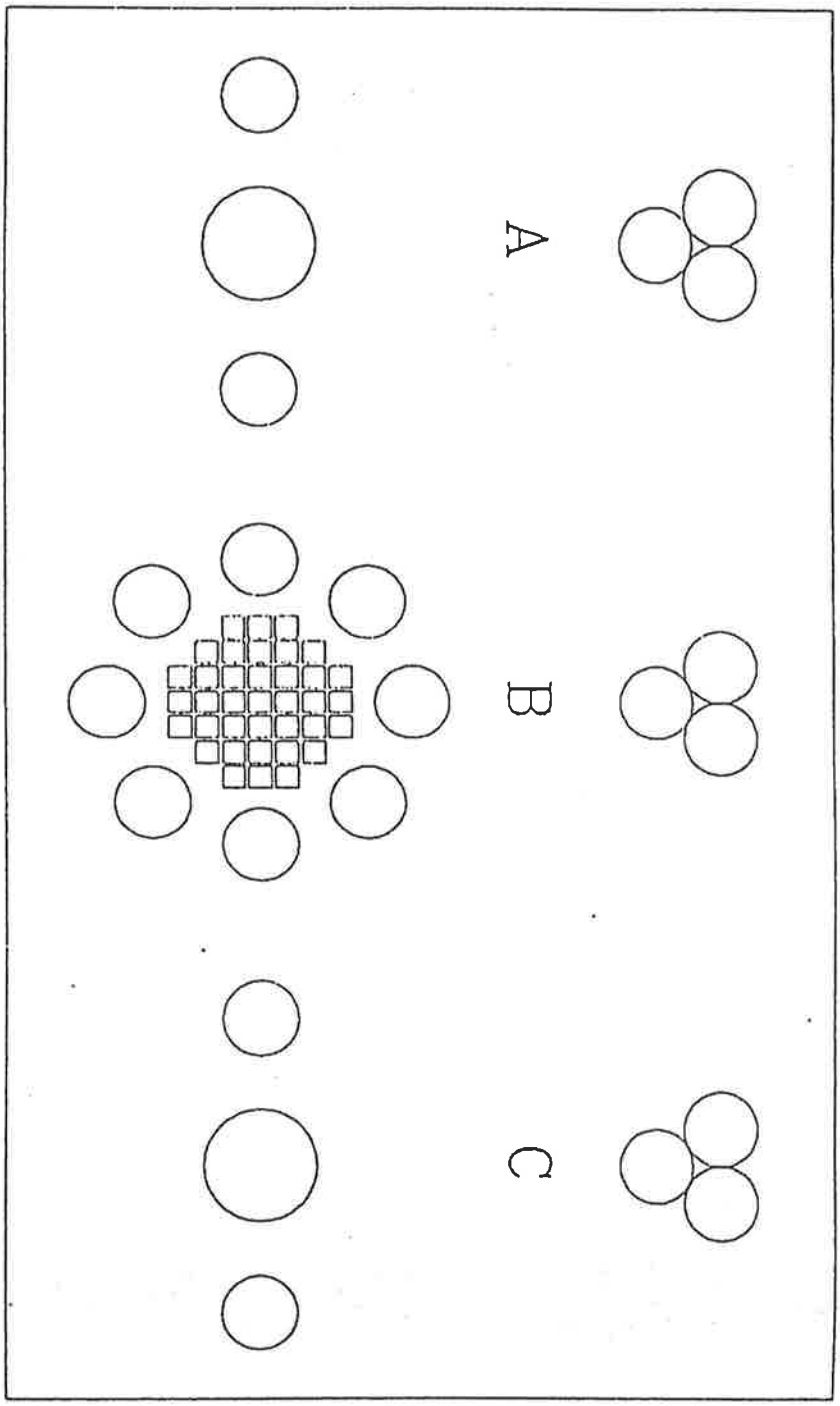

Figure 4.2: The previous configurations of detector arrangement on BIGRAT. The triplet detectors are depicted in the top diagram. Below this, Ax and Cx can be seen as the on-axis tubes on the outer mirrors, with the camera mounted on the central mirror (from Dazeley, 1999).

By 1992 the spherical mirrors were replaced with segmented parabolic mirrors maintaining the diameter of 4 m and introducing a focal length of 2.7 m. The parabolic shape removed any timing delays due to Čerenkov photons arriving at the focus from different parts of the mirror. It also increased the available collecting area for each mirror with improved focusing. Each segment of glass was coated with an aluminium oxide layer to reduce deterioration of the reflective surface over time.

Prior to the installation of the new pulse shape system, the BIGRAT mirrors had deteriorated somewhat mainly due to dust build-up. During the course of the experiment, measurements were made at various positions on each mirror segment using a calibrated reflectometer operating at 500 nm (Dowden et al. 1997). Combining these, the average reflectivities of the "A" and "C" mirrors were observed to remain fairly constant at about 65 ± 5%. We have assumed here that the reflectivity does not change rapidly across the spectral response of the photocathode.

At about the same time as the BIGRAT mirrors were replaced, a low resolution imaging system was installed on the central "B" mirror. The camera contained 37 Hamamatsu R2102 tubes and subtended a total field of view of ~ 2.3°. The detector pods on the outer "A" and "C" mirrors were also replaced with single on-axis tubes with fast rise-times for measuring pulse shape information. These will be discussed in more detail in the next section. Two monitor tubes of RCA 8575 were set off-axis to these. They were used in coincidence with a guard ring of Hamamatsu R329-02 tubes around the camera to identify off-axis cosmic ray events. This more recent configuration is shown in figure 4.2.

The original pulse shape system (Roberts et al. 1991) collected signals from one of the on-axis outer mirror tubes through a 10x pre-amplifier and along ~ 110 m of Heliax coaxial cable (with a bandwidth of 175 MHz) to a Tektronix 7912 digitising oscilloscope in the hut. The corresponding signal from the other tube was transmitted along RG58 coaxial cable to the hut as a trigger signal. Pulse shape analysis of observations of the binary pulsar Her X-1 resulted in a claim for a weak signal (Roberts 1993). The newer pulse shape system described in this chapter was installed in June 1995 and became operational later that year.

The current pulse shape system was originally operated on the telescope slab. This was necessitated by the attenuation of high frequency information in the Ax signal when travelling along large lengths of the coaxial cable. The initial setup used RG8 coaxial cable to transfer the PMT signals to the data acquisition system. In April of 1998, another similar length of Heliax cable was added in order to carry the Ax signal back to the hut. The new cabling layout enabled the remote collection of pulses in the relative comfort of the hut, and continual monitoring of data whilst collection was in progress. This made troubleshooting during observation runs much quicker. A comparison of the instrumental response of the detector for each cabling configuration will be discussed in section 5.3.1.

4.2.1 The Photomultiplier Tubes

For historical reasons, the on-axis tubes on mirrors "A" and "C" will be identified from here on as Ax and Cx respectively. The pulse shape analysis in this thesis was performed using the signals from Cx, a 10-stage EMI 7822 tube with a rise-time

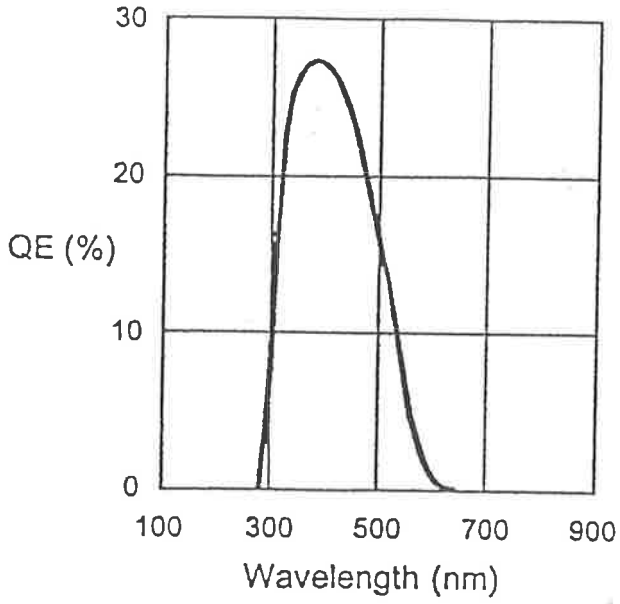

Figure 4.3: The spectral response of the bi-alkali photocathode used in the PMTs on BIGRAT. The peak emission occurs at about 400 nm.

of 1.9 ns. The other tube Ax is slightly slower (12-stage EMI 7823) at 2.1 ns and is mainly used to define the double coincidence trigger with Cx. Its pulse shapes have also been recorded for potential analysis. Each tube has an effective diameter of 75 mm and a field of view of 1.6°. Both use bi-alkali photocathodes with a peak quantum efficiency of 25% at 400 nm (see figure 4.3). These are mostly sensitive to incoming light with wavelengths between 300 nm and 600 nm. As such, we are not particularly sensitive to Čerenkov emitted in the ultraviolet.

Each photomultiplier base had already been tuned to provide a clean leading edge for the pulse shapes (Roberts 1993). The trailing edge fluctuates greatly and is extremely difficult to optimise for, because of large fluctuations in the signal in the last stage of the PMT dynode chain. No attempt has been made here to study the trailing edge in detail.

In the old pulse shape system the tubes were operated at much higher voltages due to the low gain of the digitising system. This resulted in some deterioration of the photocathodes of the tubes. The new digitising system has a higher gain allowing us to operate the tubes at reduced voltages. This minimised further damage to each photocathode through overexposure to background starlight, while still providing sufficient amplification for the faint Čerenkov signals.

4.2.2 Data Acquisition and Storage

Signals from Ax and Cx were read into the two channels of a Lecroy 9361 digital oscilloscope. This has a large bandwidth (300 MHz) for resolving the high frequency components of these fast pulses. The signals were terminated in 50 ohms and displayed as voltage-time profiles with a timebase of 5 ns cm^{-1} and a voltage gain of 5 mV cm^{-1}. The pulses were digitised in time steps of 0.4 ns and voltage steps of 0.16 mV.

A pulse height hardware threshold was applied to the Cx signal alone to trigger the system. Near the horizon, the event rate dropped considerably and a coincidence trigger was then applied to both channels to reduce the triggers due to local muons passing through the detector. A software coincidence trigger was later applied to each dataset. This allowed some flexibility in choosing the most efficient thresholds for minimising the effects of sky noise while maintaining a sufficiently high event rate.

For each hardware trigger, the digitised signals were recorded for later analysis. Initially, data were stored directly onto SRAM (Static RAM) cards mounted in the oscilloscope. This reduced the necessary delay between triggers due to the recording of each event. However, limitations in the oscilloscope's software prevented the

assignment of more than 1000 filenames and the continuous writing of multiple events to a single file was not possible. The data acquisition system was then altered to accommodate the remote transfer of data to a personal computer via a high speed, digital GPIB interface. This arrangement allowed more control over the storage of data but resulted in a dead time of ~ 100 ms per event during which time no further events could be captured. Although large, this delay was still modest compared with the typical trigger rates of less than 1 Hz at the zenith. Pulse data were stored in binary format together with event times read from the system clock of the computer. At the end of each observing session, data were backed up onto 100 MB Zip disks and transported back to Adelaide.

4.2.3 Operation of the Telescope

At the beginning of each observing season (of about a week), checks were performed on reference stars to maintain the pointing accuracy of the telescope and the system clock on the computer was updated. The sky was monitored each night for the presence of clouds by visual inspection. The weather conditions were logged together with details of the triggering setup at the start of each observation run.

Geomagnetic effects were investigated briefly during the initial phase of this experiment. The inclination or "dip" of the geomagnetic field at Woomera is -63°. The total field strength at this location is 58 μT, and the geomagnetic declination angle is 6°E. The mean event rate measured by the pulse shape system on BIGRAT as a function of geomagnetic azimuth is shown in figure 4.4. Data were collected at a fixed zenith angle of 60° and for azimuth angles of 0°, 90° and 180°. These rates were

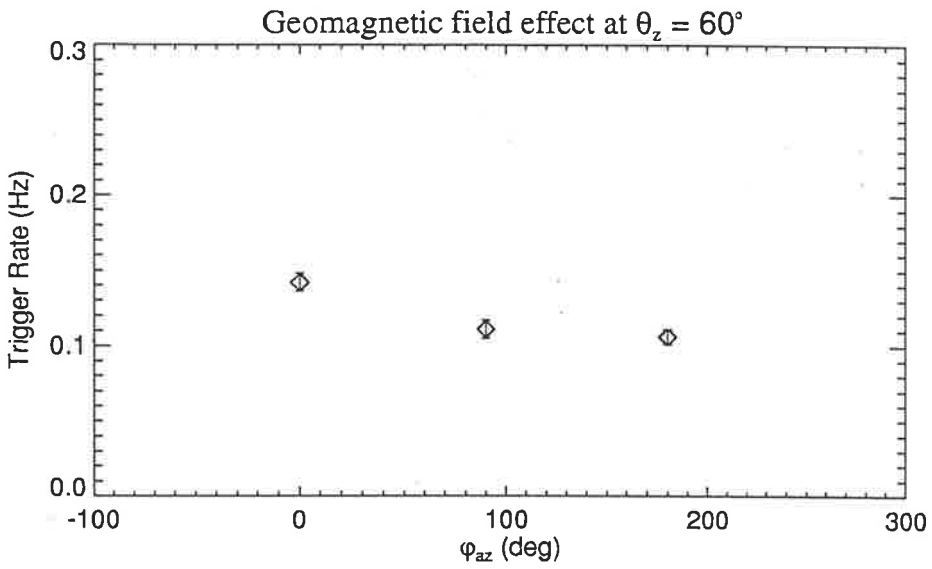

Figure 4.4: BIGRAT trigger rate measured at $\theta_z = 60°$ for a series of datasets collected at geomagnetic azimuth angles 0°, 90°, 180°. The observed rate decreases as the telescope moves away from the direction of geomagnetic north.

averaged over two clear nights of observations to help reduce any potential differences in atmospheric clarity arising between datasets. The event rate appears to be greatest for showers parallel to the field, decreasing for showers travelling across the field lines. This is consistent with the predictions outlined in section 2.5. However, no variation in the mean width of measured Čerenkov pulse shapes as a function of azimuth angle was observed.

During typical observation runs, pulse data were recorded in fixed zenith angle runs. To minimise any potential effect on the data at large zenith angles due to the geomagnetic field, the telescope was generally pointed northwards. Since the pointing direction for a given run was fixed, the star field seen by each tube (and thus the noise level) varied throughout the run. To monitor this, sky noise pulses were collected

prior to and after each run by randomly triggering the telescope on the same region of the night sky. Runs were kept short (~ 1 hour) to reduce the variation in noise level during this time. These short runs were also important for reducing the effects of atmospheric instability on the transmission of the Čerenkov pulses. This is particularly important at larger zenith angles where large atmospheric fluctuations in the increased air mass can alter the shape of the Čerenkov pulse. Towards the end of the experiment, the use of a narrow aperture, temperature sensitive cloud monitor (Clay et al. 1998) was investigated for these large zenith angle observations. Unfortunately the monitor was found to be less useful near the horizon, at zenith angles greater than 60°, due to radiant heat from the ground (Johnston 1998).

4.2.4 Pre-Analysis of the Pulse Data

To yield high current gains in the PMTs for the faint collected light, the tubes were operated at high voltages (~ 1500 V). Since their photocathodes were not shielded, a positive voltage was necessary to maintain a low voltage at the front of each PMT. This resulted in the output signals superimposed on a large DC signal at the anode. Prior to measurement by the oscilloscope, this DC offset must be removed by capacitative coupling of the PMT output. Unfortunately, the loss of the total DC component of the signal prevented the determination of the true zero brightness level (or at least with respect to the level of dark current in the PMTs).

The AC baseline is determined by averaging signal fluctuations such that the amount of signal in the measured pulse above and below the baseline is equivalent. The Čerenkov signal causes little shift in this baseline position since it is much faster than the coupling

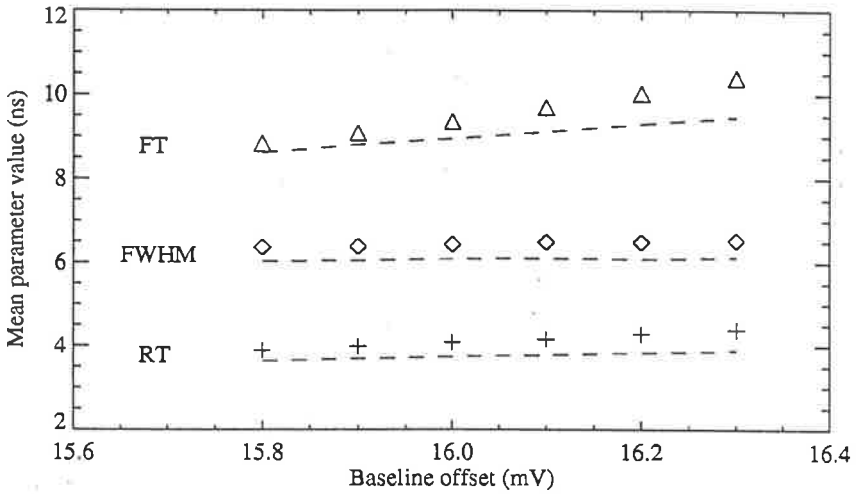

Figure 4.5: Sensitivity of pulse parameters to variations in the level of the voltage offset applied to the pulse data. A low trigger threshold of 7 mV has been applied for the plotted points. The dashed line describes the situation for a higher threshold of 14 mV. Even with the higher threshold, RT and FT are still affected by small baseline shifts.

response (~ 500 ns) of the system. Instead, the AC baseline is set by fluctuations in the NSB at timescales greater than this. Estimating the true zero of our atmospheric signals is difficult. Since the NSB fluctuations follow Poisson statistics it should presumably be possible to estimate the true, mean brightness level from fluctuations in the baseline. However, only a small portion of the noisy baseline was recorded at the start of each pulse. So we shall opt to reference our measured and simulated pulses from an AC baseline.

A positive voltage offset was applied to the baseline of the negatively going pulses captured by the oscilloscope. This was used to maximise the range of pulse heights for which temporal parameters could be reliably assigned. A maximum useful pulse height of 34 mV resulted in about 20% of the data lost through large off-scale pulses saturating

the system, while small pulses near threshold still contained sufficient resolution. The value of this offset was not always reliably recorded during an observation run. Also, if any change to the offset position occurred during a run while optimising the pulse height range, then direct subtraction of this offset was impossible. It was discovered that the assigned pulse parameters are sensitive to small shifts in the value of this offset (see figure 4.5). Variations in the parameter values occur roughly at the level of the mass discrimination of our modelling (see chapter 5) with the rise-time and fall-time parameters the most affected.

To combat this, an averaged baseline was estimated by fitting a Gaussian distribution to the first 10 ns of the noisy, leading edge of each pulse. Trigger delays larger than this had been applied when the data were recorded to minimise edge effects in the digitisation window. Thus, we have some confidence that this portion of the pulse contained only sky noise information. The effect of using an averaged baseline instead of the offset baseline was checked for a zenith dataset in which the offset was reliably recorded. Better agreement in the mean FWHM value was obtained between measured and modelled data (at least at the zenith) when considering the averaged baseline.

Since hardware triggers were set with respect to the offset baseline, new software thresholds had to be applied during pre-analysis at higher levels. The pulse parameters for small events are very sensitive to blurring by the presence of sky noise fluctuations (see section 5.3.4) and so these new thresholds have not eliminated any useful data. Only a small threshold level was applied to the Ax signals in order to increase the number of high-threshold Cx pulses collected, while still maintaining a coincidence trigger above the level of NSB fluctuations. The optimal trigger levels chosen for the

data will be quoted in section 5.3.2, following calibration of the detector and a consideration of sky noise effects on the data.

Prior to analysis, the event rate of each data set was binned into time intervals in order to reject portions of the data where the rates dropped below that consistent with Poisson fluctuations. This reduction in rate was expected to be due to thin, low level cloud that was not visible at the time of observations. Any presence of cloud may affect the pulse temporal information in a non-trivial way. At the very least, it suggests an increase in energy threshold due to the severely attenuated signals. After these rate cuts, data were selected based on the integrity of their pulse shapes. Events where part of the pulse fell outside the digitising window, such that parameter values could not be estimated, were rejected. The pulse data points were binned into 0.1 ns steps using a simple linear interpolation. Each pulse was then parameterised into rise-time (10 – 90% of the leading edge), FWHM (50 – 50% of pulse maximum), and fall-time (90 – 10% of the trailing edge) distributions ready for comparison with the parameter distributions from simulated data.

4.3 Calibrating the System

Čerenkov events are recorded as electrical signals. However, the simulations used in the next chapter do not attempt to model the gain structure of each tube. Instead, they generate pulses in units of photocathode charge, following the inclusion of mirror reflectivity and photocathode spectral response. To interpret the BIGRAT data with these simulations, a relationship between pulse height (in mV) and photocathode charge, Q, (in pe) must be established. The triggering criteria for the pulse shape

PMT	*Anode Current* (μA)	*Current Gain,* G (x10^5)	T_{RT} (ns)	Δ (pe mV^{-1})
Ax	6.2	5.0	2.7	7 ± 2
Cx	7.1	6.0	2.4	5 ± 1

Table 4.1: Mean values for measured anode current, current gain and conversion factors for each tube. The resolving times for each signal path are also displayed.

system are pulse height based and the pulse height will depend on the temporal characteristics of the final pulse. There will not be a simple relationship between Q and pulse height, except where the pulse is bandwidth limited. It is advantageous for us, when defining trigger thresholds for the simulations, to define the conversion factor in terms of the maximum pulse height, PH_{max}, rather than the area of the pulse. The following sections outline various methods for calculating the conversion factor

$$\Delta = \frac{Q}{PH_{max}} \tag{4.1}$$

4.3.1 Measuring Tube Gains

Direct measurements of the tube gains have been made in laboratory conditions in Adelaide. We define the current gain, G, of a tube as the ratio of anode current to photocathode current. The lighting conditions due to the night sky background were recreated in the laboratory using a green LED and a DC voltage supply. Since singles rates for each tube could not be monitored during observation runs, the level of illumination could only be estimated from the fluctuation level of the output signal on the oscilloscope. This was compared with signals directly sampled from the night sky.

The intensity of light from the night sky seen by each tube varies considerably due to the presence of stars in the field of view. The gain of each tube was therefore measured across a suitable range of lighting level, but only mean values will be quoted here.

The photocathode current in each PMT was measured with an electrometer sensitive to pA and a multimeter measured the anode current. The calculated gain was then used to describe the amount of current leaving the anode for any given charge, Q, leaving the photocathode. After the signal is terminated in Z = 50 Ω, the resulting pulse height measured on the oscilloscope will define the conversion factor for each tube

$$\Delta = \frac{T_{RT}}{1.6 \times 10^{-22} GZ} \quad \text{pe mV}^{-1} \tag{4.2}$$

The resolving time T_{RT} depends on the bandwidth of each signal path of tube, cabling and oscilloscope. Within this time, complete photoelectron pileup occurs and the maximum height of this pulse will then be in proportion with the charge leaving the photocathode. Values for the mean anode current, gain and conversion factor for each signal path are listed in table 4.1. No signal loss along the cabling has been considered here and so the conversion factors may actually be lower than quoted above.

Measurements of the Cx tube indicate some variation in gain with increasing light level. This may be due to photocathode damage as suggested in section 4.2.1. The pulse height distribution of the more stable Ax tube has been compared with that of Cx for each observation dataset to monitor its performance (see section 5.3.2).

In general, photomultiplier tubes also experience a certain degree of variation in their current gain with time when a voltage is first applied. Without a stable gain, calibration of this experiment is impossible and any data collected cannot be usefully analysed. Thus at the beginning of each observation run, tubes were operated for about half an hour in complete darkness to 'warm up'. This allowed enough time for the tube gain to become constant before any data was taken. The time chosen was compatible with observations of gain variation in the lab.

4.3.2 Sky Noise Fluctuations

Any measurement of faint Čerenkov pulses is sensitive to background illumination. Atmospheric Čerenkov telescopes are therefore ideally operated on clear moonless nights. Other sources of sky noise include direct and scattered starlight, zodiacal light, airglow, and light pollution from the nearby townships of Woomera and Roxby Downs. This sky noise limits the energy threshold for a Čerenkov telescope. No small signal can be distinguished from the noise. Telescopes with imaging systems installed are capable of detecting relatively low energy showers through the use of an array of pixels. Each of these sees a small window of the sky resulting in less illumination for a given pixel. Noise pixels that are clearly not part of the Čerenkov image may then be ignored. This provides a better signal-to-noise ratio than would be possible from a single pixel with the same field of view.

Modelling sky noise is not a simple task. The light arriving at a detector is a complex function of atmospheric transmission, the highly varying background star field, and fluctuations in the output signals of each tube. However, it is possible, for the purposes

of calibrating the system, to make an estimate of the background sky noise arriving at the detector as a function of galactic latitude. We begin by calculating the incident flux of a 10th magnitude star per square degree at 400 nm

$$F_{10} = 2.9\times10^{-2} \text{ photons ns}^{-1} \text{ m}^{-2} \text{ sr}^{-1} \text{ nm}^{-1} \tag{4.3}$$

This corresponds to the wavelength of peak emission for the photocathode (see figure 4.3). Including mirror area, A, mirror reflectivity, R, the detector solid angle, Ω, and integrating over the spectral response, $\Psi(\lambda)$, of the photocathode with respect to wavelength, λ, we calculate a mean sky noise rate for this star by rewriting equation 3.13 as

$$n_{mean} = A\Omega R \int \Psi(\lambda) F_{10}(\lambda)\, d\lambda \tag{4.4}$$

where n_{mean} is the mean fluctuation level of photocathode current in pe ns^{-1} due to light from a 10th magnitude star. A calculation of sky noise rates for the normal operation of BIGRAT depends on the number of 10th magnitude stars observed in our field of view as a function of galactic latitude. Following Allen (1973), we include the contributions from airglow, diffuse galactic light, and direct starlight where all are given in units of F_{10}.

Thus, we can calculate limits for the sky noise visible at the galactic pole and the galactic equator.

$$n_{pole} = 58 n_{mean} \text{ (galactic pole)} \tag{4.5a}$$

$$n_{equator} = 220 n_{mean} \text{ (galactic equator)} \tag{4.5b}$$

PMT	n_{pole} (pe ns^{-1})	$n_{equator}$ (pe ns^{-1})	$< \bar{n}_{measured} >$ (mV ns^{-1})	Δ (pe mV^{-1})
Ax	0.45	1.70	0.19	6 ± 3
Cx	0.45	1.70	0.17	6 ± 4

Table 4.2: Calculated limits for sky noise rates defined by n_{pole} and $n_{equator}$, the flux levels in pe ns^{-1} expected from viewing near the galactic pole and galactic equator respectively. The measured mean sky noise rate is quoted for each PMT in units of mV ns^{-1}. A conversion factor for each tube is also calculated and errors are estimated from the sky noise limits described above.

where n_{pole} and $n_{equator}$ describe the mean fluctuation level of photocathode charge in pe ns^{-1} due to the number of stars in our detector's field of view when looking at the galactic pole and the galactic equator respectively.

Table 4.2 lists the calculated sky noise limits defined by n_{pole} and $n_{equator}$. Since the viewing aperture of the PMTs is so small there will be considerable variation in the sky noise level for even a small number of stars in the field of view. Rather than attempt to match rates at the pole and equator, we will simply use the range of sky noise rates measured by BIGRAT to define a mean sky noise rate $< \bar{n}_{measured} >$ for each tube. We estimate the mean fluctuation level by fitting a Gaussian distribution to the fluctuations in each 50 ns sky noise pulse. Assuming these follow Poisson statistics, the standard deviation, $\sigma_{measured}$, then defines the mean fluctuation level in a single pulse by

$$\sigma^2_{measured} = \bar{n}_{measured} \quad \text{mV ns}^{-1} \tag{4.6}$$

We proceed to estimate the noise level for each sky noise pulse and average over the entire dataset to find the mean sky noise rate $< \bar{n}_{measured} >$. This is compared with

PMT	*Calculated Čerenkov signal* (pe)	*Measured Mean Čerenkov PH* (mV)	Δ (pe mV^{-1})
Ax	21 ± 2	5.2	4.0 ± 0.4
Cx	21 ± 2	5.8	3.6 ± 0.3

Table 4.3: Calculated and measured pulse heights of Čerenkov signals due to muons traversing the glass faceplate of each tube. A conversion factor is included for each PMT.

the mean calculated rate to define a conversion factor. The errors are assigned by considering the measured rate with respect to the calculated sky noise limits. While the errors are large, the calibrated sky noise does agree with the conversion factors estimated in the previous section and so falls well within the quoted sky noise limits. The calculated rates assume the output signal fluctuations of the tubes follow Poisson statistics. It must be mentioned that this is not entirely true since PMT signal fluctuations are described by behaviour between Poissonian and exponential (Rowell 1995).

4.3.3 Čerenkov Signals From Local Muons

Even when a tube is completely immersed in darkness, local penetrating muons from air showers may pass through the tube's glass faceplate and initiate Čerenkov production (Gregory et al. 1987). The track length of glass is smaller than 1 cm and the time for a muon to traverse it is less than 0.02 ns. The pulses are therefore orders of magnitude faster than the response of the system. Complete photoelectron pileup results and the only broadening of the output voltage pulse will be due to the limited bandwidth of the system. These muon pulses can thus be used to model both the response of the system

to each photoelectron and any instrumental fluctuations present. This will be essential for the accurate physical modelling of our detector in the next chapter.

We have already seen that the Čerenkov mechanism is well described by equation 3.1. If we include the track length of glass $L = 3.75 \pm 0.25$ mm and the spectral response of the tube, then it is a straightforward exercise to calculate the average charge released from the photocathode for a given Čerenkov pulse. With the PMTs covered, muon generated signals have been recorded by the pulse shape system. The mean pulse height of these measured signals is compared with the calculated charge in table 4.3 in order to define a conversion factor for each tube. These results appear to be in agreement with the previous calibration methods.

Chapter 5

COMPUTER SIMULATIONS

5.1 Introduction

Any mass composition analysis of data collected by an atmospheric Čerenkov detector requires knowledge of the response of the detector to different mass cosmic ray events. Only limited information of the primary mass and energy is preserved in the pulse shape data as a result of sampling the Čerenkov shower front at a single location for each event with respect to the shower core. Interpretation of the data must therefore be determined after the study of appropriate simulations of cosmic ray EAS.

In this chapter we look at the performance of our detector in the context of these EAS simulations. To recreate the physical conditions under which data were collected, measurements of both instrumental response and sky noise are incorporated into the modelled Čerenkov pulse shapes. We particularly concentrate on the handling of systematic uncertainties introduced at the time of data acquisition, and also those imposed by limits in the modelling. An interpretation of pulse shape structure follows identifying the optimal parameters for analysis. We begin with a description of the software used for the EAS simulations and its implementation.

5.2 Simulating Čerenkov Pulse Data

Monte Carlo calculations of Čerenkov pulses from EAS were made using the CORSIKA (Heck et al. 1998) program (version 5.94). This was written originally for

the KASCADE experiment (described in section 1.6.2). The software provides a detailed model of EAS initiated by high energy cosmic rays. Cosmic ray primaries are injected at the top of the atmosphere and the subsequent interactions and secondary particles are followed through the model atmosphere. Information from specific aspects of the shower may then be output for further analysis. The advantage of this program is its versatility. It can be set up to run on many computing platforms and customised for the study of a variety of different EAS experiments.

For primary energies covered in this thesis (1 TeV – 1 PeV), the differences in interaction models were not expected to be large. Hadronic interactions with atmospheric nuclei, at energies above 80 GeV, were calculated using VENUS (Very Energetic NUclear Scattering) (Werner 1993), which is a program designed to simulate ultra-relativistic heavy ion collisions. The widely used GHEISHA (Gamma Hadron Electron Interaction SHower Code) (Fesefeldt 1985) model has been used to calculate the elastic and inelastic hadron cross-sections for low energy (< 80 GeV) interactions. All electromagnetic interactions were simulated using the EGS4 (Nelson et al. 1985) routines.

In addition to the direct particle treatment, routines have been provided by the HEGRA group (Bernlohr 2000) for tracking the Čerenkov radiation produced in EAS. Bunches of Čerenkov photons are generated at each emission step of the charged shower particles. Each bunch is then ray-traced to observation level and checked for collection by a telescope mirror. Characteristic details of a bunch, such as the emission height, direction cosines of its trajectory, number of photons in the bunch,

arrival time upon striking the mirror, and identity of the parent particle may then be recorded.

Datasets of showers were generated by CORSIKA from files of initial parameters. Each INPUTS file contained user defined run information such as: the mass of cosmic ray primary; a differential energy spectrum and range from which the primary's energies were sampled; particle dependent energy cuts; and the zenith and azimuthal angles of the arrival direction of the primary. The CORSIKA coordinate frame defines all particle trajectories with respect to x (North), y (West) and z (Up). A more natural reference frame for ground-based measurements is the coordinate frame reflecting the pointing direction of the telescope. Thus a transformation to the telescope frame of reference was necessary for each Čerenkov photon striking the detector. Thanks to the geometry of an alt-azimuth telescope, this coordinate frame also coincides with the tilted plane of the shower front. Therefore, for non-vertical observations, only a single coordinate transformation was required for each incident photon.

The INPUTS file also included site information about Woomera: the height of observation level; the geomagnetic field strength and orientation; and the relative coordinates and dimensions of the BIGRAT mirrors. By default, all showers were necessarily created with the detector positioned at the shower core. A distribution of impact distances was then created by randomly distributing multiple telescopes within a user-defined core radius, R_{max}, for each shower. By resampling the same shower numerous times, the number of actual showers fully generated was reduced. When simulating inclined showers, this scattering radius was increased to accommodate their broader lateral spread. For these non-vertical showers, changes were made to

CORSIKA to define R_{max} in the tilted shower plane. Each shower was also repeatedly scattered within a solid angle defined by the half angle, θ_{max}, to simulate the random arrival directions of the cosmic ray primaries. The optimal values for R_{max} and θ_{max} will be estimated in section 5.4.1.

Computing time poses a problem when following the large number of shower particles. This is most evident at larger zenith angles where the increased atmospheric attenuation of the Čerenkov signal results in a dramatic increase in energy threshold of the detector. At 70° from the zenith, a typical cosmic ray dataset of 200 showers with energies exceeding 100 TeV may take weeks to run, even on a computer with substantial processing power. A thinning option is available, but for measurements at TeV energies provides little benefit. The amount of Čerenkov emission is relatively insensitive to particle energies above the Čerenkov threshold so our data may be affected by the thinning of particle numbers. For the increased energies of inclined showers, we have applied thinning for energies below 10^{-7} of the primary energy. Only a representative sample is then followed below this threshold energy. Absolute energy cuts on the secondary EAS particles have also been set at the Čerenkov threshold.

File storage is an important consideration because of the potentially large numbers of Čerenkov photons recorded from showers of substantial energy well above trigger threshold. Included by the HEGRA group is an option for defining a photon bunch size. Only information on the bunch as a whole is then recorded. The bunch size used here has been optimised so that after the addition of atmospheric transmission and photocathode quantum efficiency, the number of surviving photons from each bunch is approximately one.

A number of important mechanisms were identified for the realistic modelling of telescope performance. Atmospheric attenuation, photocathode quantum efficiency, mirror reflectivity and the response of PMT and cabling have all been folded with the Čerenkov yield. The resulting photoelectrons were fluctuated in the detector's angular field of view according to the measured blur spot of each parabolic mirror and collected by the PMTs. The telescope's central mirror also has the facility for mounting an imaging system but it was not used during this work. Pulse shapes were digitised in 0.1 ns steps before directly sampled sky noise pulses were added. Pulse height cuts were then applied to the signals from each PMT and temporal parameters (rise-time, FWHM, and fall-time) calculated for those coincident pulses triggering the system.

5.3 Modelling Telescope Performance

5.3.1 Instrumental Response

Čerenkov pulses typically have a FWHM less than 10 ns, which is often of shorter duration than the resolving time of an average detector. For an instrument with infinite bandwidth, the arrival time of each photon in the pulse would be determined exactly. Unfortunately, a real telescope suffers from timing limitations inherent in the PMTs, cabling and data acquisition system. This finite instrumental response results in a smoothing of the overall pulse shape through photoelectron pile-up. Separating the instrumental response from experimental data by de-convolution is difficult and tends to neglect fluctuations.

It is better to directly measure the instrumental response and incorporate this into the simulated pulses. The signal path from each triggering PMT was considered

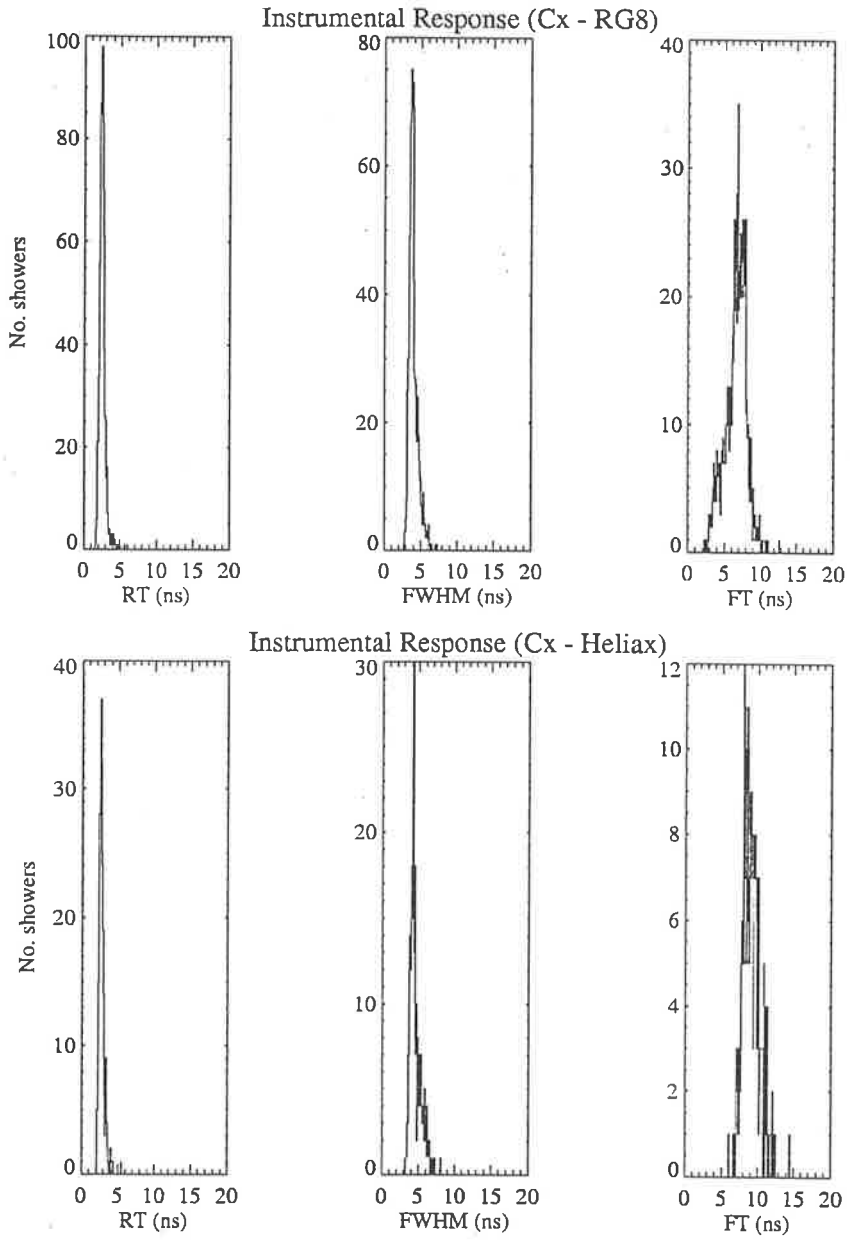

Figure 5.1: Rise-time, FWHM, and fall-time distributions for single photoelectron pulses. The top figures are for the signal path for the Cx tube using ~ 10 m of RG8 cabling, and the bottom figures show the distributions where the RG8 was replaced by ~ 110 m of Heliax cable.

independently. Each PMT was triggered in darkness by local muons traversing the small thickness of its glass faceplate. The duration of each pulse is much shorter than the detector response and may be thought of as an input δ-function to the system. These muon pulses broaden naturally as a result of the finite instrumental response, and we shall use them as an approximation of the response of the system to individual photoelectrons. Pulse height cuts were applied to the muon pulses in order to reject those small pulses lacking sufficient resolution for the reliable estimation of their parameter values. Those pulses, which were chosen, were normalised to a pulse height of one photoelectron for comparison with the calibrations in section 4.3. These "single photoelectron" pulses were then folded with the Čerenkov photons generated by CORSIKA. Figure 5.1 shows the fluctuations in the instrumental response for the Cx signal paths in the two trigger configurations described in chapter 4. The RG8 cabling setup is shown in the top figure and the lower bandwidth, Heliax setup in the bottom figure. Fluctuations in the trailing edge appear to be significant and will hinder the extraction of useful information on shower development from the fall-time parameter.

5.3.2 Estimating CORSIKA Trigger Thresholds

Following the inclusion of system response, mirror area, reflectivity, and atmospheric transmission in our modelling, the triggering of the pulse shape system is determined from a coincidence trigger between two applied pulse height thresholds. In section 4.3, we described various calibration techniques for converting our pulse height (voltage) measurements into the units of charge output by CORSIKA. In addition to these techniques, we can also examine the relative current gain between the two PMTs directly from datasets of real pulses recorded by BIGRAT. This allows

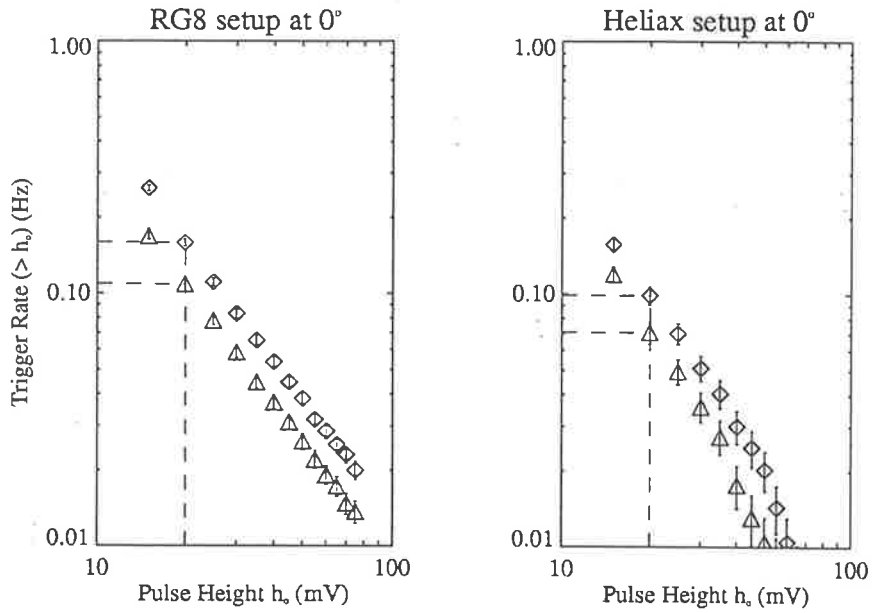

Figure 5.2: Integral pulse height distributions for Ax (Δ) and Cx (◊) signals measured at the zenith using (a) the RG8 cabling setup; and (b) the Heliax cabling setup. Standard deviation errors are included.

not only a relative calibration between the tubes, but also a direct verification that the performances of both PMTs (under the same lighting conditions) are consistent.

We have already mentioned that the pulse height distribution of atmospheric Čerenkov signals is well described by a power law (see section 3.6.1). Integral pulse height distributions of the Cx and Ax signals taken from zenith datasets collected with the RG8 and Heliax setups are plotted in figure 5.2. The power law exponent represented by the slope of each distribution is similar for each PMT. This gives us some confidence that neither of the tubes introduces any modification of the signals that we have not accounted for in the modelling. In the spirit of our previous calibrations, we may now estimate the relative conversion factor between the Ax and

Tube	Raw PH_{min} (mV)	Raw PH_{max} (mV)	Calibrated PH_{min} (pe)	Calibrated PH_{max} (pe)
Ax	5	34	15	110
Cx	14	34	55	135

(a) RG8 setup

Tube	Raw PH_{min} (mV)	Raw PH_{max} (mV)	Calibrated PH_{min} (pe)	Calibrated PH_{max} (pe)
Ax	5	34	20	140
Cx	7	34	35	170

(b) Heliax setup

Table 5.1: The min and max pulse height cuts (PH_{min} & PH_{max}), which will be applied to the BIGRAT data in the analysis in chapter 6, are quoted for each PMT before and after calibration. The values for the (a) RG8, and (b) Heliax cabling setups are shown. The maximal pulse height cut is needed to reject off-scale events (see section 4.2.4). A reduced PH_{min} has been applied for data collected with (b) to increase the statistics in these smaller datasets.

Cx signals by calculating their difference in trigger rate for a given trigger level. These will be combined into the absolute thresholds quoted later.

The energy threshold, E_{th}, for the telescope is fixed by the values of the Cx and Ax trigger thresholds. Absolute values for these trigger levels (and thus E_{th}) may be determined by matching the measured vertical event rate of BIGRAT with a simulated event rate. The latter rate is determined by considering the triggering efficiencies of the CORSIKA generated primaries. For heavier primaries, this efficiency decreases due to a reduced energy per nucleon available for the development of each sub-shower. This means that there will be an increased energy threshold for iron showers relative to protons. Since our definition of energy threshold (see

section 3.6.2) does not depend on the lowest energy, triggering event, we apply a minimum energy, $E_{\min}$, for each primary species when creating CORSIKA datasets. This reduces the waste in generating low energy showers incapable of triggering the telescope and hence reduces computing time.

The "observation" time in which N_{total} cosmic ray showers arriving in a solid angle, $\Omega_{\max}$, are collected at the ground in an area, $A_{\max}$, is given by

$$t_{obs} = \frac{N_{total}}{F_{CR}(>E) A_{\max} \Omega_{\max}} \tag{5.1}$$

Here, N_{total} is the number of CORSIKA generated events multiplied by the number of times each event is reused to produce impact points and arrival directions randomly scattered within the user defined maximum area and solid angle.

Calculating the event rate requires knowledge of the primary cosmic ray spectrum, $F_{CR}(>E)$, and also the triggering efficiency of the air Čerenkov signals for each species. For a comparison of rates at the zenith we make use of integral spectra estimated from JACEE measurements (Watson 1997) at TeV energies.

$$F_p(>E) = 0.06E^{-1.8} \quad \text{(proton)} \tag{5.2a}$$

$$F_{He}(>E) = 0.05E^{-1.7} \quad \text{(helium)} \tag{5.2b}$$

$$F_N(>E) = 0.02E^{-1.6} \quad \text{(nitrogen)} \tag{5.2c}$$

$$F_{Fe}(>E) = 0.01E^{-1.5} \quad \text{(iron)} \tag{5.2d}$$

	Proton	Helium	Nitrogen	Iron
Primary Flux (> 3 TeV) (m^{-2} sr^{-1} s^{-1})	0.0083	0.0076	0.0043	0.0023
% Trig Efficiency (> 3 TeV)	0.41	0.31	0.25	0.27
Triggered Flux (> 3 TeV) (normalised)	1	0.71	0.32	0.18

Table 5.2: The integral flux above 3 TeV, from JACEE measurements, for each CORSIKA primary considered in the simulations. The trigger efficiencies for each species, with respect to our modelled detector, have been estimated as described in section 3.6.2. The JACEE fluxes and trigger efficiencies have been combined to generate predictions for the triggered flux values, of each species, expected in the BIGRAT data. These have been normalised with respect to the triggered proton flux.

Each integral flux above is measured in m^{-2} s^{-1} sr^{-1} with energy, E, in TeV. Here, we have only quoted mean values of the flux for each primary.

The absolute trigger levels for Ax and Cx can now be estimated for both the RG8 and Heliax setups and are shown in Table 5.1. The thresholds applied to our measured pulse shape data in mV are included with the calibrated CORSIKA values in photoelectrons. The relative gain calibrations estimated earlier have also been accounted for. This calibration is similar to the results obtained in section 4.3, but we shall opt to use these values in preference since they are directly derived from our modelling of the atmosphere and detector as a whole.

Applying these trigger levels, we can estimate the relative likelihood of triggering the telescope for each species as a function of energy. This is described in table 5.2. All fluxes are referenced with respect to the minimum energy chosen for CORSIKA proton

events. The triggered composition derived from the JACEE predictions has been included for comparison with the results of our analysis in chapter 6.

5.3.3 Spectral Dependence and Atmospheric Transmission

The version of CORSIKA used for the simulations in this thesis does not assign spectral information to the photon bunches when created. Wavelengths were allocated later by sampling from the Čerenkov spectrum in the operating range of the PMT photocathode (300 – 600 nm). Photons were then converted to photoelectrons using the quantum efficiency curve of the bi-alkali photocathode (see figure 4.3). No wavelength dependence was included for mirror reflectivity.

The atmospheric model for standard US atmosphere 1976 is the default model used in CORSIKA. Atmospheric density profiles for other models are also available. Shower development has been shown to be sensitive to latitude and seasonal effects. Seasonal variations alone can cause a 15 – 20% shift in the Čerenkov photon density observed at ground level. For a detailed review of these effects the reader is referred to Bernlohr (2000). Unfortunately, seasonal effects were not known at the time of the data acquisition phase of this experiment, and therefore no investigation of such effects has been attempted in this work. Future experiments will need to plan their data collection across a full year's observation campaign so as to average over any seasonal bias in the event rates at different elevations. A mid-latitude summer model has been chosen for the analysis of this work purely out of simplicity. The data taken from this experiment was fairly evenly spread throughout the winter and summer months.

Atmospheric transmission of the optical Čerenkov light is not included in CORSIKA by default, and must be added externally. Rayleigh (molecular) scattering, ozone absorption and aerosol scattering are the most likely processes responsible for the attenuation of the Čerenkov signal. The effect of ozone absorption was expected to be minimal over the spectral range of the detector, but has still been included for completeness. We are interested in describing the attenuation as a function of emission height and wavelength. This is purely for the convenience of folding it with the detector response directly into our pulse shapes. We thus make use of attenuation coefficients for each process to derive look-up tables describing the total vertical transmission of the signal from a height, h, (up to a maximum of 30 km) to ground level. Values for these coefficients have been obtained from the Handbook of Optics (1978).

The amount of molecular scattering is proportional to λ^{-4} and is primarily responsible for the reduction in Čerenkov signal, which also peaks at small wavelengths. It also depends on the local atmospheric density, n_R, measured in m^{-3}. The attenuation coefficient as a function of vertical height is then described by

$$\beta_R(h) = \sigma_R n_R(h) \times 10^3 \text{ km}^{-1} \tag{5.3}$$

where σ_R is the wavelength dependent, Rayleigh scattering cross-section in m^2 and n_R is the density in m^{-3}. The mean value of this coefficient, $\overline{\beta}_R$, in each height increment, Δh, allows us to estimate the Rayleigh optical thickness between this height and sea level

$$\tau_R = \sum_0^h \overline{\beta}_R(h)\Delta h \tag{5.4}$$

The optical thickness for each scattering and absorption process may be combined linearly into a total optical thickness, τ_{total}. This can then be used to calculate the total atmospheric transmission from this height to that of the detector level, h_0, by

$$T(h,\theta_z) = e^{-(\tau_{total}(h)-\tau_{total}(h_0))\sec(\theta_z)} \tag{5.5}$$

This may be used for inclined showers ($\theta_z \leq 70°$) where the "plane-parallel atmosphere" approximation remains valid. For observations closer to the horizon, a realistic atmospheric curvature model is available in CORSIKA.

Mie scattering due to aerosols has been included in a general way, but the concentration of aerosols present can be highly variable from night to night and is totally site-dependent. Scattering depends on the amount of dust and water vapour present within a few km above ground level. Regular atmospheric monitoring is advised for Čerenkov measurements at large θ_z, where the aerosol variability is significantly increased. Unfortunately, during the course of the experiment no resources were available for such detailed measurements.

Atmospheric extinction measurements were attempted with BIGRAT to check the validity of our transmission model. The total extinction of light from a star can be estimated from a series of observations of the star's brightness at different elevations by fitting the function

$$I(\lambda) = I_0(\lambda)T(\lambda,\theta_z) \tag{5.6}$$

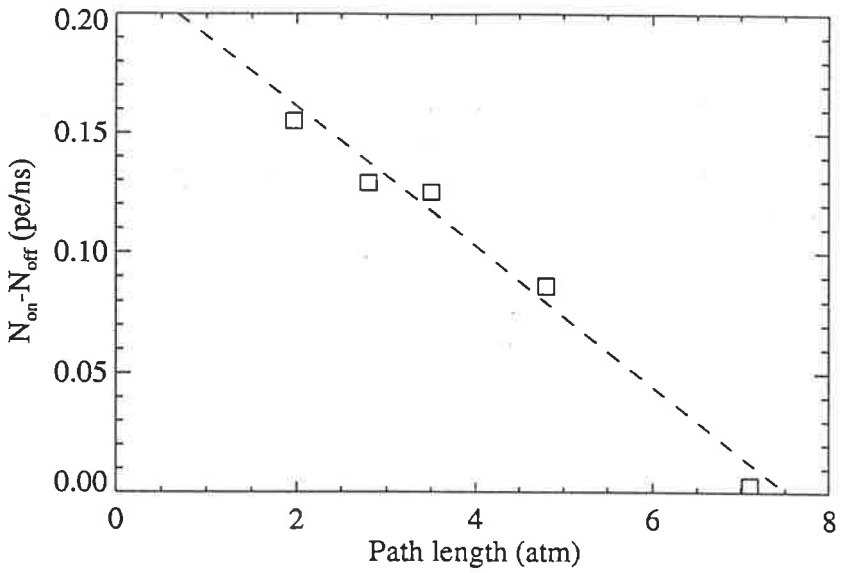

Figure 5.3: Atmospheric extinction measurements taken at Woomera with BIGRAT. The difference in mean sky noise rates for an on-source (containing the star "ε Sco") and an off-source region is plotted as a function of path length. The sky noise rates have been converted into units of pe/ns following section 5.2.2.

where I is the measured intensity from the star, I_0 is its true intensity, and T is the atmospheric transmission for inclined observations given in equation 5.3. We have used the telescope to track an on-source region (containing the star "ε Sco") and an off-source region (relatively free from stars) across a range of zenith angles. Random triggering of the telescope, at various elevations, collected sky noise pulses characterising the observed brightness in each direction. Following section 4.3.2, we determine the mean sky noise level for each dataset by first calculating the fluctuation level in each 50 ns triggering sample with respect to the mean baseline of the trace. The mean noise level is then obtained from equation 4.6. Dividing this by the duration of the trace (50 ns) gives us a sky noise rate in mV/ns, which can be converted to units of pe/ns according to the calibrations in the previous section.

The difference between on-source and off-source brightness gives an intensity, I, which is plotted as a function of atmospheric thickness, $\sec(\theta_z)$, in figure 5.3. A linear fit indicates a drop in brightness of 16% for each additional airmass traversed. This is in reasonable agreement with other more detailed, extinction measurements made at Woomera (McGee 2000) which predict a drop of ~ 20% per air mass. The reduction appears to be less significant than that predicted by our atmospheric transmission model. However, as we shall see in chapter 6, the observed relationship between trigger rate and θ_z is difficult to reconcile without resorting to such an attenuation model.

For our model, both Rayleigh and Mie scattering are treated as absorption mechanisms. In other words, we have assumed only single scatterings have occurred – either the photon is scattered out of our detector's acceptance angle or it is not. No accounting for the multiple scattering of photons back into the beam has been considered. For Rayleigh scattering, which dominates the atmospheric attenuation during clear nights, propagation delays due to multiple scattering over a large range of altitude might significantly distort the Čerenkov pulse shape. As we shall see in section 6.2.1, there are difficulties in recreating the FWHM and fall-time distributions accurately. The pulse widths are underestimated with respect to our measured data, and this discrepancy becomes worse with increasing θ_z, suggesting a source of signal delays has been neglected from our modelling. The maximum number of molecular scatterings which Čerenkov photons might experience travelling from a typical depth of shower maximum to ground level ranges from about three (Handbook of Geophysics 1965), for observations at the zenith, to about six or seven at $\theta_z = 70°$. The increased path length

differences for photons scattered by small angles in inclined showers suggests that if multiple scattering is important, then the signal delays will increase with zenith angle.

Whereas Mie scattering is highly forward scattered, Rayleigh scattering is nearly isotropic and the expected probability of collecting multiply scattered photons in our small aperture detector is expected to be very small. Thus, it seems the Čerenkov pulse shape may not be overly sensitive to this. A more detailed treatment of this mechanism is still needed for future timing analysis. The contribution of multiple scattering to uncertainties in fluorescence measurements is currently being studied for the Auger project (Matthews 2001).

5.3.4 Sky Noise Blurring of Čerenkov Pulses

As outlined in section 3.6.1, the background illumination from stars is a problematic source of noise for the measurement of faint Čerenkov signals. The intensity of this sky noise fluctuates greatly with changes in the atmosphere and with the particular star field viewed during the course of a run. To monitor this, sky noise was directly sampled before and after each observation run by randomly triggering the system on the night sky. This ensured a record of the general lighting conditions for every dataset recorded. Each sample trace was cleaned of accidental muon triggers by applying a pulse height cut, converted to units of photoelectrons and added to the simulated Čerenkov pulses.

Random sky noise fluctuations distort the arrival time information obtainable from a Čerenkov signal. It is useful to identify a pulse height threshold above which the effects of sky noise blurring become negligible. From the file of instrumental response pulses described in section 5.3.1, a sufficiently large "test" pulse (bearing roughly the mean

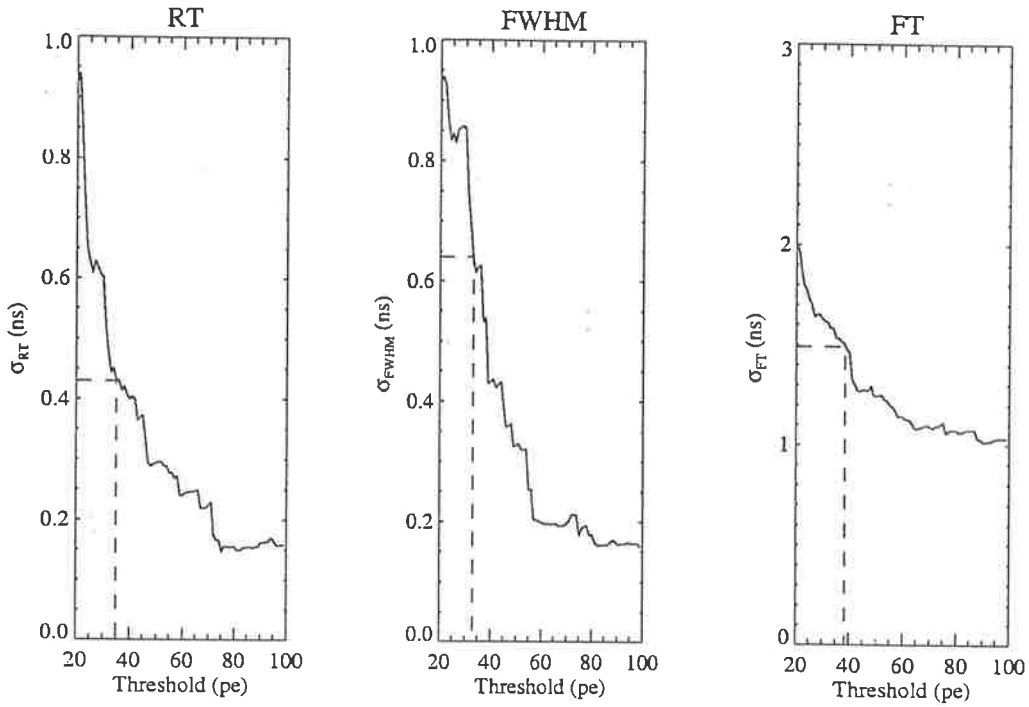

Figure 5.4: The sky noise blurring level described by the standard deviation for each pulse parameter as a function of trigger threshold. The dashed line shows the fluctuation level for each parameter due to instrumental response.

values of rise-time, FWHM and fall-time) was chosen. A pulse height distribution was obtained by assigning pulse heights (randomly chosen from a spectrum) to multiple instances of the test pulse. Properly calibrated sky noise was then added. The variance in pulse shape parameters as a function of trigger threshold is shown in figure 5.4. The point at which the fluctuations due to sky noise blurring become less than the intrinsic fluctuations in the system response occurs at a threshold of 35 pe.

5.4 Detector Bias in the Pulse Data

In any non-ideal detector, instrumental limitations will affect the measurements. For the accurate modelling of a telescope's performance it is important to identify as many potential sources of this bias as possible.

5.4.1 Sensitivity to Energy Threshold and Collecting Area

Each CORSIKA dataset was created based on a set of initial parameters. A poor choice of these would greatly harm the ability of the simulations to accurately describe our measurements. An overestimate of the minimum energy for the spectrum we are sampling our cosmic rays from will needlessly omit low energy showers that may have triggered the telescope. The event rate will then be underestimated. Shower size, and the resulting longitudinal spread of these particles, is energy dependent (Allan 1971). The mean pulse width thus increases with primary energy. Therefore, overestimating the minimum energy will introduce an artificial increase in the mean pulse width of the triggered dataset as shown in figure 5.5(a). It is safer to underestimate the minimum energy required, but this will greatly increase the required computing time by creating many spurious showers incapable of triggering the system.

We have already seen the difficulties in calibrating our pulse shape measurements with precision. By matching event rates between simulations and measurement we have optimised our calibration to reduce trigger bias. However, an incorrect choice of trigger thresholds will further bias the pulse data, as shown in figure 5.5(b), since the variation in FWHM values increases with decreasing pulse height. This is the result

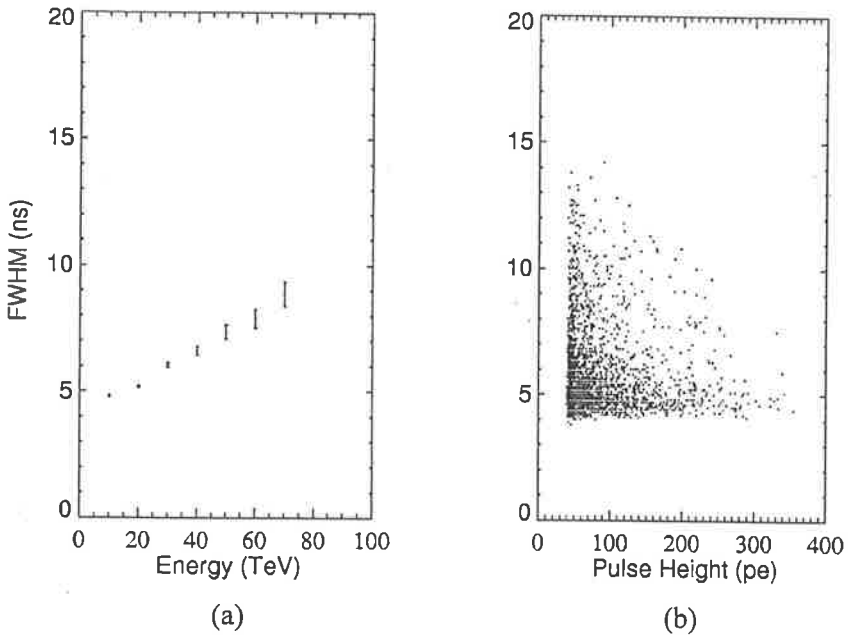

Figure 5.5: The sensitivity of FWHM values, for a dataset of simulated vertical proton showers, to (a) primary energy, and (b) pulse height. The reasons for this are discussed in the text.

of core distance effects. Reducing thresholds allows the detector to trigger on showers at larger core distances where the spread in pulse widths becomes greater. The relationship between FWHM and core distance will be introduced in figure 5.8.

We assign core distances to our events by randomly scattering our detector in a circle of radius, R_{max}, defined in the tilted shower plane. At large core distances, there is a significant increase in the mean FWHM and therefore, if R_{max} is not sufficiently large, we may neglect large FWHM events far from the core. For the work in this thesis we have used R_{max} values of 350 m at the zenith; 500 m at 60°; and 600 m at 70°.

The early studies of timing information from Čerenkov signals were made with wide aperture detectors. A detector with a small angular field of view such as BIGRAT introduces its own bias to the collected data. Large angle Čerenkov emission from showers at large core distances will fall outside the detector's aperture. However this is complicated by the fact that cosmic ray primaries arrive from all directions. It is thus possible for a significant number of off-axis, large core distance showers to trigger the telescope.

CORSIKA primaries have been generated with the assumption that they all arrive from a single direction coinciding with the direction in which the telescope is pointing. To model the random arrival directions of the cosmic rays, the angular image of each Čerenkov signal was randomly scattered within a solid angle defined by the half angle, θ_{max}. This solid angle was chosen to contain the largest off-axis shower thought to be capable of triggering the telescope. The sensitivity of the pulse shape parameters and trigger rate to the value of θ_{max} is shown in figure 5.6. Again, the FWHM increases with θ_{max} because of larger angle emission from showers at large core distances. As the zenith angle of observation increases, the increased path length through the atmosphere will enhance the Čerenkov light from higher energy particles closer to the core. This results in a decrease in the size of the angular image and therefore there is also a reduction in the optimal solid angle. This work has used θ_{max} values of 3° at the zenith, and 2° for inclined showers at 60° and 70° from the zenith.

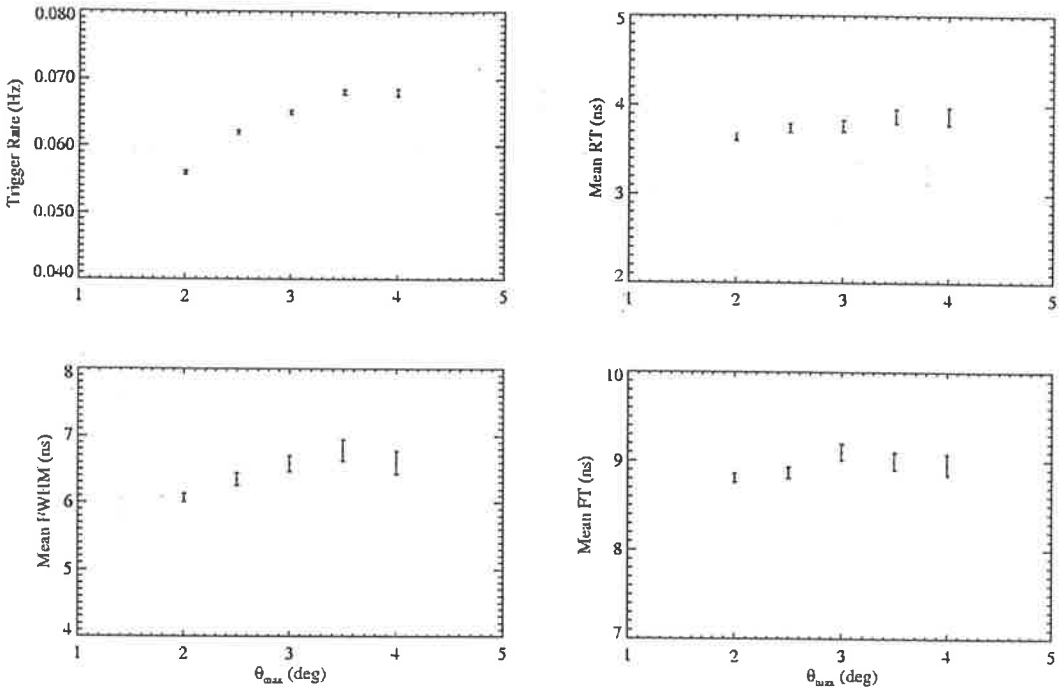

Figure 5.6: The sensitivity of the trigger rate and mean pulse parameters to the applied value of θ_{max}, for a dataset of vertical simulated proton showers. Trigger rate errors are given by Poisson statistics, and the pulse parameter errors are standard errors in the mean values.

5.4.2 Data Acquisition Bias

In the last section we considered some potential problems in modelling a cosmic ray experiment using an ideal detector. No mention was made of the bias introduced by the detector itself in collecting the Čerenkov pulse data. We have already discussed the finite time response of the detector. Now we need to consider the size of the sampling window of the data acquisition system.

Until now, we have only defined the triggering of our system by the acceptance of a minimum pulse height. However, there is also a maximum pulse height set by the

voltage range of the sampling window. Pulses that are too large stretch beyond the maximum voltage visible in this window and make the determination of pulse shape parameters uncertain. Such data were still recorded but have not been considered for analysis. A pulse height cut on the measured pulses does not necessarily define an absolute cut on the Čerenkov pulse height distribution. Fluctuations in the noise level will move a pulse, whose height is close to the trigger threshold, above or below this threshold. The triggered pulse height distribution may then depart from the correct distribution, possibly a power law, near this threshold.

The sampling window defines a finite time window of 50 ns. Each signal was delayed to ensure the complete capture of the leading edge of each pulse. Due to small differences in cable length, the Ax signal was delayed relative to the Cx signal by about 15 ns. For some wider pulses, the trailing edge of the Ax signals extended beyond the window, and the fall-time (and sometimes the FWHM) parameter could not be determined. Since the Ax signals were mainly used for triggering only, this did not cause much of a problem. At larger zenith angles, the increased width of the pulse leading edge increased the number of pulses with some portion lying outside the window. Pulses from the Cx PMT were not considered for analysis if either the FWHM or fall-time parameters could not be determined. These same parameter cuts have been applied to the simulated datasets. Cable delays have also been included in the modelling with the addition of a fixed time offset to the simulated Ax signals prior to cuts.

5.5 Pulse Shape Interpretation

5.5.1 A Simple Model

Čerenkov photons arrive at the ground following their production across a large range of altitude. Therefore, we should expect the observed pulse shape to contain some measure of the longitudinal development of a shower. The arrival times of the photons are related to their height of emission in a way that is sensitive to where they fall relative to the shower core.

For the moment, let us assume that the only Čerenkov emission arising from the shower is that due to the electromagnetic component. We have already seen (from chapter 3) that this component dominates the lateral and longitudinal extent of the shower. We will further assume that all shower particles travel along the core of the shower with a speed, c. Following figure 5.7, we consider Čerenkov pulses from two different points in the shower's development. After photons emitted at A hit the ground at a distance, D, from the shower core, the shower particles continue on their path from A to B. Emission from point, B, (lower in the atmosphere) then arrives after the light from A by a purely geometric argument. The path length, AD, is shorter than the path length, $AB + BD$.

Unfortunately, this argument is complicated by the fact that the emitted photons do not travel through the atmosphere with the same speed as the shower particles. Refraction of these photons in the air produces timing delays at the point of observation. These must be added to those due to geometric path differences alone. Such refractive index delays exceed the path delays at small core distances. The shower particles then

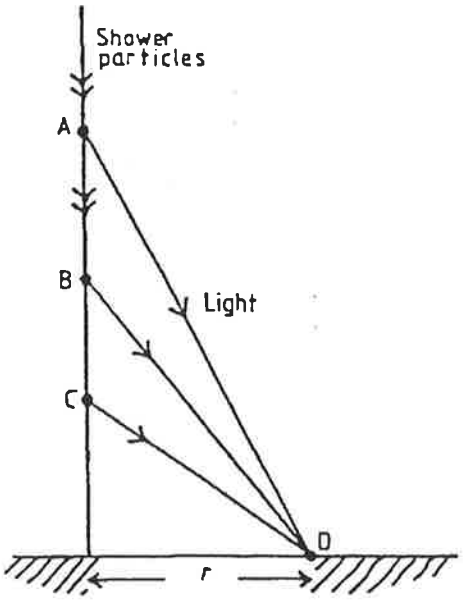

Figure 5.7: Schematic diagram showing the path length differences arising from the emission of light, at various stages of shower development, to its observation at a common point on the ground (from Hillas 1982).

overtake the Čerenkov front and photons emitted at low altitudes will arrive before those emitted from the top of the shower. As we move our detector at D away from the core, the path delays increase until they overwhelm the refractive delays. Now, light from the top of the shower will arrive first. This implies the existence of a core distance at which the two effects cancel each other out and emission from a large range of height arrives simultaneously. The implications of this for pulse shape formation will be addressed in the remainder of this section.

This effect coincides with the location of the Čerenkov "shoulder" at about 150 m from the core for vertical showers. In figure 5.8, the FWHM for Čerenkov pulses detected by a narrow field of view detector has been plotted with respect to core distance for a series of simulated vertical proton showers. The minimum FWHM is not zero as predicted

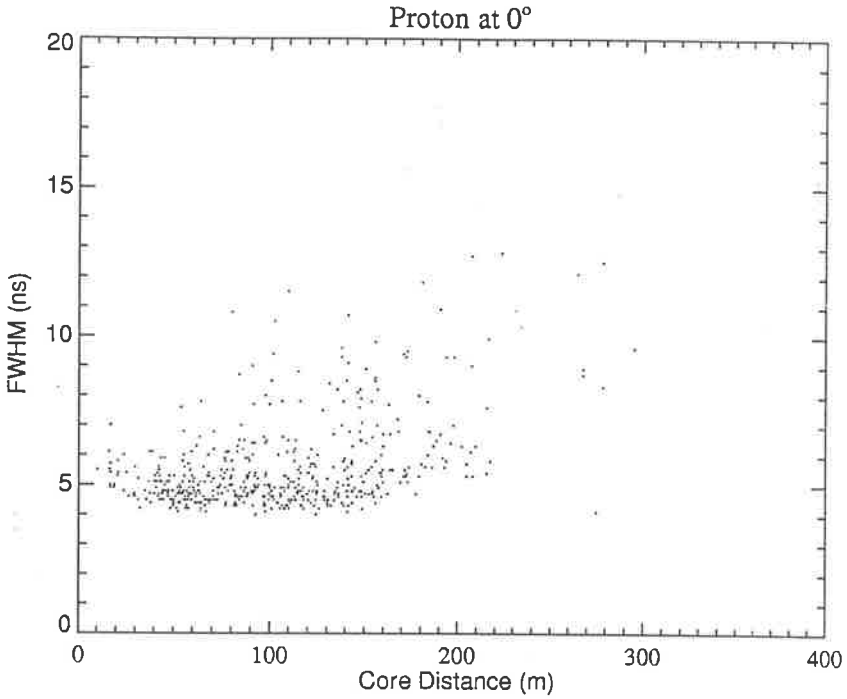

Figure 5.8: The relationship between core distance and FWHM for a series of simulated proton showers at the zenith.

because of the inclusion of detector response and the complexity of the real atmosphere compared to our simple model. The preceding argument also ignores the effect of the finite thickness of the shower front and the lateral spreading of the particles away from the shower core. These are responsible for the observed fluctuations. A review of such effects can be found in Allan (1971).

The general trends in pulse shape formation due to shower development have been well summarised elsewhere (Roberts 1993). The bulk of the Čerenkov emission appears to be produced by the portion of the electromagnetic component near the core. This results in a short pulse of only a few nanoseconds duration at the point of observation. Emission from particles far from the core causes a widening of the

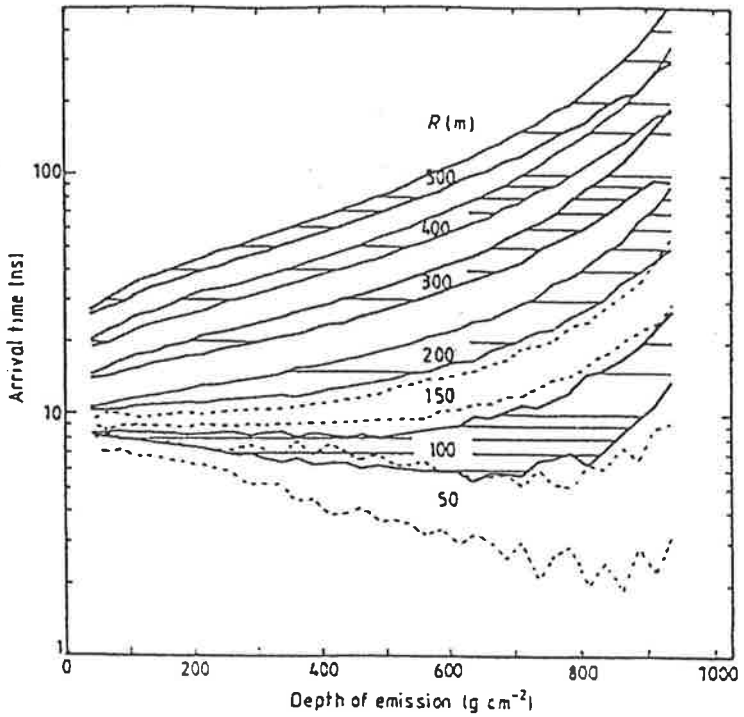

Figure 5.9: The dependence of the spread of photon arrival times on the depth of emission. For core distances, *R*, greater than 150 m, a simple relationship exists (from Hillas 1982).

pulse. Since the latter photons lag behind the emission near the core, they naturally extend the trailing edge of the pulse.

Čerenkov timing experiments have anticipated that longitudinal information from shower development may be recoverable from the pulse shape. This depends strongly on core distance. Refractive delays distort the relationship between the height of emission and the arrival time of the photons for measurements at small core distances. Figure 5.9 shows the spread in photon arrival times as a function of emission depth for pulses measured by wide aperture detectors at various core distances. We can see that a simple relationship only exists at distances far from the core. This motivated earlier pulse shape experiments that used wide aperture detectors at large core distances. In

addition to the longitudinal information from the electromagnetic component, we will see in the next section that it is also possible to obtain primary mass information from the pulse shape by considering emission from the muon component.

5.5.2 The Local Muon signal

The number of muons in an EAS is a signature of the mass of a cosmic ray primary. A proton initiated shower produces only a relatively small number of muons, each carrying a lot of energy. On the other hand a heavier primary will be much more abundant in its muon production. This arises because of the increased meson multiplicity for heavier showers, as discussed in section 2.4. From here on, we shall refer to the Čerenkov light produced by muons as the "muon signal".

An investigation of the rise-time, FWHM and fall-time distributions for the Čerenkov pulses from a dataset of CORSIKA generated showers will help us identify the parameter most sensitive to the muon signal. We shall consider a set of vertical proton showers, applying the triggering conditions described in section 5.3.2. Figure 5.10 presents the resulting parameter distributions shown both with, and without, the muon signal included. The rise-time distribution appears to contain much of the available muon information. This is consistent with preliminary composition work by Roberts et al. (1998) and Roberts (2000). He proposed that the muon signal might separate sufficiently from the electromagnetic signal in the detected pulse so as to be a strong identifier of mass composition. It was also suggested that this discrimination should improve at larger zenith angles because of the increased distance to shower

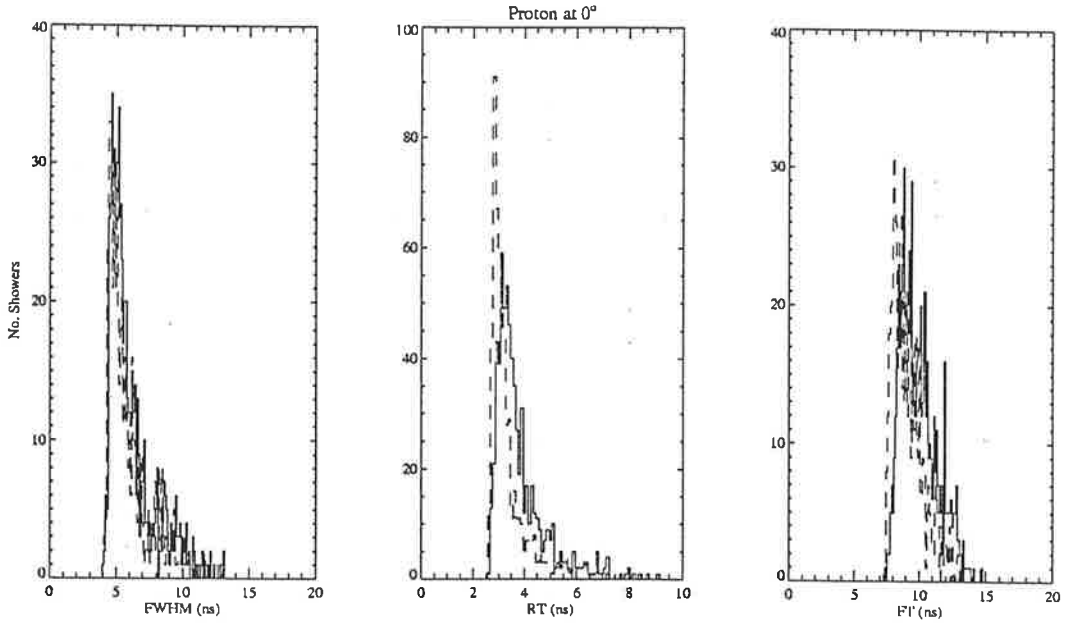

Figure 5.10: RT, FWHM & FT distributions for CORSIKA protons arriving from the zenith. The solid lines describe the total pulses and the dashed lines represent the pulse data where the muon signal has not been included.

maximum further delaying the electromagnetic pulse. We will consider this in more detail in the next section.

5.5.3 Observations at Large Zenith Angles

The steep power law of the cosmic ray energy spectrum suggests that the events triggering a detector will be dominated by primaries with energies close to the threshold energy of the detector. We may then probe higher energy primaries by increasing the energy threshold. However, a simple raising of individual trigger thresholds is not enough. Due to the steep energy spectrum, the arrival rate of the primaries is too greatly reduced at higher energies to be of practical use. Alternatively, if we increase our angle of observation away from the zenith then the path length from shower

maximum to the ground increases and the Čerenkov light is dispersed over a larger area, reducing the photon density on the ground. This causes a natural increase in threshold energy and the increased size of the Čerenkov pool on the ground greatly increases the detector's collecting area. A useful event rate may then be maintained over a large energy range.

Sommers and Elbert (1987) investigated this in order to promote the observation of PeV γ-ray signals at low elevations. They claimed an improvement in signal-to-noise ratio with increasing zenith angle for those γ-ray sources with spectra much flatter than the cosmic ray spectrum. Their results were based only on geometric arguments and neglected atmospheric attenuation of their Čerenkov signals. Without these signal losses, the predicted energy threshold will be substantially underestimated (particularly at large zenith angles). Figure 5.11 shows the zenith angle dependence of threshold energy and collecting area respectively for proton and iron showers triggering BIGRAT. The dependence of the integral triggering efficiency is also shown where it has been calculated with respect to the minimum energy of each CORSIKA dataset. These have been determined from detailed Monte Carlo simulations. Atmospheric attenuation and sky noise have been included in these results.

For the analysis of our BIGRAT data, sets of CORSIKA generated protons, helium, nitrogen and iron have been generated at 0°, 60° and 70° from the zenith. These will be used to test our pulse shape measurements against mixtures of varying composition in chapter 6. The parameter distributions for each mass primary and zenith angle are presented in figures 5.12, 5.13, 5.14 and 5.15. Initial inspection of these results shows that the rise-time distribution significantly broadens with increasingly heavy primaries

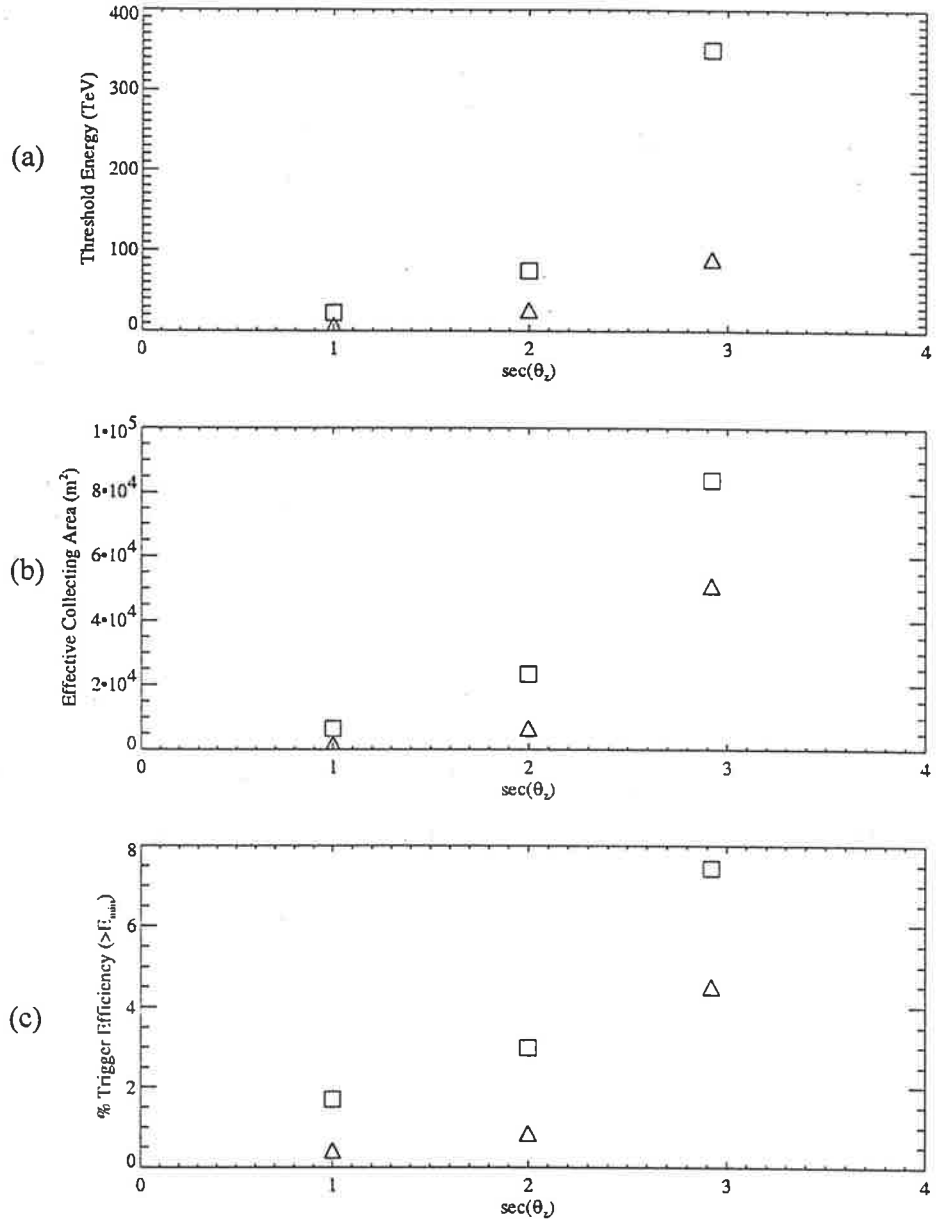

Figure 5.11: The zenith angle dependence for proton (Δ) and iron (□) primaries of the: (a) energy threshold; (b) collecting area; and (c) integral trigger efficiency (which is defined with respect to the minimum energy of each dataset).

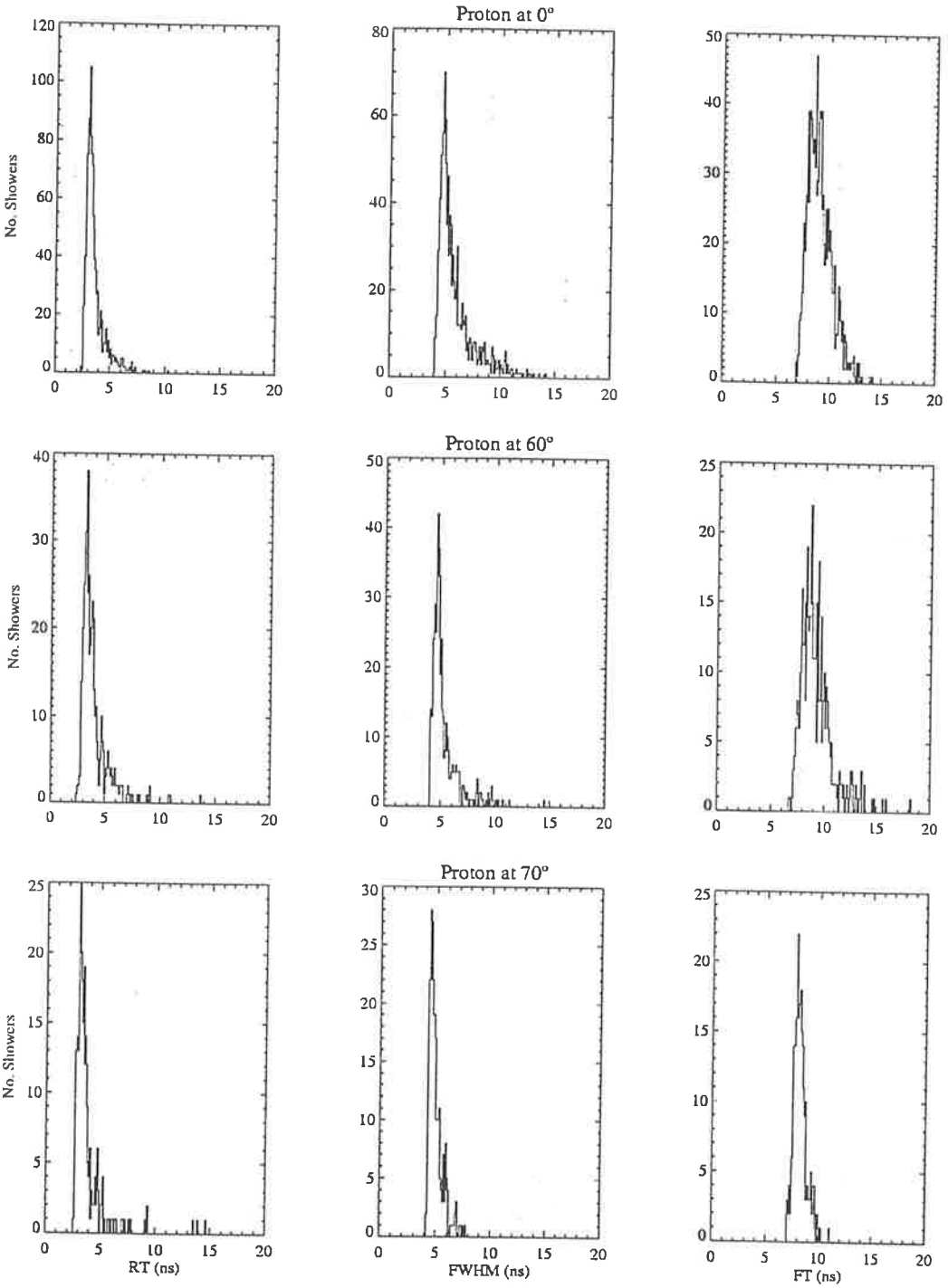

Figure 5.12: Rise-time, FWHM and fall-time distributions for CORSIKA generated proton showers arriving from different zenith angles: (top) 0°, (middle) 60°, and (bottom) 70°. Only those events are collected that satisfy the RG8 triggering criteria of section 5.2.2.

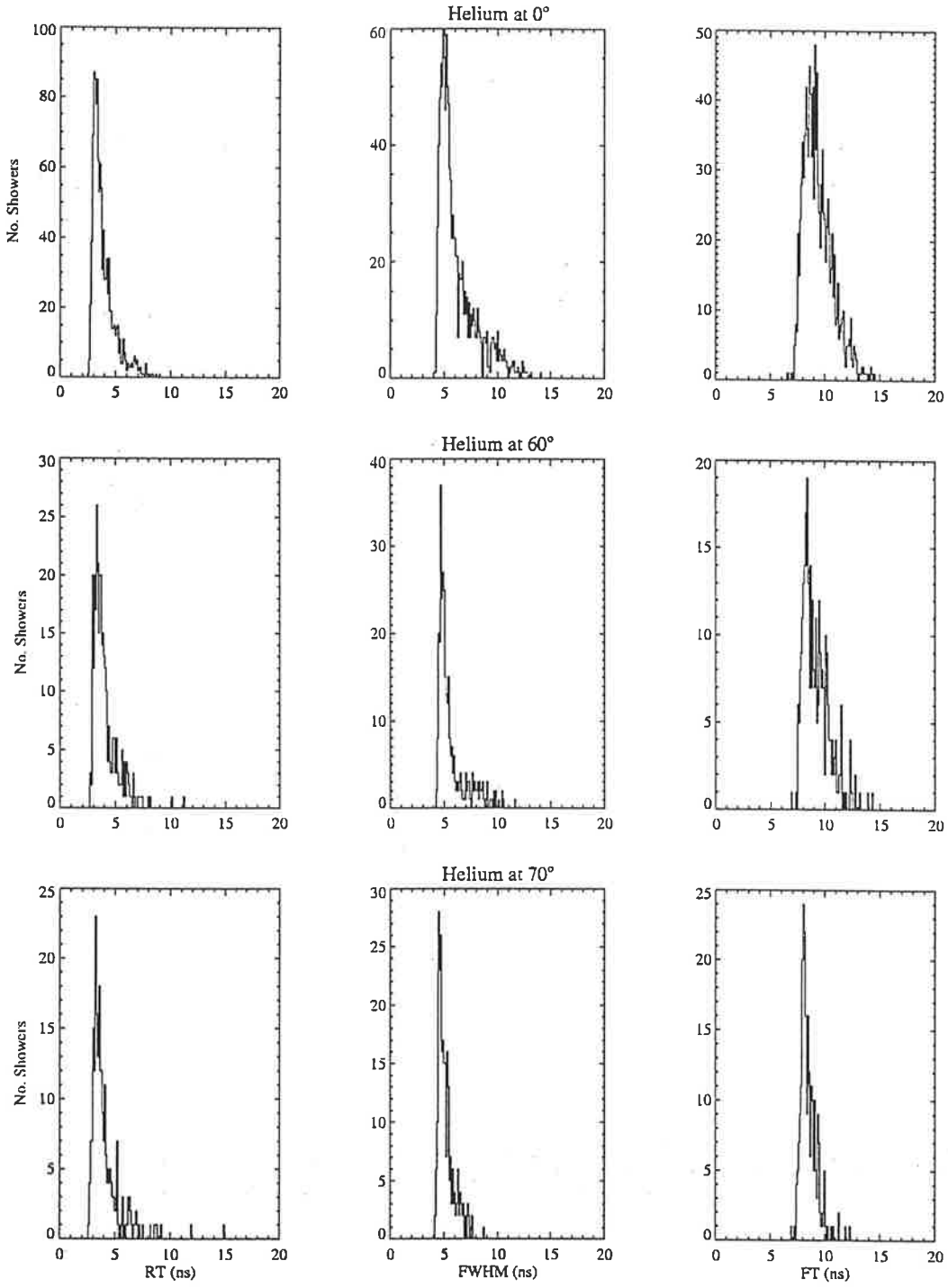

Figure 5.13: As described in figure 5.12, but for helium showers.

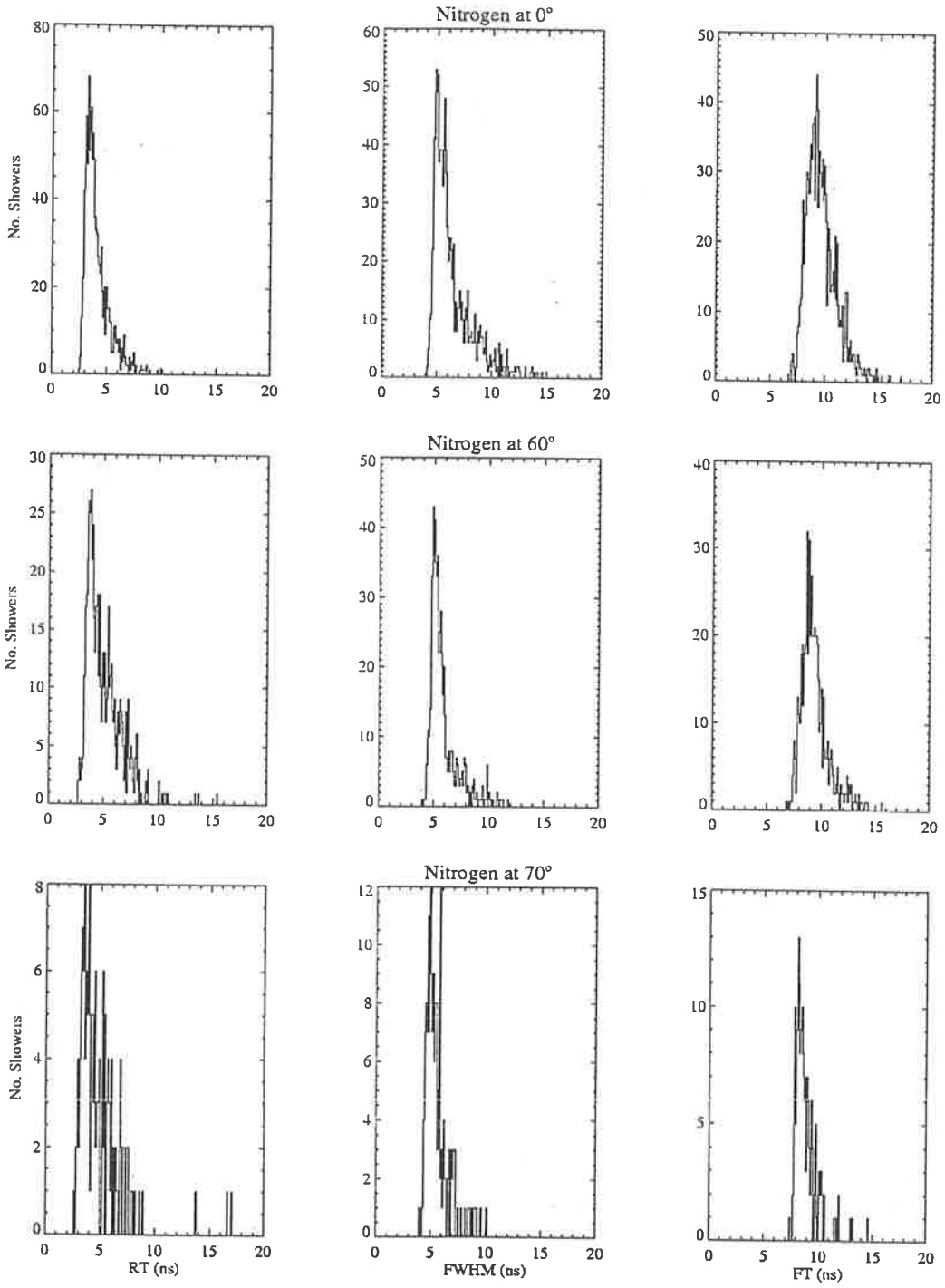

Figure 5.14: As described in figure 5.12, but for nitrogen showers.

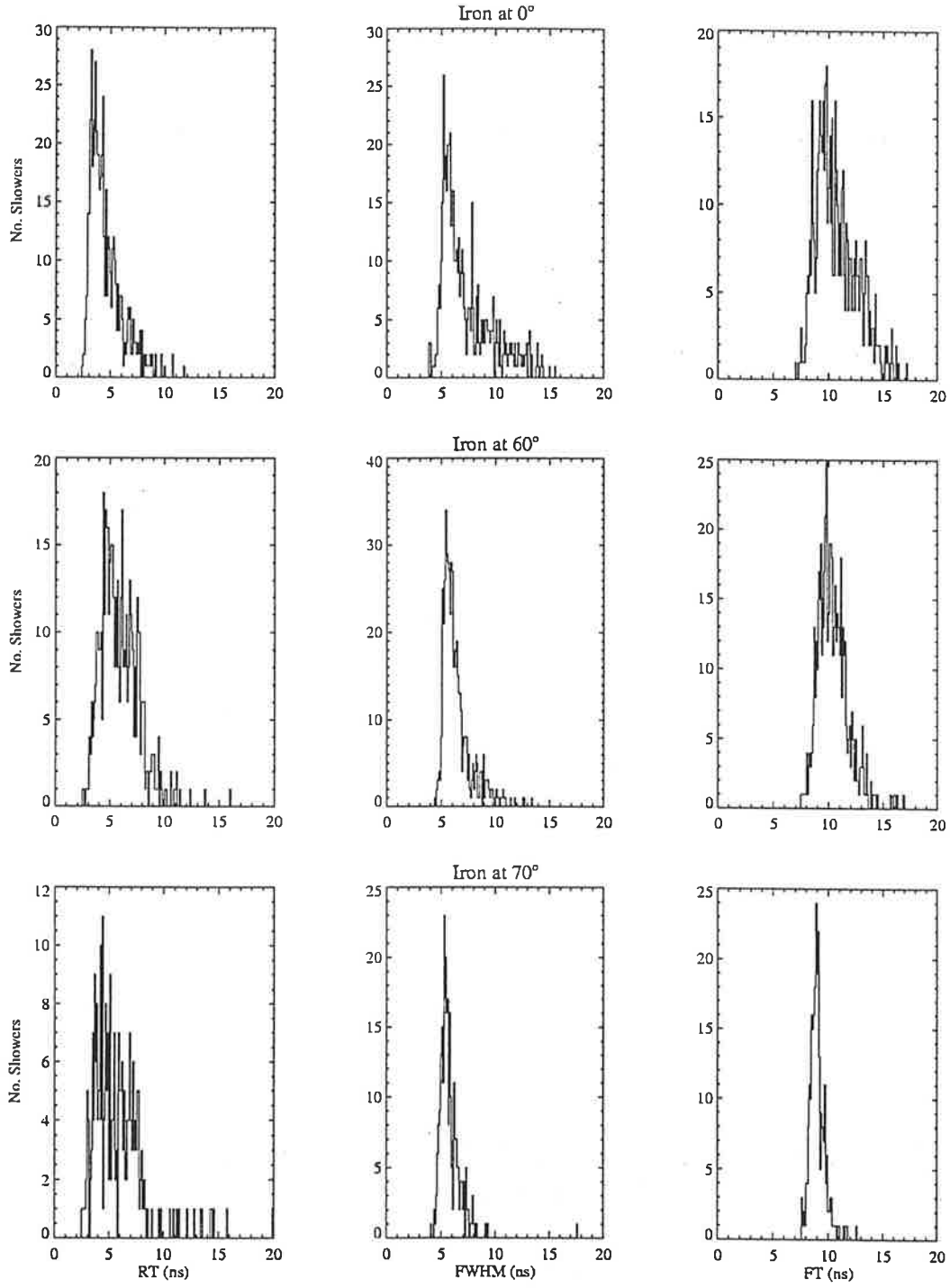

Figure 5.15: As described in figure 5.12, but for iron showers.

and also with increasing zenith angle for a given primary as predicted in the previous section. The FWHM and fall-time distributions also broaden with increasing mass. However, unlike the rise-time distribution, they appear to become narrower with increasing zenith angle for a given mass primary. This is an effect of the increased distance from shower maximum to ground level for inclined showers relative to those at the zenith. The reduction in curvature of the shower front of such showers results in a flatter relationship, between pulse width and core distance, than seen in figure 5.8.

We now examine the rise-time distributions for inclined showers in more detail in the interests of studying the possible effectiveness of mass discrimination at large zenith angles. A comparison of the muon information present in the proton and iron datasets at zenith angles, 0° and 70° has been made in figure 5.16. In much the same way as figure 5.10, the rise-time distributions of each are presented for the case where the muon signal is included and where it has been omitted. The iron primaries show a greatly increased muon signal at the zenith. As the zenith angle of observation increases, the rise-time distribution for the protons does not appear to change greatly from the zenith to 70°. Contrary to this, the iron data shows a noticeably broader rise-time distribution at low elevations due to the muon information. This suggests the possibility of an enhancement in the discrimination between proton and iron showers at large zenith angles based on rise-time information alone.

To interpret how the rise-time parameter relates to the muon information in a physical sense, we need to discuss the relative emission heights for the electromagnetic and muon components. We begin by defining mean emission heights, $\overline{Z}_{emission}(em)$ and $\overline{Z}_{emission}(\mu)$, for the electromagnetic and muon signals respectively. A scatter plot of

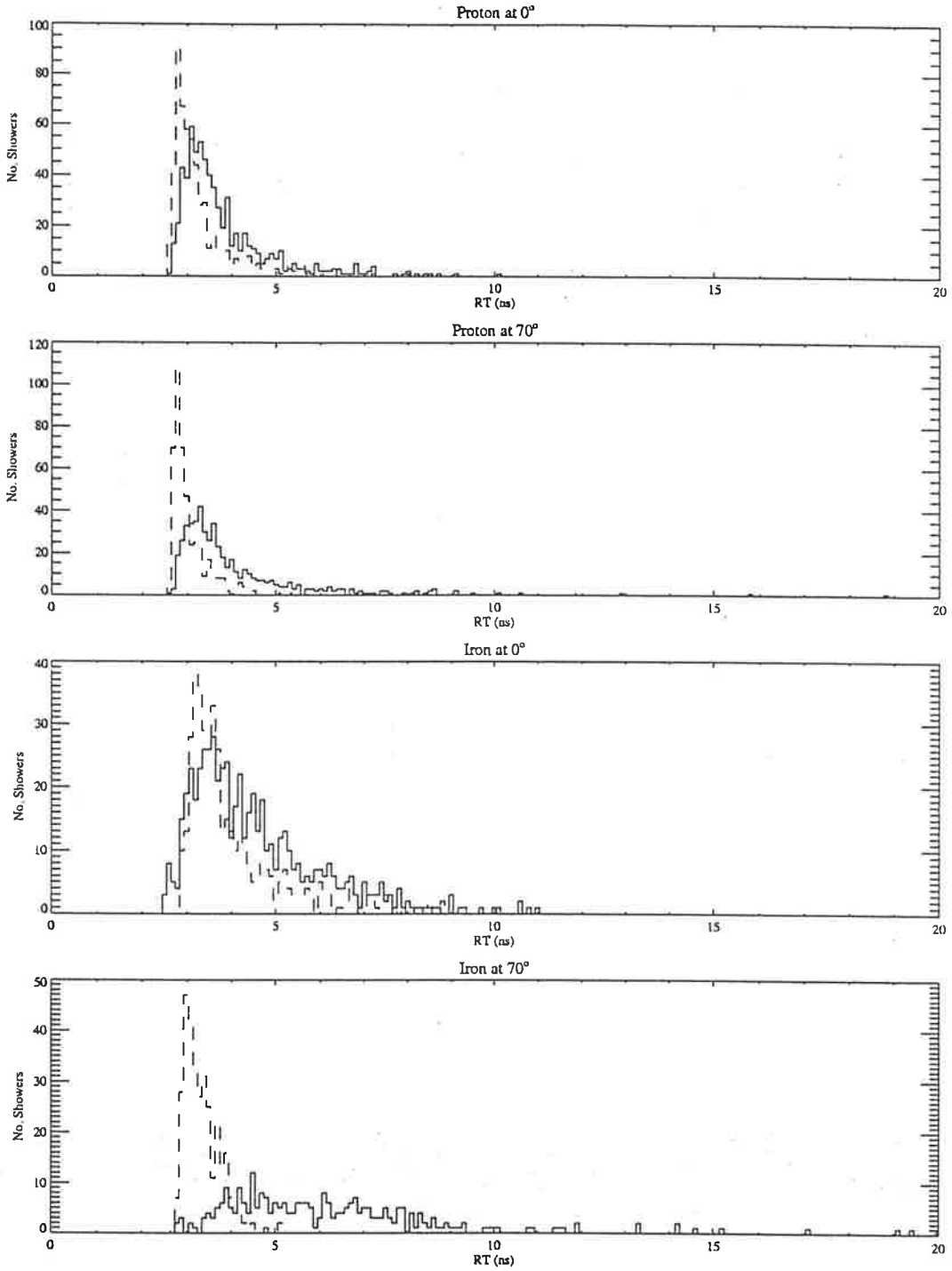

Figure 5.16: A comparison of the muon signal present in the rise-time distributions for: (a) proton and (b) iron showers at the zenith; and for them again at a zenith angle of 70° described in (c) and (d) respectively. The solid line distributions are where the entire pulse has been considered, whereas the dashed line distributions are for those pulses where the muon information has been left out.

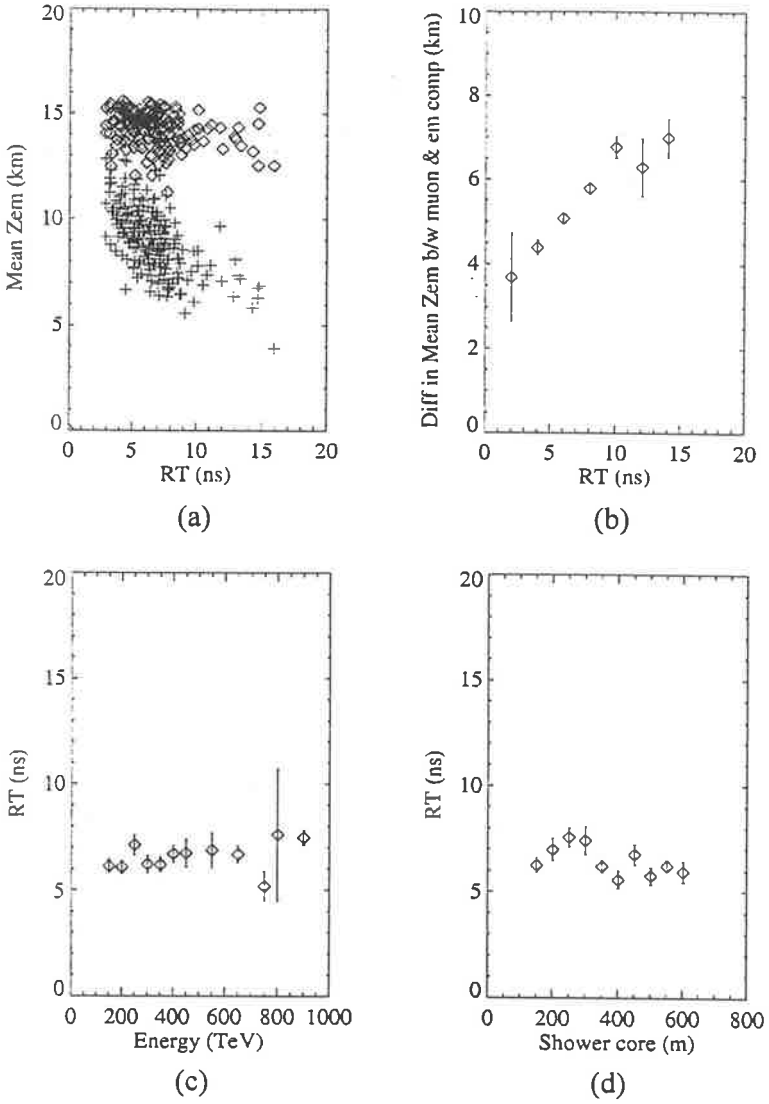

Figure 5.17: The behaviour of the rise-time parameter, at 70° from the zenith, is shown for a dataset of iron showers. The dependence of rise-time on mean emission height for both the electromagnetic (◊) and muon (+) signals is shown in (a) as a scatter plot, and (b) as the averaged difference of the emission heights of these signals. This difference is shown to increase with rise-time. Also shown is the dependence of the rise-time parameter on (c) primary energy and (d) core distance for the same dataset.

these heights as a function of rise-time, for iron showers generated at 70° from the zenith, is shown in figure 5.17(a).

The muons penetrate through the atmosphere all the way to ground level unlike the electromagnetic component, which dies out at higher altitudes. Thus, the muon emission may occur lower in the atmosphere as shown. The variance in emission height appears larger for the muons. This reflects the fact that the emission originates from a much smaller number of particles than for the electromagnetic component, and fluctuations in these signals observed at ground level will be more significant. Fortunately, the muon signal may still be comparable in intensity to the emission from shower electrons, since it originates from a larger range of altitude. At low altitudes, the relative intensity of the muon signal is further enhanced due to atmospheric attenuation of the main pulse at higher altitudes.

Figure 5.17(b) shows the difference between the emission heights of the two signals as a function of rise-time. Each point is defined by the average of the mean emission heights from 5.17(a) within each rise-time bin. Clearly, the difference in emission height increases with rise-time. This strongly suggests that the rise-time parameter is purely a result of the path delays between the two signals. The rise-time parameter also does not appear to change rapidly with primary energy (and hence depth of first interaction) or with core distance as shown in figures 5.17(c) and (d) respectively. This is particularly important considering the degree of uncertainty within our estimate of the energy threshold of our detector due to difficulties in accurately modelling the atmospherics.

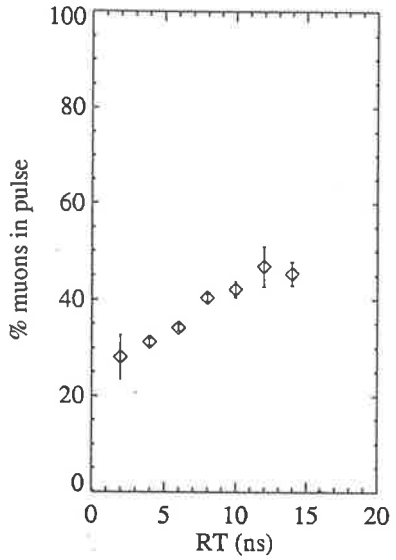

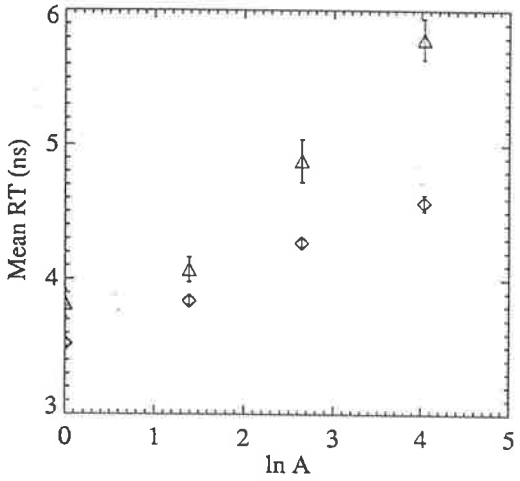

Figure 5.18: (left) The mean fraction of muon signal present in the total pulse as a function of rise-time for the dataset of iron showers used in figure 5.17.

Figure 5.19: (right) The variation of mean rise-time with primary mass, A, for zenith angles 0° (◊) and 70° (Δ).

The fraction of muon signal collected in the total pulse also appears to be related to the rise-time as shown in figure 5.18. However, this does not necessarily suggest an increase in the number of muons in those showers that produce pulses with large rise-times. We have seen in figure 5.17(a) that the rise-time will increase with decreasing height of muon emission. Therefore, the effect in figure 5.18 is probably due to the reduced attenuation of local muon signals with respect to that of the soft component.

So far we have discussed the physical mechanism behind the effectiveness of the rise-time parameter as a mass composition discriminator. However, we have not yet quantified the relationship between rise-time and primary mass. The mean rise-time for each CORSIKA dataset is plotted as a function of ln A in figure 5.19. Information on

proton, helium, nitrogen and iron are presented for zenith angles, 0° and 70°. The correlation between mean rise-time and ln A is fairly good with one major exception. The discrimination between helium and protons becomes difficult at large zenith angles. This is due to an increase in mean rise-time with zenith angle, for the proton showers, larger than is predicted by this relationship. Nevertheless, this gives us some indication of how the mean mass will scale with rise-time in the composition analysis of the next chapter.

Chapter 6

ESTIMATING COMPOSITION

6.1 Data Selection

The data considered here were collected during the period from July 1997 until September 1998, at which time BIGRAT ceased operation. In April of 1998, the RG8 signal cables on the telescope were replaced by high bandwidth Heliax cabling. Due to the differences in instrumental response and energy threshold for each choice of cabling, we are justified in separating our data into two blocks (A and B) for independent analysis. A summary of these datasets is given in Table 6.1. Block A contains the datasets collected with the original RG8 coaxial cabling and its analysis will be discussed first.

The relationship between the mean triggering rate and zenith angle is shown in figure 6.1 for both data blocks. In figure 6.1(a), the rates at a reduced trigger level have also been included for comparison. The reduction in trigger rate, with increasing zenith angle, appears to be underestimated by the predicted rates derived from equation 5.1, which is based on Monte Carlo modelling. This suggests that the energies assigned to our large zenith angle measurements in the following analysis will be slightly underestimated.

Block A

θ_z	N (before cuts)	N (after cuts)	t_{obs} (s)	Rate (Hz)
0°	2310	1624	5670	0.3
60°	809	570	12390	0.05
70°	256	193	24130	0.008

Block B

θ_z	N (before cuts)	N (after cuts)	t_{obs} (s)	Rate (Hz)
0°	400	346	800	0.4
60°	115	105	1170	0.09
70°	130	122	6100	0.02
75°	399	379	47380	0.008
80°	93	87	58000	0.0015

Table 6.1: A summary of the Block A and B datasets. Event numbers are quoted before and after applying pulse cuts as described in section 4.2.4. The trigger rate for each elevation has also been included as a means of gauging the effort required by future experiments. At larger zenith angles, it may be apparent that the pulse height (maximum) cuts are less important. The lateral distribution of Cerenkov light at these elevations is flatter due to the increased distance to shower maximum. This results in a greater number of small events with pulse amplitudes close to threshold.

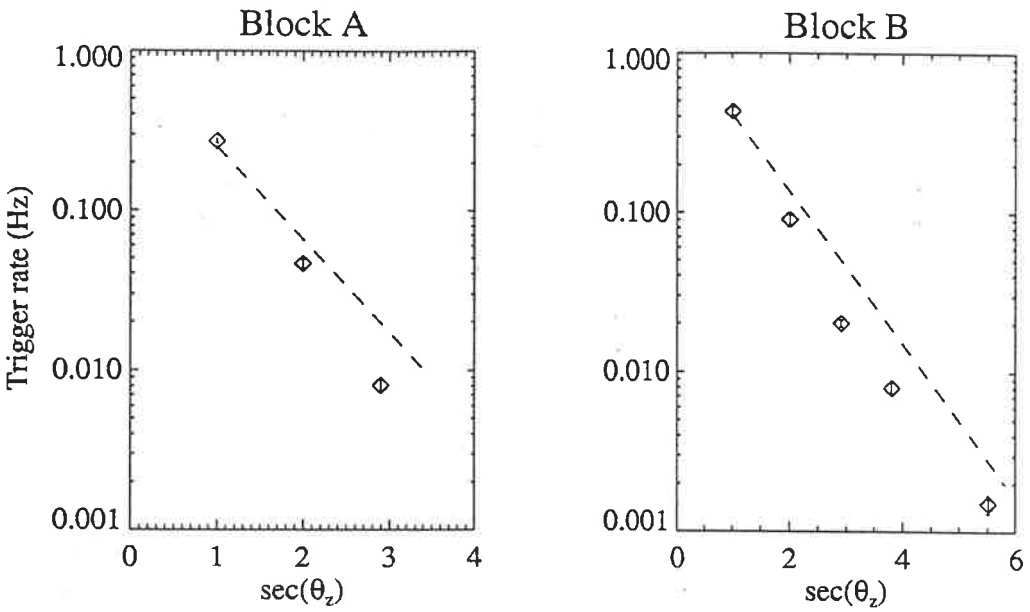

Figure 6.1: The BIGRAT trigger rate (◊) as a function of zenith angle for the (a) Block A data, and (b) Block B data. The trigger criteria for each were shown in table 5.1. The dashed lines represent estimates of the rates based on simulations up to 70°. These have been extrapolated to indicate the event rate expected at a zenith angle of 80°.

6.2 Analysis of Block A Data

The energy threshold of an atmospheric Čerenkov telescope varies greatly with primary mass. This means that the detector will preferentially select certain cosmic ray species based on their individual triggering efficiencies. Relating the composition predicted from indirect ground-based measurements back to a primary composition above the atmosphere is thus non-trivial. Confident interpretation through Monte Carlo calculations relies on the accurate modelling of shower development, the correct choice of hadronic interaction model (particularly for energies approaching the knee), and knowledge of the primary energy spectrum of each species.

Due to the poor energy resolution of our detector, there is no way of obtaining a model independent estimate of mass composition as a function of primary energy. Instead we shall make use of the spectra measured by the JACEE group (as summarised by Watson 1997) in equation 5.2. The results of our analysis will therefore yield evidence for confirming or rejecting the JACEE model based on purely ground-based measurements. This will be most valuable at the extrapolated energies where JACEE measurements become less certain because of low statistics.

In the context of the limited energy and mass resolution of a simple detector such as the one used in this thesis, we shall only attempt to interpret our results using a two-component composition model. Thus, we will assume that our measured data are a mixture of light (pure protons) and heavy (pure iron nuclei) components. Since it is a stable element, iron is generally considered to be the heaviest matter likely to be found in significant quantities in galactic cosmic radiation. We will estimate the mixing ratio of these components in the BIGRAT data by comparing the measured pulse shape parameter distributions with those from Monte Carlo mixtures.

6.2.1 Pulse Shape Behaviour at Large Zenith Angles

The mean values of each pulse shape parameter, from data block A, are plotted as a function of zenith angle in figure 6.2. Also included are those values derived from CORSIKA generated datasets of proton and iron showers. The triggering conditions have been kept constant for each dataset included and are equivalent to those derived in section 5.3.2. There appears to be a trend for the mean FWHM and fall-time of the BIGRAT data to increase with zenith angle. In contrast, the simulated data suggests a

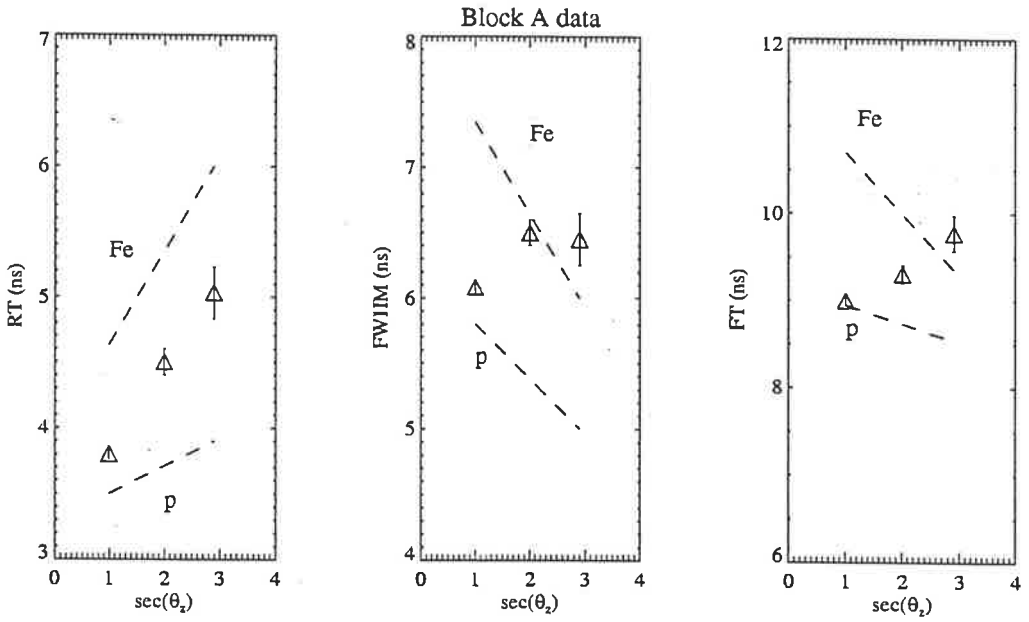

Figure 6.2: The behaviour of the mean rise-time, FWHM and fall-time values, at large zenith angles, is shown for measured BIGRAT data (Δ) and simulated protons and iron (dashed lines).

decrease in the means of these parameters and their overall distributions are observed to become narrower. This may be due to limitations in the complete modelling of atmospheric effects (see section 5.3.3 for further discussion).

A comparison between the measured and simulated mean values for FWHM and fall-time shows poor agreement at large zenith angles. It suggests a radical shift in composition within a relatively short energy range. This seems unrealistic in light of the results of other experiments at these energies. Also, the most sensitive parameter to mass composition, rise-time, does not exhibit this behaviour with zenith angle. We can try to make some sense of the FWHM and fall-time behaviour by returning briefly to section 5.5.3. We saw that the low altitude muon signal tends to fall on the leading edge of the pulse. As a result, the FWHM and fall-time parameters are more sensitive

to the high altitude emission from the electromagnetic component. Thus, they will be more susceptible to atmospheric scattering and absorption than the rise-time.

Even if we have doubts about the validity of our atmospheric modelling, figure 6.2 indicates that rise-time should still be a meaningful parameter for analysis. For the elevations shown, the BIGRAT data appears inconsistent with a pure proton or pure iron composition. Due to the lack of confidence in our ability to properly parameterise the atmospheric propagation for interpreting FWHM and fall-time information, we have concentrated on examining the rise-time in the following analysis.

6.2.2 Initial Composition Estimate Using Mean Rise-Time

Before embarking on a detailed statistical analysis of the entire rise-time distribution, we will first investigate how consistently our measured data can be described by the Monte Carlo data. A simple composition estimate may be obtained by matching the mean rise-time values of measurement and simulation.

We estimate the optimal fraction of a_0 proton and $(1 - a_0)$ iron events in each measured dataset by

$$a_0 \overline{RT}_p + (1 - a_0)\overline{RT}_{Fe} = \overline{RT}_{real} \tag{6.1}$$

where $\overline{RT}_{real}$, $\overline{RT}_p$ and $\overline{RT}_{Fe}$ are the mean rise-time values for BIGRAT data and simulated proton and iron respectively. The standard errors in the mean for each of these distributions are similarly described by $\sigma(\overline{RT}_{real})$, $\sigma(\overline{RT}_p)$ and $\sigma(\overline{RT}_{Fe})$. To quantify the error in our fractional estimate a_0, we assume these distributions are independent and thus neglect covariant terms. The error in a_0 is then calculated from

θ_z	E_{eff}(p) (TeV)	%p	E_{eff}(Fe) (TeV)	%Fe
0°	7	76 ± 6	22	24 ± 6
60°	26	61 ± 8	75	39 ± 8
70°	90	39 ± 11	350	61 ± 11

Table 6.2: Composition estimates at each zenith angle for a two-component model of proton and iron. These were obtained by matching mean rise-time values from measured and simulated data. The effective energy thresholds, E_{eff}, for each elevation and each component have also been included (as defined in section 3.6.2).

$$\sigma^2(a_0) = \sigma^2(\overline{RT}_{real})\left(\frac{\partial a_0}{\partial \overline{RT}_{real}}\right)^2 + \sigma^2(\overline{RT}_p)\left(\frac{\partial a_0}{\partial \overline{RT}_p}\right)^2 + \sigma^2(\overline{RT}_{Fe})\left(\frac{\partial a_0}{\partial \overline{RT}_{Fe}}\right)^2 \quad (6.2)$$

The computed mixing ratio of proton and iron in the BIGRAT data is summarised in table 6.2 as a function of zenith angle and energy. This preliminary study indicates that, as the energy threshold increases with zenith angle, the predicted mass composition becomes increasingly heavy.

We must also confirm that the shape of the rise-time distribution for the estimated proton/iron mixture is consistent with that of the BIGRAT data at each zenith angle. A visual comparison of the measured and simulated data should be sufficient to test the agreement of the width of these distributions. We may then proceed with a more

detailed statistical analysis of their *goodness of fit*. The number of events in each bin follows Poisson behaviour. For the bins on the tail of the distribution, containing few events, the fluctuations can be large. This is particularly true for the 60° and 70° data where the overall statistics are limited. It will therefore be helpful to smooth these distributions prior to further examination. We do this by fitting a mathematical function to each distribution.

Lognormal and gamma functions have been tested to match the asymmetric nature of the distributions. They can be expressed respectively as functions of a single time variable, t, by

$$p(t-c)=\frac{1}{(t-c)\lambda\sqrt{2\pi}}\exp^{-\frac{1}{2}\left(\frac{\ln(t-c)-K}{\lambda}\right)^2} \tag{6.3a}$$

$$\Gamma(t-c)=(t-c)^{\lambda-1}\exp^{-K(t-c)} \tag{6.3b}$$

Both functions are non-linear in their characteristic shape parameters λ, K, and offset parameter, c. We have performed non-linear fits by the method of least squares. The least squares merit function is the sum of the squares of the absolute difference between the number of events in each bin and the model value at a point centred on the bin. The merit function will be minimised by an optimal choice of values for the model parameters. The simple least squares method ignores the errors in each bin and will thus overestimate the significance of low event bins on the tail of the distribution. Alternatively, we could have used a weighted least squares fit, which incorporates the

uncertainties. Nevertheless, the simpler method is a quick means to obtaining a reasonable fit for our purely qualitative purposes.

The multidimensional minimisation has been performed with the downhill simplex method used in the numerical routine "amoeba" (Press et al. 1993). A geometrical figure (the simplex) is defined in parameter space with initial values. The volume of this object is conserved as it takes "steps" in the direction of each vector. After each step, the merit function is evaluated at the vertices of the simplex and the next step is chosen such that the point with the highest value is moved to a lower point. The simplex then spreads through the entire multidimensional space searching for the global minimum.

The best fit to the rise-time distributions has been obtained using the gamma function. It must be mentioned that the choice of model function is purely one of convenience. A close fit between the model and raw data does not imply that the model function necessarily describes some underlying physical mechanism. It simply means that the data can be expressed in this manner. The gamma function curves of measured data and simulated proton and iron data are compared in figure 6.3 for each zenith angle. In each plot, the number of events in each Monte Carlo distribution has been normalised to that of the measured dataset. The curves were then further weighted by the composition estimates quoted in table 6.2.

Given the two-component composition used, the shape of the measured data appears to be well described. However, we can see that, as we move away from the zenith, a three or four-component model will be required to accurately recreate the shape of the

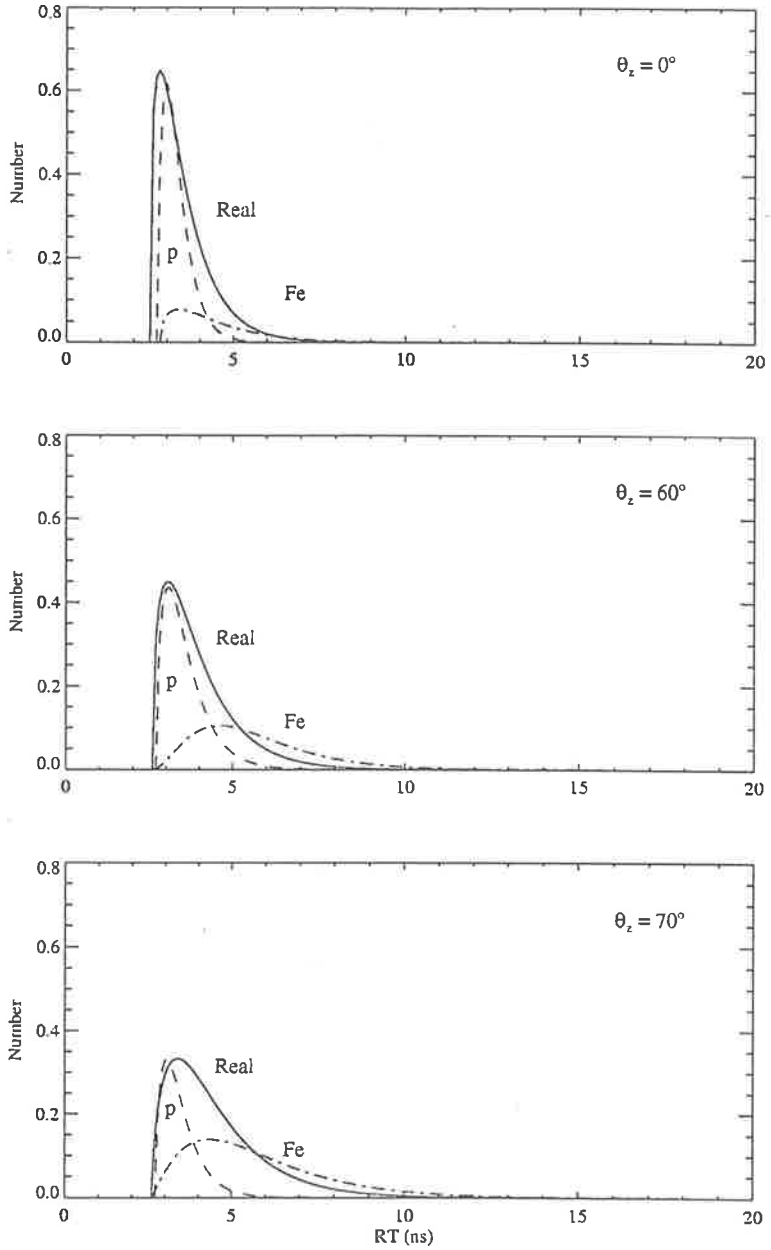

Figure 6.3: The shape of the measured rise-time distribution (solid line) is compared at each zenith angle with that of the simulated proton and iron (dashed lines) where these have been weighted according to the composition estimates in table 6.1. Each distribution has been smoothed by fitting a gamma function. The apparent overestimation of the iron in the tail of the distribution results from using only a two-component model.

BIGRAT rise-time distribution. The lack of medium-mass events causes an apparent excess of iron in the tail. A minor discrepancy exists for the zenith dataset where the measured data contains rise-time bins smaller than can be generated in our simulations. Again, this may indicate some atmospheric absorption not adequately represented. Nevertheless, we must appreciate that these small rise-time pulses only disagree with the minimum simulated pulses by ~ 0.2 – 0.3 ns. This is well below the limits of the time resolution of our detector where the rise-time of the instrumental response is of the order of 2 ns.

6.2.3 Goodness of Fit

The method of least squares used for the curve fitting in the previous section is an example of maximum likelihood estimation. A figure of merit function is chosen to characterise the worth of some statistical test. The probability distribution (or likelihood function) of this merit function may then be described and the maximum likelihood for the statistical test evaluated. The test, in this case, is used to find the best fit between two distributions.

We choose the goodness of fit statistic

$$\chi^2 = \sum_{i=1}^{n} \frac{\left(f_{measured}(i) - f_{mixture}(i)\right)^2}{\sigma_{measured\,i}^{\,2} + \sigma_{mixture\,i}^{\,2}} \qquad (6.4)$$

θ_z	N_{evt}	E_{min}(p) (TeV)	%p	E_{min}(Fe) (TeV)	%Fe	χ_ν^2
0°	1624	3	73 ± 6	10	27 ± 6	2.3
60°	570	10	79 ± 7	40	21 ± 7	2
70°	193	70	55 ± 9	150	45 ± 9	0.5

Table 6.3: Composition estimates obtained from the goodness of fit analysis. The number of events in each analysed BIGRAT dataset is shown, along with the minimum energy of the simulated proton and iron datasets. This will enable the trigger efficiency of each component, with respect to its minimum energy, to be taken into account when deriving primary flux values for the compositional estimates. The reduced chi square value for each fit is also given.

to describe the likelihood that our measured sample distribution, $f_{measured}$, and the sample distribution for a given Monte Carlo mixture, $f_{mixture}$, are drawn from the same population. The differences between the distributions are evaluated at each i^{th} bin and the errors in these bins are given by $\sigma_{measured}$ and $\sigma_{mixture}$ for the two distributions. The χ^2 probability distribution is well known and the maximum likelihood for this statistical fit coincides with the minimum χ^2 value.

The definition of the χ^2 statistic is based on Gaussian errors. However, the number of events in each bin follows Poisson statistics and so the errors will only be approximately normal if there are at least 10 events in the bin. There is a great deal of mass composition information available in the low-event bins on the tail of the distribution. These may still be included if we increase the bin widths until they satisfy the preceding condition for normal errors. Only those bins for which errors could be

reliably estimated at the same point on both distributions were included in the χ^2 calculation.

The minimisation procedure is as follows. A mixture for a given composition is randomly sampled from the proton and iron sample rise-time distributions until the number of events in the mixture distribution is equal to the measured rise-time distribution. The χ^2 value is calculated for each composition mix in 1% increments from pure proton to pure iron. The fraction of proton and iron are then recorded for the minimum χ^2 value together with the number of degrees of freedom, where this is equal to the number of bins fitted minus 1 degree for the normalisation of the number of events in the mixture. Since the number of degrees of freedom may change from one fit to the next, we shall minimise the reduced chi square value, $\chi_\nu^2 = \chi^2/\nu$. The minimisation is repeated 1000 times to describe the variation in composition estimate due to the sampling from finite distributions.

The relative abundances of proton and iron, which have been estimated for each measured dataset in the preceding analysis, are presented in table 6.3. In agreement with the results of our initial estimates (see table 6.2), the mean mass of the triggered composition increases with energy. This composition is subject to a mass dependent bias in the triggering of the telescope, which will affect our results. Before we can compare these results with the direct JACEE measurements, the triggering efficiencies, $T(>E_{min})$, of the proton and iron components must first be removed. Following equation 5.1, we can derive a prediction of the primary flux in m^{-2} sr^{-1} s^{-1}, for each i^{th} mass species, from our fractional composition estimates, N_i. The flux estimates are given by

$$F_i(>E_{\min}) = \frac{1}{T_i(>E_{\min})} \frac{N_i R_{meas}(>E)}{A_{\max}\Omega_{\max}} \tag{6.5}$$

The triggering efficiencies are included with respect to the minimum energy of each Monte Carlo dataset. This sets the energy for the flux estimate. The measured event rate, R_{meas}, must also be included for each elevation considered.

In figure 6.1, it was apparent that there are difficulties in matching the event rates between measurement and simulation for inclined showers. This will underestimate the energies assigned to the primary fluxes for those datasets. Fortunately, we can obtain a correction to these energies by considering this discrepancy between the measured rate and the simulated rate, R_{sim}, at each elevation. By choosing a power law spectrum with exponent, α, from the JACEE spectra (equation 5.2), we can calculate a corrected energy with respect to the assigned energy, E, for each dataset

$$E_{corr} = E\left(\frac{R_{meas}}{R_{sim}}\right)^{-\frac{1}{\alpha}} \tag{6.6}$$

The flux estimates have been plotted in figure 6.4. JACEE measurements are included for comparison. The JACEE spectra have been separated into two components in order to simplify the matching of our estimated fluxes. The proton and helium spectra are combined into a "light" component, with the nitrogen and iron making up a "heavy" component. Unfortunately, in analysing the BIGRAT data, we had to assume that the dataset contained only proton and iron with no intermediate mass primaries. This was because we had no prior knowledge of how the relative abundances of proton and helium (or nitrogen and iron) might depend on energy at the limits of the JACEE

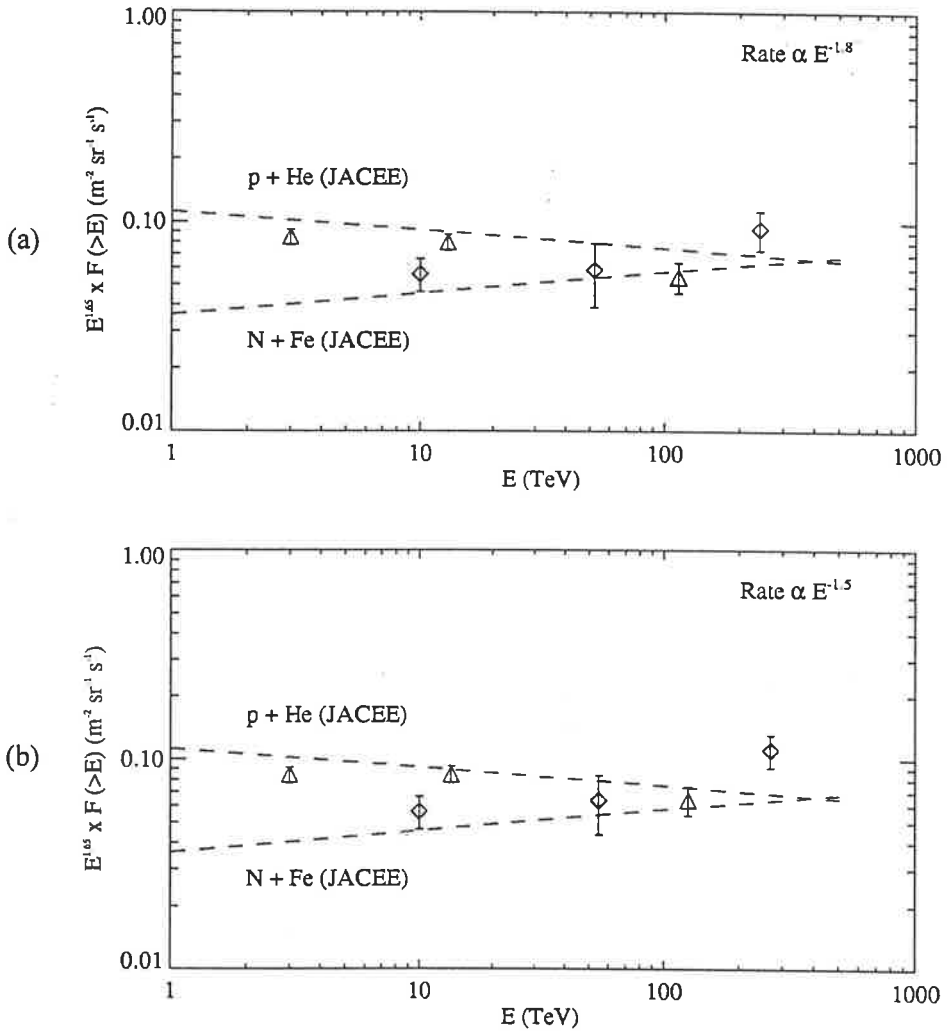

Figure 6.4: Estimated proton (Δ) and iron (◊) fluxes derived from analysis of the Block A data. The dashed lines indicate light and heavy spectra from the JACEE measurements, which have been included here for comparison. Simulated energies have been corrected by assuming the trigger rate follows (a) the proton energy spectrum, and (b) the iron energy spectrum as predicted by JACEE results.

measurements. Thus, a direct comparison of absolute flux values between JACEE data and our data is not possible.

Less ambiguity exists in observing trends in the shape of the spectra. Figure 6.4(a) shows the results where we have scaled the flux energies with respect to the JACEE proton spectrum (α = 1.8), and 6.4(b) shows the same results using the iron spectrum (α = 1.5). The shape of the estimated spectra with the corrected energies does not appear to be particularly sensitive to a reasonable choice of α. The slopes of the estimated proton and iron spectra roughly match that of the light and heavy JACEE components respectively. Without the correction in energy, these estimated spectra would be much steeper. No significant break is observed in either spectrum. However, the datasets providing the highest energy estimate values suffer from low statistics. Further measurements at these energies will still be needed.

6.3 Analysis of Block B Data

The remaining data to be analysed includes about 10 hours at 75° from the zenith, and 20 hours at 80°. We have not yet attempted simulations at these elevations. The effect of atmospheric attenuation results in the loss of much of the signal traversing the greatly increased air mass. The resulting energy threshold increase forces a drastic increase in computing time since the large numbers of photons in such showers are still tracked, even if they aren't collected in the final pulse. Nevertheless, we can still use the measured data to describe pulse shape behaviour at these elevations.

The mean pulse shape parameters are plotted in figure 6.5 as a function of zenith angle and show trends similar to that discussed in section 6.2.1 for the Block A data. Again,

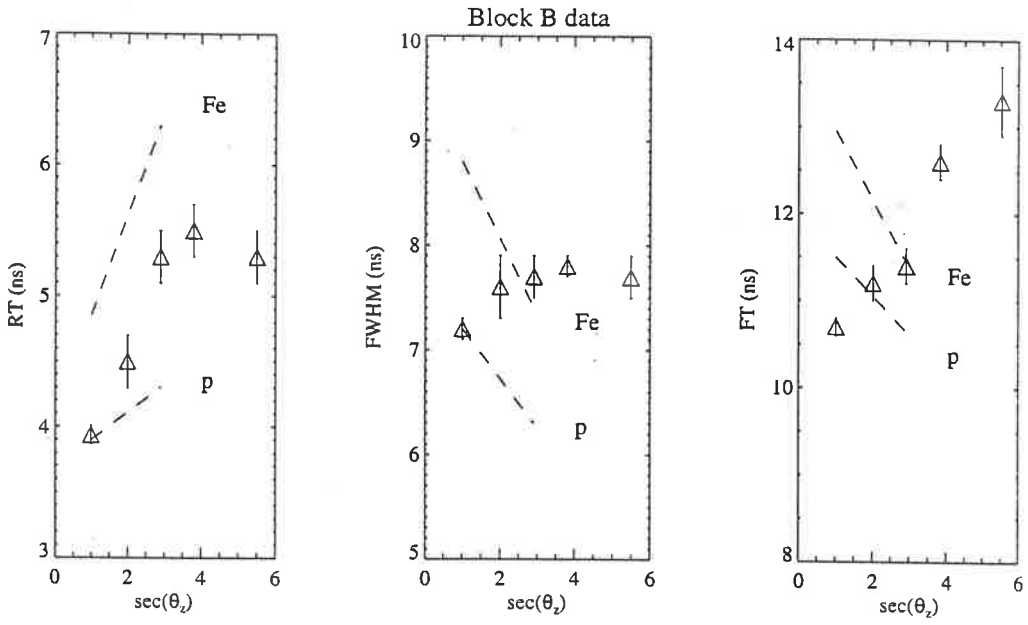

Figure 6.5: The behaviour of the mean rise-time, FWHM and fall-time values, at large zenith angles, is shown for measured data (Δ) and simulated protons and iron (dashed lines). The rise-time and FWHM values, of the BIGRAT data, appear to stop increasing with zenith angles greater than 70°.

we see that the FWHM and fall-time parameters cannot be reconciled with our modelling. Below the elevations that modelled data exist for, an interesting characteristic appears in the measured data. Both the FWHM and rise-time are seen to increase with zenith angle until about 70°. Above this, the mean parameter values become relatively constant. This suggests a limit to the effectiveness of the rise-time as a discriminator at higher zenith angles. Possibly, this reflects the onset of significant energy losses in the muon component traversing such an air mass. The likelihood of low altitude emission will then be reduced as a consequence of the increased attenuation of the muons high in the atmosphere. More measurements at these zenith angles are needed to determine whether this effect is real. If real, this suggests that the Čerenkov pulse shape technique might only be useful for energies up to a few hundred TeV per

θ_z	N_{ev}	E_{min}(p) (TeV)	%p	E_{min}(Fe) (TeV)	%Fe	χ_ν^2
0°	346	3	73 ± 9	10	27 ± 9	1.4
60°	105	10	75 ± 9	40	25 ± 9	0.3
70°	122	70	54 ± 9	150	46 ± 9	0.7

Table 6.4: Composition estimates obtained from the analysis of Block B. Similarly to table 6.3, the number of events of each measured dataset is shown, along with the minimum proton and iron energies considered. Also shown is the reduced chi square value for each fit. The statistics of these datasets is less than in Block A.

nucleon. Following the goodness of fit analysis method described in the previous section, the estimated percentage mix of proton and iron in each dataset are presented in table 6.4. The results are consistent with the previous estimates in table 6.3, although the statistics for the 0° and 60° data are reduced with respect to those in Block A, resulting in increased confidence intervals for a given elevation. It must be noted that the estimates from Block A and Block B are not independent since the same Monte Carlo datasets have been used for both. Thus, the small increase in proton numbers at 60°, seen in both data blocks, may be due to the simulated datasets at this elevation.

Chapter 7

CONCLUSIONS AND SUGGESTED FURTHER WORK

7.1 Conclusions

This thesis has discussed a technique for estimating the mass composition in the energy region between satellite measurements and the knee. Mass discrimination was based on the identification of muon information in the rise-time of Čerenkov pulses observed at ground level. The average breadth of the pulse leading edge shows a logarithmic dependence on primary mass, within the confines of the limited time response of the detector. The mass sensitivity was shown to result from two main factors: the separation in altitude of the muon and electromagnetic signals; and a reduction in the attenuation of the muon signal, with respect to the main Čerenkov front, for large differences in altitude between the two signals. The rise-time parameter also seems largely insensitive to energy and core distance making it well suited for the performance of a single atmospheric Čerenkov detector. This lack of energy dependence is beneficial since accuracy in the energy calibration of such a detector is difficult to achieve with confidence, relying as it does on interpretation from simulations.

Measurements were made with the pulse shape system, described in this thesis, across a large range of zenith angles (0° – 80°) to probe the highest energies possible. Analysis of the data has resulted in estimates of the primary integral fluxes of light and heavy cosmic ray species up to ~ 100 TeV, which seem consistent with JACEE measurements. As such, we see no significant evidence of any break in the proton

spectrum up to at least 100 TeV. Unfortunately, computing limitations have hindered the direct analysis of datasets above 70°, where the primary energies are far greater. Further modelling should be able to extend these results to higher energies. However, there is evidence that the technique loses discrimination power at these larger zenith angles due to significant energy losses of the muon component in such an air mass. If this is true, then there may exist a maximum energy for practical measurements of the order of a few 100 TeV per nucleon, thus preventing the extension of this work up to the knee.

7.2 Modelling Limitations

Monte Carlo simulations have been unable to describe many of the features observed in the pulse shape data preventing a more detailed study. While simulations appear well matched with measurements at the zenith, the trigger rate differs with increasing zenith angle. This resulted in underestimated primary energies based on the simulations, and corrections to these were required for the derivation of primary spectra from our composition estimates.

The discrepancy between the measured and simulated FWHM and fall-time values increases with zenith angle. The increase of these parameters with zenith angle, as observed in our measured data, is difficult to understand. At large zenith angles, the increased distance to shower maximum produces a diminished radius of curvature for the shower front. This results in a flatter core distance relationship for pulse widths and should thus reduce the FWHM value averaged over all core distances. If the FWHM and fall-time parameters contain signals delayed from the main shower front, which are

not considered in the CORSIKA simulations, then this pulse shape behaviour is explained. Resolving these differences would allow the investigation of multi-parameter cuts in enhancing mass discrimination, and would provide a better energy resolution of the analysed data.

Alternatively, incomplete modelling of atmospheric effects may be responsible for the observed differences between measurement and simulation. This is quite possible, given that any effects will be more noticeable with the increase in air mass at large zenith angles. Timing information in the pulse is path length dependent, and multiple scattering of the photons at large zenith angles may be important. Thus, more detailed photon scattering routines need to be included in the simulations. This should also be supported by LIDAR measurements of atmospheric clarity at the time of observation.

7.3 Further Work

A reduction in instrumental response to sub-nanosecond rise-times will aid mass discrimination, particularly near the zenith. With such a reduction, we might hope to extend our analysis to a three or four-component model. This enhanced discrimination would enable a more precise estimate of the primary flux for each of these species, without being biased by the use of too simplistic a model like the proton/iron mixture considered here.

Further measurements at zenith angles greater than 70° are needed. With the triggering criteria described here: 100 hours at 75° would give ~ 3000 events; and 100 hours at 80° would provide ~ 700 events. Better understanding of the modelling at these zenith angles will be needed before confident interpretation of this data is possible.

REFERENCES

Aglietta, M. et al. (1999), *Astropart. Phys.* **10**, 1.

Aharonian, F. et al. (1998), *Nucl. Phys. Proc. Supp.* **60B**, 193.

Aharonian, F. et al. (1999), *Phys. Rev.* **D59**, 092003.

Ahmad, Q. et al. (2001), *Phys. Rev. Lett.* **87**, 071301.

Allan, H. (1971), *Prog. Elem. Part. and Cosmic Ray Physics* **10**, 170.

Allen, C. (1973), Astrophysical Quantities, The Althone Press (Uni. Of London).

Allen, G. et al. (1999), *Proc. 26th ICRC (Salt Lake City)* **3**, 480.

Anderson, C. (1933), *Phys. Rev.* **43**, 491.

Antoni, T. et al. (1999), *J. Phys. G: Nucl. Phys.* **25**, 2161.

Apanasenko, A. et al. (1995), *Proc. 25th ICRC (Rome)* **3**, 571.

Apanasenko, A. et al. (2001), *Proc. 27th ICRC (Hamburg)* 1626.

Arqueros, F. et al. (2000), *Astron. Astrophys.* **359**, 682.

Asakimori, K. et al. (1998), *Astrophys. J.* **502**, 278.

Auger, P. et al. (1939), *Rev. Mod. Phys.* **11**, 288.

Bednarek, W. & Protheroe, R. (2001), *Astropart. Phys.*, in press.

Bernlohr, K. (2000), *Astrop. Phys.* **12**, 255.

Biermann, P. (1994), *in* 'High Energy Astrophysics', ed. Matthews, J. (World Scientific), p. 217.

Binns, W. et al. (1999), *Proc. 26th ICRC (Salt Lake City)* **3**, 21.

Blackett, P. & Occhialini, G. (1933), *Proc. Royal Soc.* **A139**, 699.

Blackett, P. (1948), *in* Rep. Conf. Gassiot Comm. Of the Physical Society, London on 'Emission Spectra of the Night Sky and Aurora', p. 34.

Boley, F. et al. (1962), *Phys. Rev.* **124**, 1205.

Boley, F. (1964), *Rev. Mod. Phys.* **36**, 792.

Browning, R. & Turver, K. (1977), *Il Nuovo Cim.*, **A38**, 223.

Castellina, A. (2001), *Nucl. Phys. Proc. Suppl.* **97**, 35.

Čerenkov, P. (1934), *C. R. Acad. Sci. U.S.S.R.* **8**, 451.

Chadwick, P. et al. (1999), *J. Phys. G: Nucl. Phys.* **25**, 1223.

Clay, J. (1934), *Physica* **1**, 363.

Clay, R. et al. (1998), *Pub. Aust. Astro. Soc.* **15**, 332.

Colgate, S. & Johnson, M. (1960), *Phys. Rev. Lett.* **5**, 235.

Compton, A. (1933), *Phys. Rev.* **43**, 387.

Costa, C. (1998), *Phys. Rev.* **D57**, 4361.

Dawson, B. (1985), The Lateral Distribution of Cerenkov Light from Extensive Air Showers, PhD Thesis, University of Adelaide.

Dawson, B. et al. (1989), *J. Phys. G : Nucl. Phys.* **15**, 893.

de Nolfo, G. et al. (1999), *Proc. 26th ICRC (Salt Lake City)* **3**, 29.

deBeer, J. et al. (1966), *Proc. Phys. Soc. Lond.* **89**, 567.

Dixon, H., Turver, K. & Waddington, C. (1974), *Proc. Phys. Soc. Lond.* **A339**, 157.

Doll, P. et al. (1990), The Karlsruhe Cosmic Ray Project KASCADE, KfK Report 4686.

Dowden, S. et al. (1997), *Meas. Sci. Tech.* **8**, 1258.

Enomoto, R. et al. (2002), *Astropart. Phys.* **16**, 235.

Fermi, E. (1949), *Phys. Rev. Lett.* **75**, 1169.

Fesefeldt, H. (1985), Report **PITHA-85/02**, RWTH Aachen.

Feynman, R. (1969), *Phys. Rev. Lett.* **23**, 1415.

Fomin, Y. & Khristiansen, G. (1972), *Sov. J. Nucl. Phys.* **14**, 360.

Frank, I. & Tamm, I. (1937), *Dokl. Akad. Nauk. S.S.S.R.* **14**, 109.

Gaisser, T. (1990), Cosmic Rays and Particle Physics, Cambridge University Press.

Galbraith, W. & Jelley, J. (1953), *Nature* **171**, 349.

Garcia-Munoz, M. et al. (1977), *Ap. J.* **217**, 859.

Gregory, A. et al. (1987), *Nucl. Instr. Meth.* **A257**, 423.

Greisen, K. (1960), *Ann. Rev. Nucl. Sci.* **10**, 63.

Greisen, K. (1966), *Phys. Rev. Lett.* **16**, 748.

Grigorov, N. et al. (1970), *Sov. J. Nucl. Phys.* **11**, 588.

Grigorov, N. et al. (1972), *Proc. 12th ICRC (Hobart)* **5**, 1752.

Grindlay, J. (1971), *Il Nuovo Cim.* **2B**, 119.

Handbook of Geophysics and Space Environments (1965), ed. Valley, S., Air Force Cambridge Research Laboratories, (US Air Force).

Handbook of Optics (1978), ed. Driscoll, W. (McGraw-Hill), p. 14-1.

Hayashida, N. et al. (1999), *Astropart. Phys.* **10**, 303.

Heck, D. et al. (1998), Report **FZKA 6019**, Forschungszentrum Karlsruhe.

Heitler, W. (1935), Quantum Theory of Radiation, 2nd Edition, Oxford University Press.

Hess, V. (1912), *Physik. Zeitschr.* **13**, 1084.

Hillas, A. (1982), *J. Phys. G: Nucl. Phys.* **8**, 1475.

Hillas, A. & Patterson, J. (1987), VHE Gamma ray Astronomy, K. Turver, ed., (Dordrecht : D. Reidel), p. 243.

Hillas, A. & Patterson, J. (1990), *J. Phys. G : Nucl. Phys.* **16**, 1271.

Hofmann, W. (1999), 'Proc. Int. Work. "Towards a Major Atmospheric Cherenkov Detector VI" (Salt Lake City)', p.500.

Ip, W. & Axford, W. (1991), *in* "Particle Acceleration in Cosmic Plasmas", eds. Zank, G. & Gaisser, T. (A. I. P. Conf. Proc. No.264, New York), p.400.

Jackson, J. (1962), Classical Electrodynamics, John Wiley and Sons, New York.

Jelley, J. & Galbraith, W. (1955), *J. Atmos. Terr. Phys.* **6**, 250.

Jelley, J. (1967), *Prog. Elem. And Cosmic Ray Physics* **9**, 41.

Jelley, J. (1982), *in* P. Ramana Murthy & T. Weekes, eds., 'Proc. Int. Workshop on VHE Gamma ray Astronomy, Ooty.', p.3.

Johnson, T. (1940), *Phys. Rev.* **57**, 1047.

Johnston, M. (1998), Honours Thesis, University of Adelaide.

Jokipii, J. & Morfill, G. (1987), *Ap. J.* **313**, 842.

Kalmykov, N., & Ostapchenko, S. (1993), *Yad. Fiz.* **56**, 105.

Kampert, K. et al. (2001), *World Scientific*, in press.

Karle, A. et al. (1995), *Astropart. Phys.* **3**, 321.

Kniffen, D. et al. (1999), 'Proc. Int. Work. "Towards a Major Atmospheric Cherenkov Detector VI" (Salt Lake City)', p.492.

Kolhorster, W. (1913), *Physik. Zeitschr.* **14**, 1066, 1153.

Konopelko, A. et al. (1990), *Proc. 21st ICRC (Adelaide)* **4**, 484.

Krennrich, F. et al. (1999), 'Proc. Int. Work. "Towards a Major Atmospheric Cherenkov Detector VI" (Salt Lake City)', p.515.

Kulikov, G. & Khristiansen, G. (1958), *Soviet Physics JETP* **35**, 635.

Lagage, P. & Cesarsky, C. (1983), *Astron. Astrophys.* **118**, 223.

Linsley, J. (1985), *Proc. 19th ICRC (La Jolla)* **3**, 461.

Mahan, S. et al. (1999), *Proc. 26th ICRC (Salt Lake City)* **3**, 17.

Mallett, L. (1926), *C. R. Acad. Sci. (Paris)* **188**, 445.

Matthews, J. et al. (2001), *Proc. 27th ICRC (Hamburg)* 745.

McGee, P. (2000), private communication.

Moliere, G. (1948), *Z. Naturforsch* **3a**, 78.

Nelson, W. et al. (1985), Report **SLAC 265**, Stanford Linear Accelerator Center.

Nesterova, N. & Chudakov, A. (1955), *Zh. Eksp. Teor. Fiz.* **28**, 384.

Nishimura, J. & Kamata, K. (1951), *Prog. Theor. Phys.* **6**, 628.

Patterson, J. & Hillas, A. (1983a), *J. Phys. G : Nucl. Phys.* **9**, 1433.

Patterson, J. & Hillas, A. (1983b), *J. Phys. G : Nucl. Phys.* **9**, 323.

Patterson, J. & Hillas, A. (1989), *Nucl. Inst. Meth.* **A278**, 553.

Peters, B. (1961), *Il Nuovo Cimento* **22**, 800.

The Pierre Auger Design Report (1985),
http://www.auger.org/admin/DesignReport/index.html

Porter, N. (1973), *Il Nuovo Cim.* **8**, 481.

Press, W. et al. (1993), Numerical Recipes, 2nd Edition, Cambridge University Press.

Protheroe, R. & Szabo, A. (1992), *Phys. Rev. Letters* **69**, 2885.

Ptuskin, V. et al. (1999), *Proc. 26th ICRC (Salt Lake City)* **4**, 195.

Rachen, J. & Biermann, P. (1993), *Astron. Astrophys.* **272**, 161.

Ramana Murthy, P. & Wolfendale, A. (1986), Gamma ray Astronomy, p.182., Cambridge : Cambridge University Press.

Rao, M. & Sinha, S. (1988), *J. Phys. G : Nucl. Phys.* **14**, 811.

Rhode, W. et al. (1996), *Nucl. Inst. Meth.* **A378**, 399.

Roberts, M. et al. (1991), *Proc. 22nd ICRC (Dublin)* **2**, 645.

Roberts, M. (1993), A Search for VHE Gamma Rays from Her-X1 using the Pulse Profile Technique, PhD Thesis, University of Adelaide.

Roberts, M. et al. (1998), *J. Phys. G : Nucl. Part. Phys.* **24**, 255.

Roberts, M. (2000), *Astropart. Phys.* **12**, 239.

Rossi, B. & Greisen, K. (1941), *Rev. Mod. Phys.* **13**, 240.

Rossi, B. (1930a), *Nature* **125**, 636.

Rossi, B. (1930b), *Phys. Rev.* **36**, 606.

Rossi, B. (1952), High Energy Particles, Prentice-Hall, Inc.

Roth M. et al. (1999), *Proc. 26th ICRC (Salt Lake City)* **HE** 2.2.40.

Rowell, G. (1995), A Search for VHE Gamma Rays from PSR1706-44 using the Atmospheric Cerenkov Imaging Technique, PhD Thesis, University of Adelaide.

Skobelzyn, D. (1929), *Z. Phys.* **54**, 686.

Sommers, P. & Elbert, J. (1987), *J. Phys. G : Nucl. Phys.* **13**, 553.

Störmer, C. (1964), The Polar Aurorae, Oxford : Oxford University Press.

Strong, A. & Moskalenko, I. (1998), *Ap. J.* **509**, 212.

Swordy, S. et al. (1993), *Ap. J.* **403**, 658.

Thornton, G. & Clay, R. (1979), *Phys. Rev. Lett.* (erratum *Phys. Rev. Lett.* (1981), **45**, 1463) **45**, 1622.

Thornton, G. & Clay, R. (1981), *Phys. Rev. D* **23**, 2090.

Tümer, O. et al. (1990), *Proc. 21st ICRC (Adelaide)* **4**, 238.

Venkatesan, D. (1990), *Phys. in Can.* **46(1)**, 4.

Volk, H. & Biermann, P. (1988), *Ap. J.* **333**, L65.

Watson, A. (1997), *Proc. 25th ICRC (Durban), Invited & Rapp. Talks* **8**, 257.

Weekes, T. (1976), *Il Nuovo Cim.* **35B**, 95.

Werner, K. (1993), *Phys. Rep.* **232**, 87.

Westfall, G. et al. (1979), *Phys. Rev. C* **19(4)**, 1309.

Yanasak, N. et al. (1999), *Proc. 26th ICRC (Salt Lake City)* **3**, 9.

Zatsepin, V. (1965), *Soviet Physics JETP* **20**, 459.

Zatsepin, G. & Kuz'min, V. (1966), *JETP Lett.* **4**, 78.